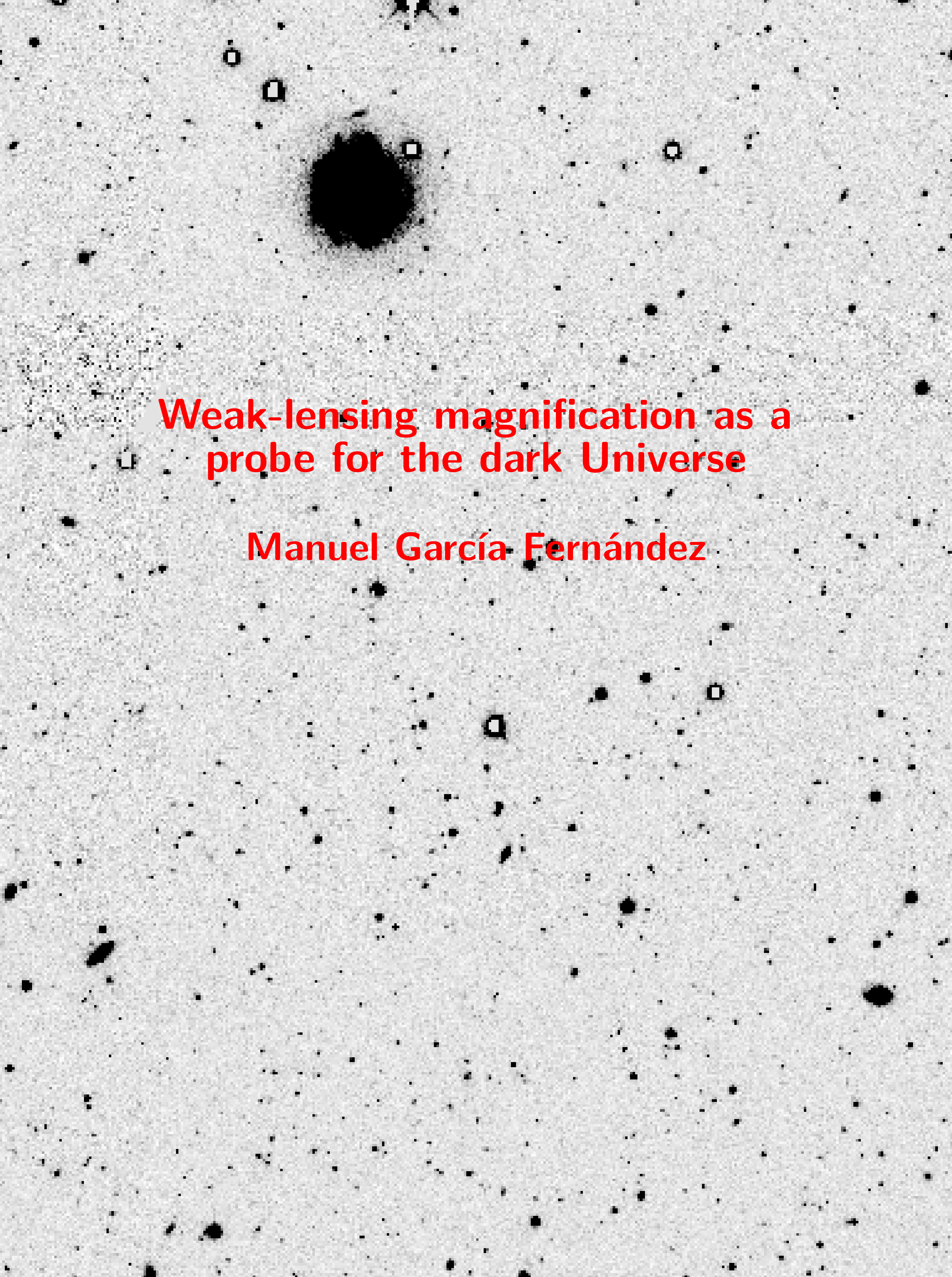

Weak-lensing magnification as a probe for the dark Universe

Manuel García Fernández

GOBIERNO DE ESPAÑA
MINISTERIO DE ECONOMÍA, INDUSTRIA Y COMPETITIVIDAD
Ciemat
Centro de Investigaciones Energéticas, Medioambientales y Tecnológicas
EXCELENCIA MARÍA DE MAEZTU
cfp
CIEMAT
física de partículas

Departamento de Investigación Básica – División de Astrofísica de Partículas
Centro de Investigaciones Energéticas Medioambientales y Tecnológicas

&

Departamento de Física Teórica – Facultad de Ciencias
Universidad Autónoma de Madrid

Weak-lensing magnification as a probe for the dark Universe

Magnificación por lentes gravitacionales débiles como sonda del universo oscuro

Tesis presentada por:
Thesis submitted by:
Manuel García Fernández
Para el grado de Doctor en Física Teórica.
For the degree of Ph.D. of Theoretical Physics.

Dirigido por:
Supervised by:
Dr. Eusebio Sánchez Álvaro
&
Dr. Ignacio Sevilla Noarbe

Madrid, Marzo-XXX del 2017

According to RD-99/2011, in partial fulfillment to obtain the 'Mención Internacional' qualification, this Thesis is written in English.
According to UAM's Normative (12/15/2011), Summary and Conclusions are also written in Spanish and included before the core of the Thesis, right after the table of contents.

Conforme al RD-99/2011, en requerimiento parcial para la obtención de la calificación de 'Mención Internacional', esta Tesis está redactada en Inglés.
Conforme al acuerdo del Consejo de Gobierno de la UAM (15/12/2011), el Resúmen y las Conclusiones también se encuentran redactadas en Castellano y se incluyen antes del cuerpo de la Tesis justo después del índice.

This Thesis is part of the following publication archives:
The DES Collaboration archive:
Fermilab preprint/thesis server:

Part of the results obtained during the development of this Thesis has been published under peer-review journals and proceedings. Their references are listed below.
Parte de los resultados obtenidos durante el desarrollo de esta Tesis han sido publicados en revistas y conferencias con un proceso de revisión por pares. Sus referencias bibliográficas se encuentran abajo.

M. Garcia-Fernandez, E. Sanchez and N. Sevilla-Noarbe. *Magnification with wide-field photometric surveys.* Highlights on Spanish Astrophysics XII. March 2017.

M. Garcia-Fernandez et al. *Weak lensing magnification in the Dark Energy Survey Science Verification data*, arXiv:1611.10326. November 2016.

Cover image credit: M. Garcia-Fernandez & The DES Collaboration
Chapter header credit: NASA

Yesterday's sensation is today's calibration.
RICHARD FEYNMAN

And tomorrow's background!
VALENTINE TELEGDI

Contents

Resumen y Conclusiones

Resumen

Medidas recientes de diferentes experimentos arrojan dos efectos observacionales: el Universo es plano y se expande de forma acelerada. Estes dos resultados no están permitidos simultáneamente en la teoria gravitatoria actual –la Relatividad General– en su formulación original. Las alternativas a la Relatividad General que tienen en cuenta la expansión acelerada en universos planos son: la constante cosmológica, la presencia de campos cuánticos exóticos y teorías de gravedad modificada. Sea cual sea la respuesta se le denomina energía oscura.

El experimento que se está desarrollando actualmente que está específicamente diseñado para desvelar la naturaleza de la energía oscura es el Dark Energy Survey (DES), que usará cuatro métodos para discriminar qué teoría es la correcta: Supernovas de tipo 1a (SNIa), el número de clústeres de galaxias, las oscilaciones acústicas de bariones y las lentes gravitacionales débiles.

Las lentes gravitacionales débiles son producidas por la deflexión las trayectorias de los fotones en la presencia de campos gravitatorios lo que se traduce en un curvado de los rayos de luz. Esto implica que la luz emitida por galaxias lejanas es desviada por la materia localizada entre dichas galaxias y el observador. Para fuentes extensas, esto se traduce en dos efectos observacionales: un aumento isótropo del tamaño (magnificación) y una elongación/encogimiento a lo largo de uno de los ejes (*shear*).

Dado que el brillo superficial se conserva, el incremento del tamaño debido a la magnificación produce un incremento del flujo de las galaxias que se encuentran más alejadas. Esto permite ver galaxias que estarían por debajo del umbral de detección is el efecto de lente gravitacional no existiese. Este efecto es conocido como *number-count magnification* y permite medir el perfil de convergencia de la muestra seleccionada como lente, que está directamente relacionado con el perfil de materia.

En esta Tesis, se desarrolla una nueva metodología para estudiar el efecto *number-count magnification* y se aplica al catálogo de datos *Science Verification* del experimento *Dark Energy Survey*. Esta nueva metodología empleada usa galaxias fuente de la población general de galaxias seleccionadas puramente por su *redshift* fotométrico. Esta muestra está mucho más poblada, lo que permite usar lentes menos densas. Además una nueva técnica para estudiar errores sistemáticos con la ayuda de simulaciones se ha usado, lo que permite aportar medidas fiables y no sesgadas. Finalmente en los datos *Year 1* de DES se ha medido el perfil de convergencia de *voids* y *troughs* usando esta nueva metodología.

La determinación del perfil de convergencia de *voids* y *troughs* es una forma excelente de revelar la naturaleza de la energía oscura, dado que son grandes regiones donde hay una gran infra-densidad de materia, por lo que su evolución y estructura está dominada por la energía oscura. Sin embargo, las predicciones teóricas del perfil de convergencia de *voids* en modelos de gravidad modificada no están todaía disponibles. Dado esto, una nueva ventana para desvelar la naturaleza de la energía oscura se a abierto aunque aún necesita de desarrollo.

Conclusiones

La Relatividad General ha sido la teoría gravitatoria desde que Einstein la concibiese hace un siglo. Desde entonces, ha pasado satisfactoriamente las pruebas más exigentes. Sin embargo, el descubrimiento de la expansión acelerada del Universo –energía oscura– junto con los últimos resultados del LHC en el campo de la Física de Altas Energías sugiere que algo debe estar mal o en el campo del Model Estándar Física de Partículas o que hay algo más allá de la Relatividad General.

Medidas de la gravedad en escalas cosmológicas puede arrojar pistas sobre la naturaleza de la energía oscura. Uno de dichos escenarios, son las regiones más vacías del Universo: *voids* y *troughs*. Dado que dichas regiones están mayormente vacías de materia, su evolución y estructura está dominada por la energía oscura. Esto implica que constituyes un entorno prometedor para sondar la energía oscura.

Las medidas de las propiedades de *voids* y *troughs* se pueden hacer con el efecto de lente gravitacional débil, es decir: magnificación y *gg-lensing*. La ventaja de usar estes dos métodos es que son efectos complementarios del mismo fenómeno pero son sensibles a diferentes errores sistemáticos. Esto implica que la combinación de estes dos métodos para medir *voids* y *troughs* proporciona una medida precisa y fiable para la naturaleza de la energía oscura.

Aunque los grandes cartografiados de galaxias han producido durante los últimos años numerosos resultados de lentes gravitacionales,

Summary

Latest measurements from different experiments lead to two observational effects: the Universe is flat, and its expansion is accelerated. Previos results are not allowed at the same time with the current gravitational theory –General Relativity– on its original formulation. The alternatives to General Relativity to take into account the accelerated expansion on flat universes are: the cosmological constant, the presence of exotic quantum fields and modified gravity theories. Whatever it's the answer it is called dark energy.

The current experiment specifically designed to unravel the nature of dark energy is the Dark Energy Survey (DES), that will use four probes to discriminate which theory is right: Type Ia Supernovae (SNIa), cluster counts, barion acoustic oscillation (BAO) and weak-lensing.

Weak-lensing is produced by the gravitational bending of the trajectory of photons by gravitational fields leading to the deflection of the light rays. Thus, the light emitted by foreground distant galaxies is deflected by the matter located between them and the observe. For extended sources, in addition to the change in position, for extended sources, this leads to two observational effects: an isotropic size enlargement (magnification) and an elongation/shrink along one axis (shear).

Since the surface brightness is preserved, the isotropic size enlargement due to magnification produces an increase on the observed flux of the background galaxies. This allows to see galaxies that would be beyond the detection threshold if gravitational lensing was not present. Since this flux augmentation is dependent on the distance to the objects that produce lensing, nearby the lenses the observed density of sources is increased. This effect is known as number-count magnification and allows to probe the convergence profile of the lens sample selected, that is a proxy for the matter profile.

On this Thesis, a methodology to study number-count magnification is developed and applied to the Dark Energy Survey Science Verification data. This new methodology employs source galaxies from the general population selected purely by photometric redshift. This sample is much more numerous, allowing to use a sample with much lower number of lenses. In addition a new technique to estimate systematic errors using simulations has been used, allowing to unbiased an reliable measurements. In additions, on the DES Year 1 data, the convergence profile of voids an troughs is determined using this new methodology.

The measurement of voids and troughs convergence profile is an excellent way to test the nature of dark energy, since they are large under-dense regions of the Universe and they are environments whose evolution is dominated by dark energy. Nevertheless, theoretical work on the convergence profile of voids is still not available. Thus a new window to test dark energy has been opened with this study that still needs to keep development.

1. Introduction

Nature's change and evolution is produced by the dynamics that governs bodies and systems contained in the Universe. All the known interactions can be described in terms of the four Fundamental Forces: gravitation, weak, electromagnetic and strong in ascending order of relative strength. High Energy Physics was able to describe the weak, electromagnetic and strong forces in terms of a $SU(3) \times SU(2) \times U(1)$ gauge symmetry group in what is known as the *Standard Model* [1–5]. Nevertheless, attempts to include Gravitation in a similar frame has not provided yet satisfactory results.

The current consensus theory of gravitation is Einstein's General Relativity, that describes gravity as a deformation of the space-time. It is based on two assumptions: physical laws must be the same in every coordinate system (Principle of Covariance) and Special Relativity must hold locally for every inertial observer (Principle of Equivalence). The most general second-order differential equation that holds these principles is the Einstein's field equation [6–9]

$$R_{\mu\nu} - \frac{1}{2} R g_{\mu\nu} + \Lambda g_{\mu\nu} = \frac{8\pi G_N}{c^4} T_{\mu\nu}, \tag{1.1}$$

where $R_{\mu\nu}, T_{\mu\nu}$ are the Ricci and energy-momentum tensor respectively, c the speed of light and $R = g^{\mu\nu} R_{\mu\nu}$ is the Ricci scalar. The free parameters of this equation are G_N –Newton's constant– and Λ, the cosmological constant.

Previous equation can also be obtained on the variational formalism using the Einstein-Hilbert action [10]:

$$S = \frac{c^4}{16\pi G_N} \int d^4x \sqrt{-g} (R - 2\Lambda) + S_M, \tag{1.2}$$

with S_M the matter term of the action and $g = \det(g_{\mu\nu})$.

1.1 The ΛCDM Cosmology

One of the consequences of Einstein's equation is that the metric tensor is not static, implying that the geometry of the Universe changes. Thus, the space-time is a dynamical entity itself and its past and future evolution can be computed within the framework of General Relativity.

Assuming that the Universe is homogeneous and isotropic [11, 12], the only possible metric tensor is the Friedman-Lemaître-Robertson-Walker metric (FLRW) given by the line element [13]

$$ds^2 = -dt^2 + a^2(t)\left[\frac{dr^2}{1-Kr^2} + r^2(d\theta^2 + \sin^2\theta d\phi^2)\right], \tag{1.3}$$

where $a(t)$ is a function of time know as scale factor, $K = -1, 0, 1$ is the curvature of the universe and r, θ, ϕ are the spatial 3D spherical coordinates.

Solving Einstein's equation for this metric, an expression for the evolution of the scale factor with time can be obtained

$$H^2(t) \equiv \left[\frac{\dot{a}(t)}{a(t)}\right]^2 = \frac{8\pi G_N}{3c^4}\rho(t) - \frac{K}{a^2(t)}, \tag{1.4}$$

where the dot denotes time derivatives, and ρ is the total density of energy. The parameter H has been defined as the expansion rate and its value at present H_0 is known as Hubble's constant.

Expansion rate can be expressed in terms of the normalized energy densities

$$H^2(t) = H_0^2\left[\sum_i \Omega_i(t) - \Omega_K\right] \tag{1.5}$$

with

$$\Omega_K \equiv \frac{K}{[a(t)H_0]^2} \quad \text{and} \quad \Omega_i(t) \equiv \frac{8\pi G_N \rho_i(t)}{3H_0^2}. \tag{1.6}$$

The parameter Ω_i is the density of the i-th matter/energy specie whose evolution with time can be computed using Thermodynamics. For non-relativistic matter –that is, matter with velocity $v \ll c$–,

$$\Omega_M(t) = \Omega_M^0 a^{-3}(t), \tag{1.7}$$

whereas for relativistic matter species –that is, $v \sim c$–

$$\Omega_r(t) = \Omega_r^0 a^{-4}(t). \tag{1.8}$$

Here Ω_i^0 denotes the value on the present day of the i-th matter specie and, by construction, the following equation holds:

$$\sum_i \Omega_i^0 = 1 + \Omega_K^0. \tag{1.9}$$

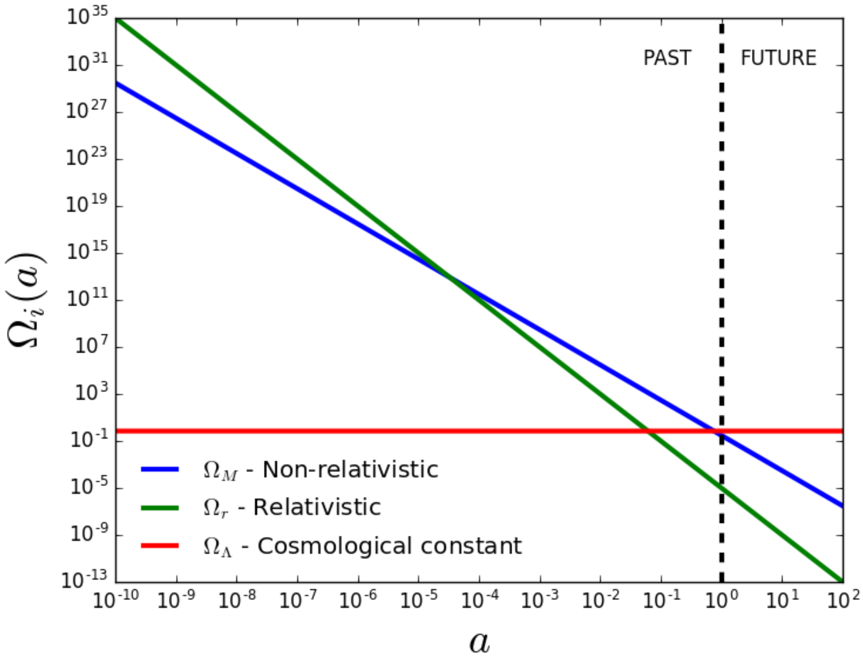

Figure 1.1: Critical energy density for different types of matter species as function of the scale parameter of the Universe: relativistic (cold matter), non-relativistic (radiation), and cosmological constant. It can be seen that at present (black-dashed line), cosmological constant has just started to be dominant over the other species.

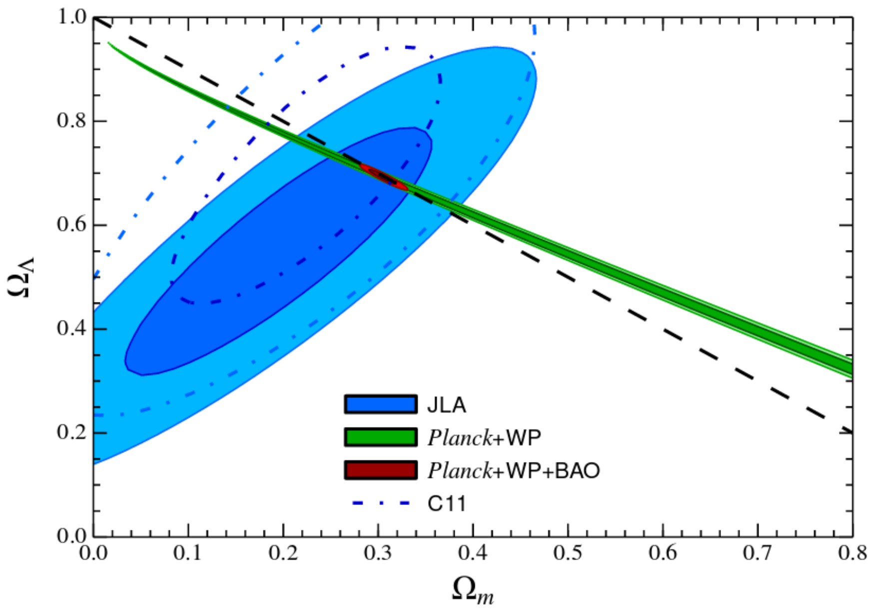

Figure 1.2: Determination of the non-relativistic matter and dark energy content of the universe with the combination of SNIa, BAO, CMB from [14].

Ω_M	Ω_Λ	Ω_b	Ω_K
0.315 ± 0.013	0.685 ± 0.013	0.04904 ± 0.00051	-0.0001 ± 0.0052

Table 1.1: Density at present of the different matter species according to Planck 2015 [15].

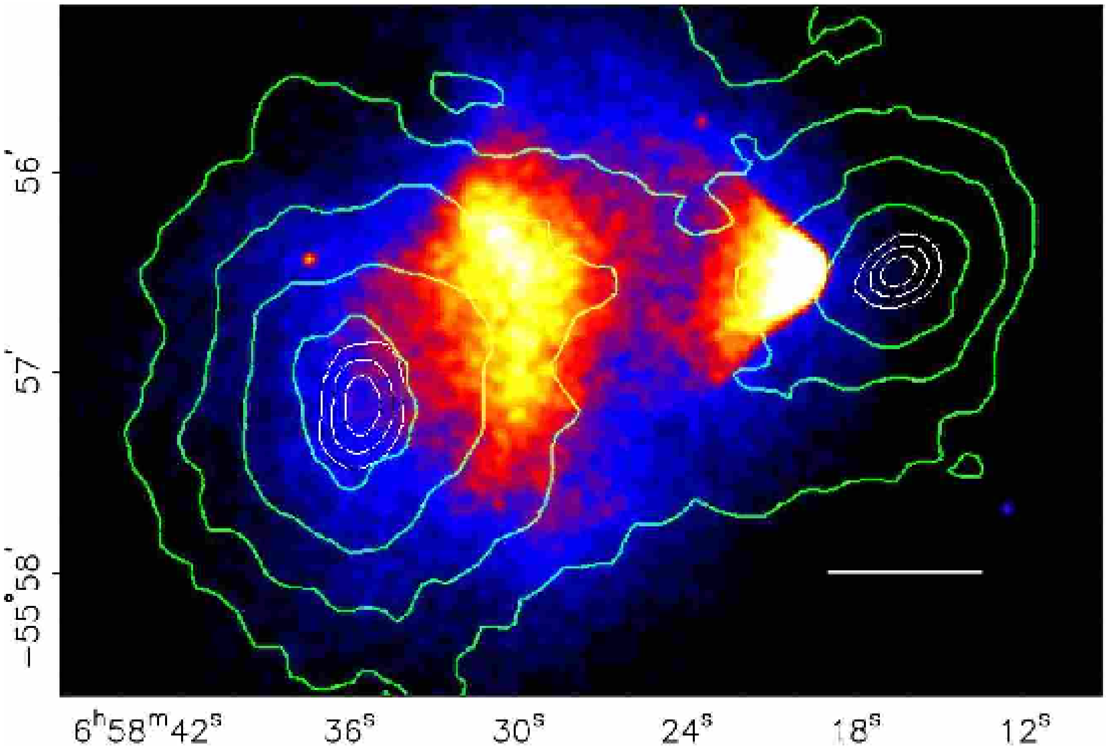

Figure 1.3: Bullet cluster. Colors indicate the baryonic mass measured with gamma-rays, whereas the solid lines indicate the mass reconstructed with gravitational lensing. This result is considered the clearest evidence that baryonic- and dark-matter are decoupled. Image taken from [16].

Taking into account that the matter species and the curvature evolve on a different manner with time (Figure 1.1), its relative abundance at present fixes the expansion rate for the whole history of the Universe from birth to death.

General Relativity with FLRW metric constitutes the theoretical basis for the current fiducial cosmological model: ΛCDM. It states that the Universe is flat, homogeneous and isotropic; has a non-zero cosmological constant and its non-relativistic matter content is mainly composed by what is known as dark matter. Dark matter is a form of matter that is not on the Standard Model of High Energy Physics and interacts with the ordinary –a.k.a. baryonic– matter trough gravity (Figure 1.3). Latest constrains on the density of the different matter species by Planck Collaboration 2015 [15] can be found at Table 1.1.

1.2 The Cosmological Constant problem

The cosmological constant can be absorbed on the right-hand-side of the Equation 1.1 and interpreted as a constant matter term known as dark energy:

$$R_{\mu\nu} - \frac{1}{2} R g_{\mu\nu} = \frac{8\pi G_N}{c^4} T_{\mu\nu} - \Lambda g_{\mu\nu}. \tag{1.10}$$

With this matter term, assuming $\Omega_K = 0$, Equation 1.5 transforms into

$$H^2(t) = H_0^2 \left[\sum_i \Omega_i(t) + \Omega_\Lambda(t) \right], \tag{1.11}$$

where $\Omega_\Lambda(t) = \Omega_\Lambda^0$ is the dark energy density. This new term is a time-independent constant that has the same value on every location of the Universe. Thus, as the other matter species has a density that decreases with time, the dark energy density has only impact at late cosmic times.

This new term may be regarded as a new matter specie such that

$$\rho_\Lambda = \frac{3H_0^2}{8\pi G_N} \Omega_\Lambda. \tag{1.12}$$

Taking into account Equation 1.9 and Equation 1.12, an upper bound on the dark energy density can be established

$$\rho_\Lambda \leq \frac{3H_0^2}{8\pi G_N} \sim 10^{-47}\ \mathrm{GeV}^4. \tag{1.13}$$

Since this energy density fills the whole Universe and is an inherent property of the geometry of the Universe and hence of the Universe itself, from a physical point of view it can be identified as the energy of the vacuum [17–19]. Assuming that the Standard Model is valid up to the Planck scale, the energy density of the vacuum can be estimated to be [20]

$$\rho_{QFT} = \int_0^{1/L_P} dk \sqrt{k^2 + m^2} \frac{4\pi k^2}{(2\pi)^4} \sim 10^{71}\ \mathrm{GeV}^4, \tag{1.14}$$

where L_P is Planck's length. Thus, there's a miss-match between the amount of dark energy measured and that predicted by QFT of many orders of magnitude. It can be argued that although it is known that Planck's energy scale is the upper range of validity of Standard Model physics, nothing prevents that it starts to fail at lower scales. A lower bound on this point can be established as the Quantum Cromodynamics (QCD) cutoff scale ($\sim$ 200 MeV), leading to a vacuum energy density of

$$\rho_{QCD} = \int_0^{1/L_{QCD}} dk \sqrt{k^2 + m^2} \frac{4\pi k^2}{(2\pi)^4} \sim 10^{-3}\ \mathrm{GeV}^4, \tag{1.15}$$

reducing the tension between theory and experiment, but still being catastrophic. It is worth to remark that establishing the range of validity of the Standard Model at the QCD cutoff scale is an optimistic scenario for the cosmological constant, since latest LHC results have demonstrated its validity of the Standard Model up to 1 TeV.

It can be argued that the cosmological constant is not connected to High Energy Physics. Nevertheless, the energy of the quantum vacuum is still there and must be taken into account, not solving the discrepancy.

1.3 Theories for Dark Energy

As it has been stated previously, the small value of the cosmological constant can not be explained with the Standard Model of High Energy Physics. Thus, one can force the cosmological constant to be $\Lambda = 0$ and try to explain accelerated expansion of the Universe with other class of theories. The simplest approach is to postulate the existence of new exotic matter that has a negative pressure that drives the accelerated expansion. The other approach consist on postulating a new gravitational field equation by modifying Einstein's equation or starting from scratch.

1.3.1 Exotic matter fields

An explanation to the accelerated expansion of the Universe can be found on the presence on new quantum fields. The simplest case is known as quintessence and is defined as a scalar field (ϕ) that is added to the action defined at Equation 1.2 such that

$$S = \frac{c^4}{16\pi G_N} \int d^4x \sqrt{-g} R + S_\phi + S_M \tag{1.16}$$

with

$$S_\phi = \int d^4x \left[\frac{1}{2} g^{\mu\nu} \partial_\mu \phi \partial_\nu \phi - V(\phi) \right], \tag{1.17}$$

where $V(\phi)$ is the potential of the field. On the FLRW metric, this leads to a substance with pressure and density respectively

$$P_\phi = \frac{1}{2}\dot{\phi}^2 - V(\phi) \quad \text{and} \quad \rho_\phi = \frac{1}{2}\dot{\phi}^2 + V(\phi). \tag{1.18}$$

This can be parametrized as an ideal fluid with equation of state

$$w_{DE} = \frac{P_\phi}{\rho_\phi} = \frac{\dot{\phi}^2 - 2V(\phi)}{\dot{\phi}^2 + 2V(\phi)}. \tag{1.19}$$

Thus, it can be deduced that dark energy density evolves with the scale factor of the universe as

$$\Omega_\Lambda(t) = \Omega_\Lambda^0 [a(t)]^{-3(1+w_\phi)}. \tag{1.20}$$

The only possible candidate for dark energy as quintessence within the Standard Model of Particle Physics is the Higgs field, a complex scalar-field that fills the Universe and couples to gauge bosons giving them its mass. The potential of the field is given by

$$V(\phi) = \mu_H^2 \phi^\dagger \phi + \frac{1}{4}\lambda_H (\phi^\dagger \phi)^2, \tag{1.21}$$

with μ_H the mass term, λ_H the self-interaction of the field and $\phi, \phi^\dagger$ the Higgs field and its hermitian conjugate respectively. Since the potential of the field is time independent, this leads to an equation of state

$$w_{DE} = \frac{-2V(\phi)}{2V(\phi)} = -1, \tag{1.22}$$

recovering the cosmological constant solution. Thus, the cosmological constant can also be interpreted alternatively as the expected value of Higgs field at vacuum [21, 22]

$$\langle 0|\phi_0|0\rangle = \frac{|\mu_H|}{\sqrt{\lambda_H}} = \sqrt{\frac{1}{\sqrt{2}G_F}} = 246 \text{ GeV}^4, \tag{1.23}$$

not solving the discrepancy of several orders of magnitude with the cosmological constant energy density as given by Equation 1.13. Here G_F is the Fermi constant, that can be computed from the decay of the muon. The connection between the decay of the muon and the Higgs field comes from the fact that the decay is mediated by vector bosons, whose mass is given by the Higgs field:

$$\mu^- \to W^- + \nu_\mu \text{ and } W^- \to e^- + \bar{\nu}_e. \tag{1.24}$$

Other High Energy Physics potentials can be built from physics beyond the Standard Model, such us supergravity and supersymmetry [23–26], where different scalar potential can be found. Even more complicated theories with more fields that may interact between them can be postulated and will not be considered here since they are beyond the scope of this Thesis. A detailed description of all the models can be found at [27]. Nevertheless, a general phenomenological description can be made in terms of the equation of state of dark energy,

$$P_{DE} = w_{DE}\rho_{DE} \tag{1.25}$$

expanding the parameter w_{DE} in a power series of the scale factor

$$w_{DE}(t) = w_0 + w_a[1 - a(t)], \tag{1.26}$$

where w_0 denotes the value of the equation of state parameter at present and w_a is evolution –at first order– with time. The cosmological constant may be considered as an specific solution of this equation of state where

$$w_0 = -1 \quad \text{and} \quad w_a = 0. \tag{1.27}$$

The key difference between the cosmological constant and exotic forms of matter is that the latter theories provide a dark energy density that evolves trough the cosmic history.

1.3.2 Modified Gravity

Attempts to explain the existence of a cosmological constant from High Energy Physics side lead to a tension between General Relativity and the Standard Model. Possible new exotic fields that may explain late-time cosmic acceleration are walking a tightrope due to latest LHC results [28]. The remaining approach to explain the accelerated expansion of the Universe is to consider General Relativity as an approximate gravitational theory on the same way Newtonian gravity is the low-energy limit of Einstein's gravity. Extensions to General Relativity are known as modified gravity models.

In order to preserve the symmetries of General Relativity, the new field equations must be a function of the Ricci scalar. The most general class of those theories is known as $f(R)$ gravity [29, 30], and its approach is to let the action to be a general function (f) of the Ricci scalar:

$$S = \frac{c^4}{16\pi G_N}\int d^4x\sqrt{-g}f(R) + S_M, \tag{1.28}$$

that leads to the field equation

$$R_{\mu\nu} - \frac{1}{2}Rg_{\mu\nu} = \frac{8\pi G_N}{c^4}(T_{\mu\nu} + T^R_{\mu\nu}). \tag{1.29}$$

This field equation is similar to Equation 1.1 but has an additional term $T^R_{\mu\nu}$ that takes into account the additional curvature terms that can be modeled as a fluid on the same way as the energy-momentum tensor. The simplest case is $f(R) = R + \alpha R^n$ with $\alpha, n \in \mathbb{R}$, which has interesting cosmological solutions [31]. This theory has very distinctive phenomenology such as double Einstein rings with just one source galaxy on an strong lens regime [32] that –if found–, could be the smoking gun of these kind of theories. The existence of a double Einstein ring (SDSSJ0946+1006) has been reported [33], nevertheless it is a system with one lens and two sources at different redshifts, producing one ring of different diameter each.

More complicated models of modified gravity that may break the equivalence principle and the Lorentz symmetry can be considered but are not going to be treated here since they are beyond of the scope of this Thesis. For a review it can be consulted [34]. The usual approach to explore the modifications to General Relativity [35] is to consider the departures of the metric. On the Newtonian gauge, the FLRW line element of can be parametrized with the Newtonian and the lensing potential; Φ, Ψ respectively [35]:

$$ds^2 = a^2(\tau)[-(1+2\Psi)d\tau^2 + (1-2\Phi)dx_i dx^j], \tag{1.30}$$

with

$$2\nabla^2\Phi(a,k) = \frac{8\pi G_N}{c^2}a^2\mu(a,k)\bar{\rho}_M\delta_M(a,k) \quad \text{and} \quad \gamma(a,k) = \frac{\Phi(a,k)}{\Psi(a,k)}, \tag{1.31}$$

where $\bar{\rho}_M$ is the average matter density, δ_M its fluctuations and k is the wavenumber of the potentials. Here μ and γ parametrize the departures from General Relativity, that is the specific case with

$$\mu(a,k) = 1 \quad \text{and} \quad \gamma(a,k) = 1. \tag{1.32}$$

It is important to remark that the zoo of all the departures from General Relativity plus cosmological constant –including the addition of new fields–, may be unified into a single parametrization known as Parametrized Post-Friedmann Framework [36].

1.4 Probes for Dark Energy

The nature of Dark energy can be constrained using different cosmological probes [37] by measuring the w_0, w_a parameters of its equation of state or the potentials Σ, γ of modified gravity. The determination of these parameters can be split in two classes of probes: geometric and large-scale-structure tests.

Geometrical measurements exploit the fact that the distances measured on cosmological scales depend on the metric tensor of the Universe, that is affected by the energy content of the Universe and the gravitational theory used. These measurements include: the barion acoustic oscillation peak-scale (BAO), the SNIa distance-ladder, Alcock-Paczynski [38] tests and integrated Sachs-Wolfe (ISW) effect. On the other side, large-scale-structure probes are based on the measurement of the inhomogeneities of the matter density field at different moments of the cosmic history, which depend on the matter/dark-energy ratio and gravitational theory used. They include: the cluster-count evolution with redshift, redshift-space-distortions (RSD), clustering, lensing and the cosmic microwave background (CMB).

The combination of different cosmological probes leads to more accurate measurements at the same time it breaks degeneracies on the determination of the cosmological parameters [37, 39]. Nevertheless, multiprobe constrains suffer from the correlation of the different methodologies. In addition, if the different probes are provided by the same experiment, they must also take into account the correlation of the different sources of systematic errors [40–43]. Thus, the inclusion of an specific measurement on a multiprobe analysis, that is highly correlated with other probes or is very noisy, may no lead to a significant improvement of the cosmological constrain.

Weak-lensing magnification is a low signal-to-noise measurement with many sources of systematic errors [44] that is produced by the same physical entity as the gg-lensing, which has higher signal-to-noise (see chapter 2 for a full explanation of magnification and gg-lensing). Thus, the inclusion of magnification on a multiprobe analysis does not lead to an effective improvement of the measurement. This requires the use of magnification on environments and regimes that other probes can not reach.

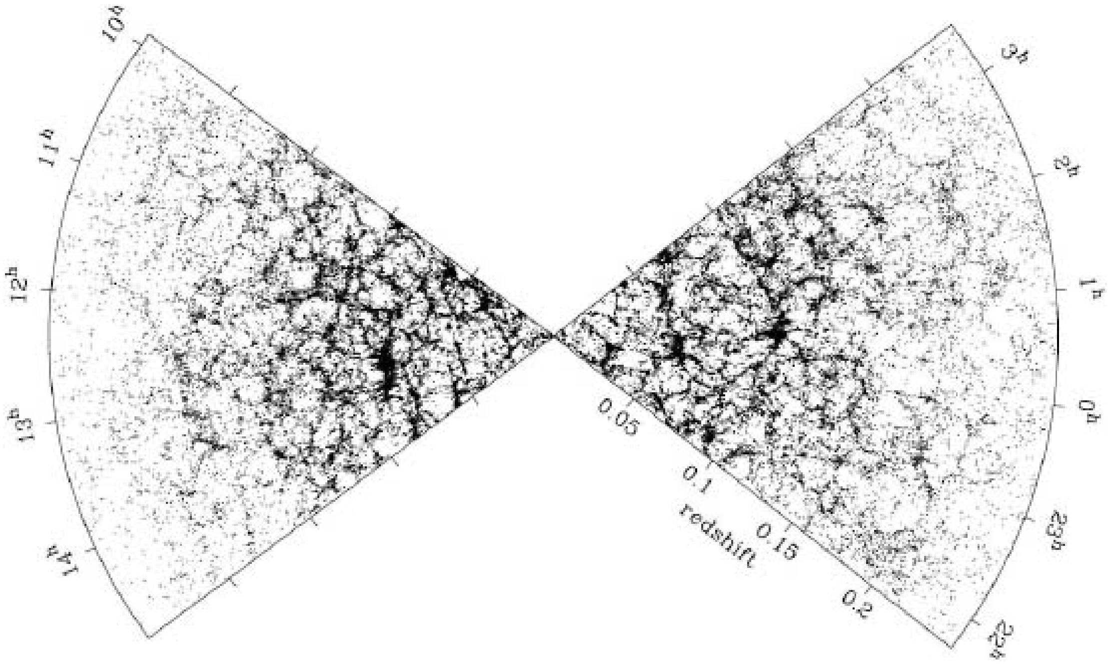

Figure 1.4: Large-scale-structure of the Universe. Each dot represents the position of a galaxy. Image credit: 2 Degree Field Survey.

The strength of magnification is that it allows to measure directly the matter profile of the large-scale-structures that conform the Universe. The true matter structures of the Universe are only accessible directly trough gravitational lensing due to the presence of dark matter. Since dark matter is not visible and interacts only trough gravity, assumptions on how the visible- –baryonic- – and dark- matter assemble together must be made on measurements other than gravitational lensing, introducing nuisances on the measurement. One of those structures are known as voids, which are the emptiest regions of the cosmic web (see Figure 1.4).

Since voids have a lower matter content than the average Universe, their gravitational evolution is more dominated by dark energy. Thus, void properties are different depending on the nature of dark energy. If the abundance of large voids on the Universe is considered, it has been reported that its number increases in $f(R)$ gravity models [45] since the abundance of dark matter halos is altered [46]. Nevertheless, if the shape of the void is measured, its ellipticity can be used as a probe for the parameters of the equation of state of dark energy [47–50], since the structure growth-factor on the line-of-sight has a variation due to the dark energy content, whereas on the transverse plane, growth-factor is constant. Finally, the radial distribution of matter around the center of a void –known as void profile– has demonstrated to be different on $f(R)$ theories and General Relativity [51–56]. Thus, by simply measuring the void matter profile, constrains on dark energy can be made.

This implies that the direct determination of the matter profile of voids by weak-lensing magnification, constitutes a promising and independent new probe on dark energy, alternative to multiprobe constrains.

1.5 Current status of Dark Energy constrains

The latest and more precise results constraining dark energy are provided by the Planck Collaboration 2015 results from the analysis of the Cosmic Microwave Background (CMB) [57].

Dark enery as an exotic form of matter, is determined by measuring the parameters of the equation of state (w_0, w_a) and their value can be seen at Figure 1.5. Results are compatible with General Relativity plus cosmological constant, the uncertainty on the parameters of the equation of state does not allow to exclude many models, specifically the type of models that predict a value of the equation of state close to that of the cosmological constant but whose equation of state evolves with cosmic time –or equivalently, redshift–, since current precision on the determination of this evolution is still limited as it can be deduced from Figure 1.6. Constrains on Modified Gravity models are also given in terms of the modified gravity potentials μ, η and Σ (see Figure 1.7 and Figure 1.8).

The latest results from the Sloan Digital Sky Survey (SDSS) and its upgrade BOSS, provide several measurements that, although they do not constrain directly dark energy theories, show a good agreement with the flat-ΛCDM paradigm. These probes include: Alcock-Paczynski tests [58], the clustering of galaxies [59], baryon acoustic oscillations (BAO) [60, 61] and redshift-space distortions [62].

Although the Planck Collaboration 2015 and SDSS/BOSS results agree between them and seem to favour cosmological constant as dark energy, there are some measurements that are in tension with Planck Collaboration 2015.

Riess et al. latest direct determination of the Hubble constant using the cosmological distance ladder (parallax-cepheids-SNIa) [63], show a discrepancy at the 3σ level with the Hubble constant measured by Planck Collaboration 2015.

CFHTLens & KiDS-450 Collaborations weak gravitational lensing analysis show tension on the $\Omega_M - \sigma_8$ plane with Planck Collaboration 2013 [64] and 2015 CMB measurements if a General Relativity plus cosmological constant scenario is considered [65, 66]. This tension may be alleviated if other models are considered, such as non-zero curvature and dark energy models [67]. Nevertheless, discrepancies could also be produced by systematic effects [68, 69].

A weak-lensing analysis by Leauthaud et al. [70] of CFHTLens & CMASS data using weak gravitational lensing, show a lower signal amplitude that the one predicted measuring the clustering of the lens sample. In addition weak gravitational lensing measurements on the $\Omega^0_M - \sigma_8$ plane have a discrepancy on the 3σ level with Planck Collaboration 2013 measurements on a cosmological constant scenario. Nevertheless, discrepancies are interpreted in terms of new physics on

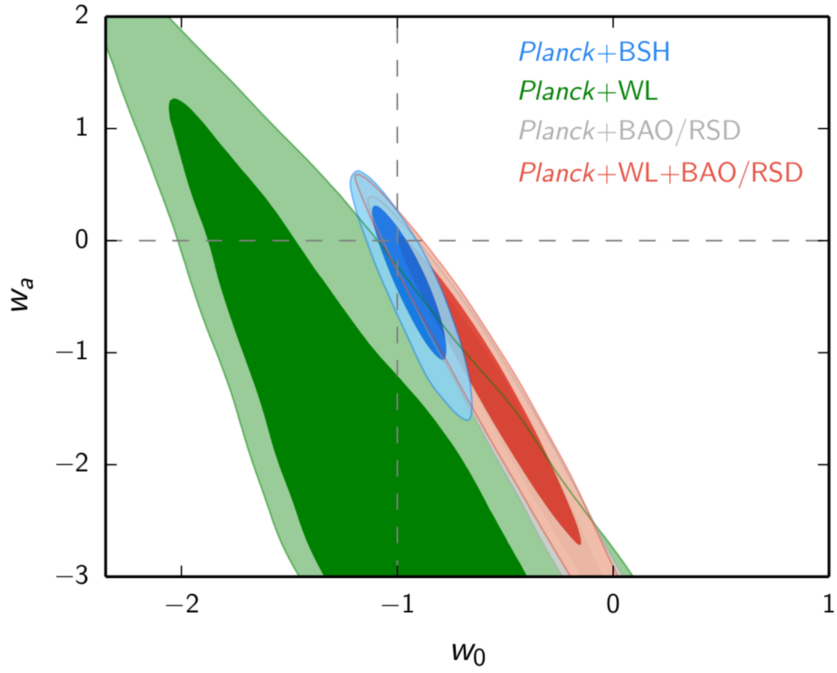

Figure 1.5: One- and two- sigma contours of the equation of state of dark energy w_0, w_a. The intersection of dashed lines is the cosmological constant. Results obtained from Planck Collaboration 2015 results [57].

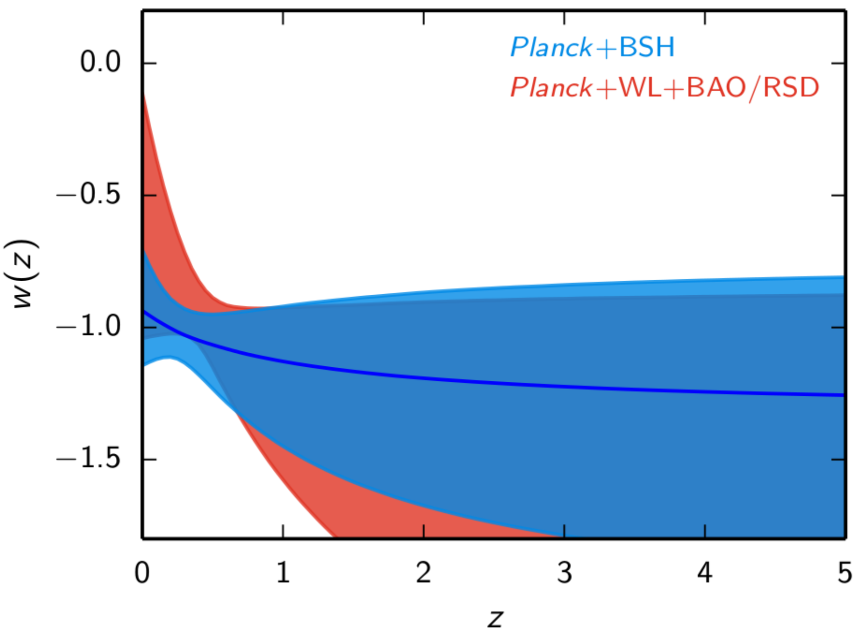

Figure 1.6: One-sigma confidence interval of the equation of state of dark energy as a function of redshift $w_{DE}(z)$ and one-sigma confidence interval. Results obtained from Planck Collaboration 2015 results [57].

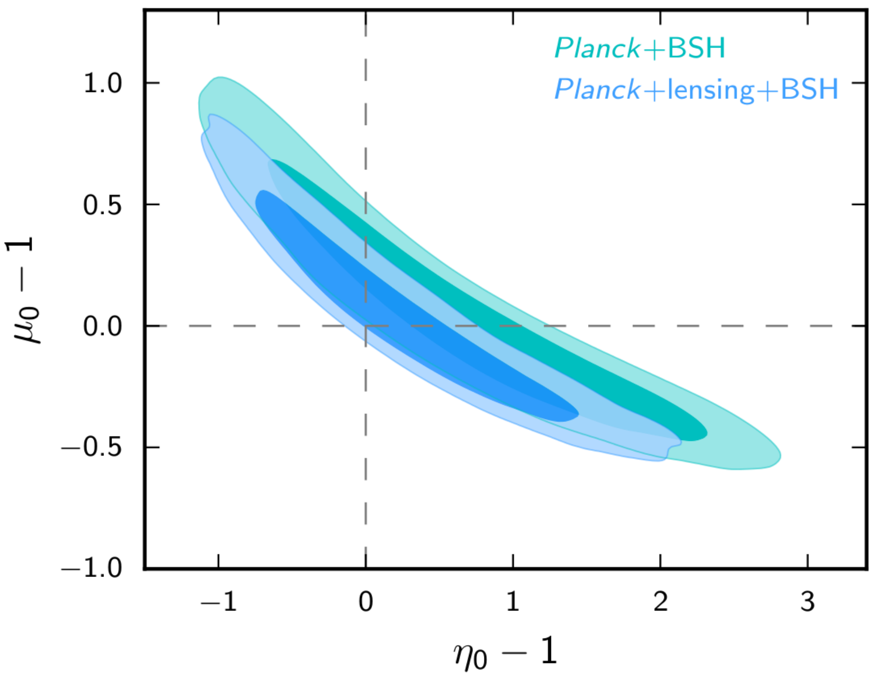

Figure 1.7: One- and two- sigma modified gravity potentials at present μ_0, η_0. Dashed line is General Relativity plus cosmological constant. Results obtained from Planck Collaboration 2015 results [57].

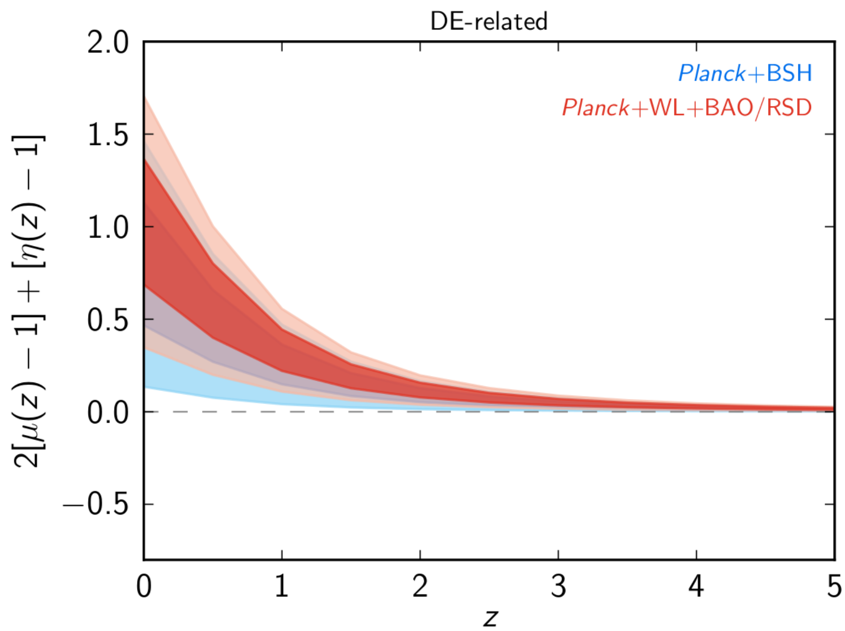

Figure 1.8: One- and two- sigma of the sum of the modified gravity potentials. Dashed line is General Relativity plus cosmological constant. Results obtained from Planck Collaboration 2015 results [57].

the astronomy side: halo occupation distribution (HOD) and baryonic physics.

Recently, a dynamical dark energy scenario has shown to solve these tensions when combining severeal cosmological probes (weak-lensing, SNIa, BAO, and CMB) [71]. An independent work has also shown that dynamical dark energy can solve these tensions combining Planck Collaboration 2015 with Riess et al., SDSS BAO and CFHTLens measurements [72]. Nevertheless, constrains are still limited.

As it has been described, current individual constrains on dark energy are not precise enough to determine which model is the correct explanation of the accelerated expansion of the Universe. Nevertheless, current cosmological model –ΛCDM–, has demonstrated to be a solid theory that explains a wide range of physical effects and has passed the most stringent tests including gravitational waves [73, 74]. Although a tension exists between different probes that may be alleviated in a non-cosmological constant scenario, caution is needed and special attention is required to do a proper systematic error estimation. This requires additional probes and redundant measurements of the same physical observable but with different sources of systematic errors. We have entered in the precision cosmology era.

§ § §

This Thesis is devoted to the analysis of weak-lensing magnification as part of the Dark Energy Survey Collaboration. Data analysis is carried out on two different data-sets of the mentioned experiment with two different goals each. The first analysis is carried out on the Science Verification data-set, aiming the detection of the magnification signal and the development of new techniques of systematic error mitigation. Once the magnification signal has been detected, a new analysis on the Year 1 data-release is made with the methodology that has been established previously. Year 1 analysis is qualitatively different since its goal is to measure the convergence profile of voids to use it as a probe for dark energy.

The next chapter (chapter 2), describes the general weak-lensing formalism and explains the magnification theory and its observational effects. The experiment where this Thesis has been developed –the Dark Energy Survey– is briefly described on chapter 3. The core of this work is found on chapter 4, where the analysis of the Science Verification data and the Year 1 data are described extensively, concluding on chapter 5.

2. Gravitational Lensing Theory

As it has been stated on chapter 1, the gravitational fields acts on the energy-momentum tensor. Thus, massless particles that are carriers of energy –such as photons– are also affected by gravity, leading to a bending of light rays. The first experimental determination of the gravitational light bending is by Dyson et al. in 1919 [75], four years after the publication of General Relativity. On this work, the observed apparent position of stars close to the Sun during a solar eclipse were measured and compared with their positions when the Sun is not in front of them. The positions of the stars where shifted as predicted by General Relativity.

Dyson et al. measurement of the gravitational deflection of the light emitted by a background object –a.k.a. source–, relied on the fact that the object that causes of the light deflection –a.k.a. the lens–, can be removed by its own seasonal motion. Nevertheless, this limits the measurement of gravitational light deflection to objects within the Milky Way. The study of the large-scale-structure of the Universe requires the use of extragalactic objects, implying that the object that acts as lens can not be removed, complicating the measurement.

One specific case of the gravitational light deflection happens when the observer, lens and source are aligned. This problem has cylindrical symmetry and leads to a very specific solution: the Einstein ring (Figure 2.1) [76]. On this configuration, the image of the background galaxy is distorted forming a ring around the lens galaxy, that its located at its center. The size of the ring is determined only by the mass of the lens and the distances of the lens and the source:

$$\theta_E = \sqrt{\frac{4G_N M}{c^2}\frac{d_{LS}}{d_L d_S}}, \tag{2.1}$$

where G_N is Newton's gravitational constant, M the mass of the lens, d_{LS} the lens-source angular diameter distance and d_L, d_S are the angular diameter distance to the lens and the source respectively.

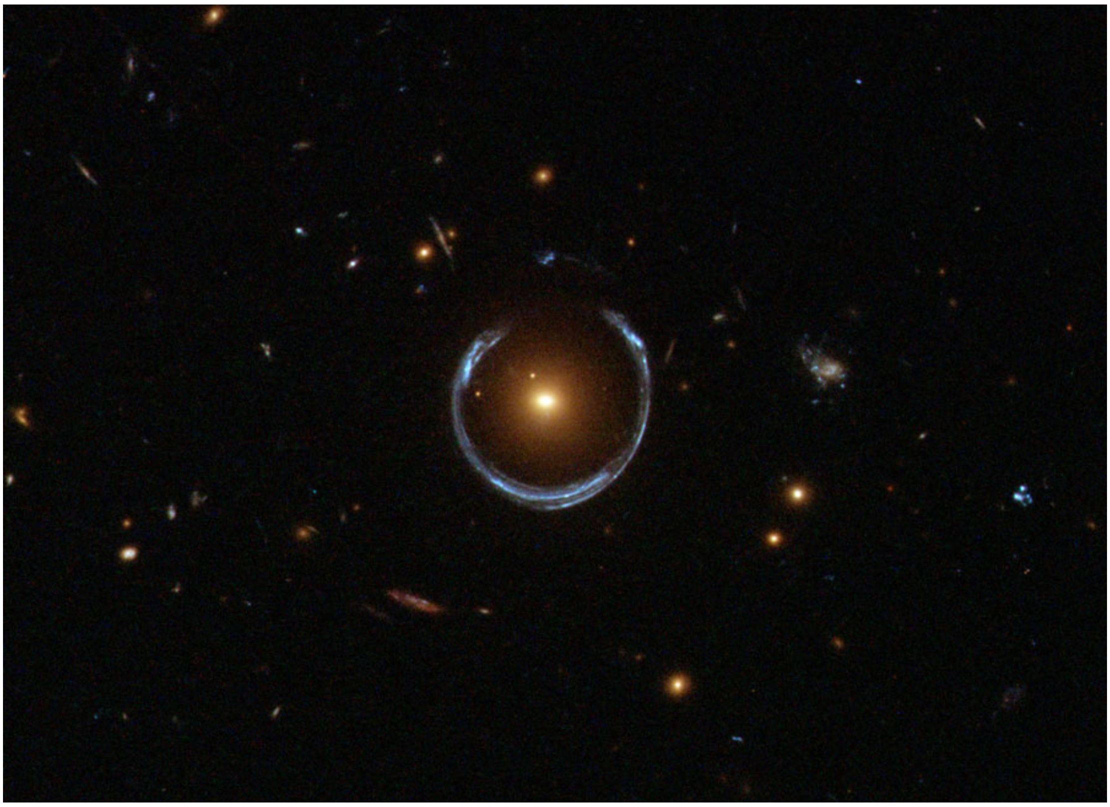

Figure 2.1: Image form the Hubble's Wide Field Camera 3 showing an Einstein ring. Central galaxy is the luminous red galaxy LRG-3-757. The blue annulus is a distant galaxy located behind the LRG. Image credit: NASA.

Finding Einstein rings may be a product of serendipity or digging hard on wide-field images [77]. Nevertheless, the probability of finding a system where observer-lens-source are aligned is very remote and only a small number of Einstein rings are known (~ 20 on the Dark Energy Survey Science Verification data). A general solution, where the system is not aligned can be found with the gravitational lens equation.

2.1 Lens Equation on Gravitational Fields

Since all the photons emitted by the source are bended coherently by the lens, the axis observer-lens constitute an optical convergent system. Thus a lens equation can be deduced using Geometrical Optics with the deflection angle ($\hat{\alpha}$) of a light ray –photon trajectory– given by General Relativity [37, 78–83]:

$$\hat{\alpha} = \frac{4G_N M}{\xi c^2}. \tag{2.2}$$

Here M is the mass of the point-particle (lens hereafter), G_N is Newton's constant, c the speed of light and ξ the closest encounter distance (a.k.a. impact paramenter). Using Figure 2.2 as reference and defining θ as the observed and β the real lens-source angle, it can be deduced that

$$\beta = \theta - \frac{D_{ds}}{D_s}\hat{\alpha}(D_d\theta) = \theta - \alpha(\theta), \tag{2.3}$$

where D_{ds}, D_s and D_d are the source-lens, observer-source and observer-lens co-moving distances.

Considering now an extended matter distribution, with density $\rho(\vec{r})$, where the observer is located at the origin. The position vector can be splitted such that

$$\vec{r} = r_{\|}\hat{r}_{\|} + \vec{r}_{\perp}, \tag{2.4}$$

where $r_{\|}\hat{r}_{\|}$ denotes the position on the direction defined by the axis observer-lens (line-of-sight or LoS hereafter) and $\vec{r}_{\perp}$ denotes a 2D vector on the plane transverse to the line-of-sight. Thus, the total matter distribution that the photon goes trough from the source to the observer is given by

$$\Sigma(\vec{r}_{\perp}, r_{\|}^S) = \int_0^{r_{\|}^S} dr_{\|}\rho(r_{\|}, \vec{r}_{\perp}), \tag{2.5}$$

where $\vec{r}^S$ is the position of the source and the quantity Σ is called the surface density. Taking into account the flat-sky approximation –that is, all the transverse planes to LoS are parallel– and summing to all the lens positions, Equation 2.2 becomes

$$\hat{\vec{\alpha}}(\vec{r}_{\perp}, r_{\|}^S) = \frac{4G_N}{c^2}\int d^2\vec{r}_{\perp}\Sigma(\vec{r}_{\perp}, r_{\|}^S)\frac{\vec{r}_{\perp}^S - \vec{r}_{\perp}}{|\vec{r}_{\perp}^S - \vec{r}_{\perp}|^2}. \tag{2.6}$$

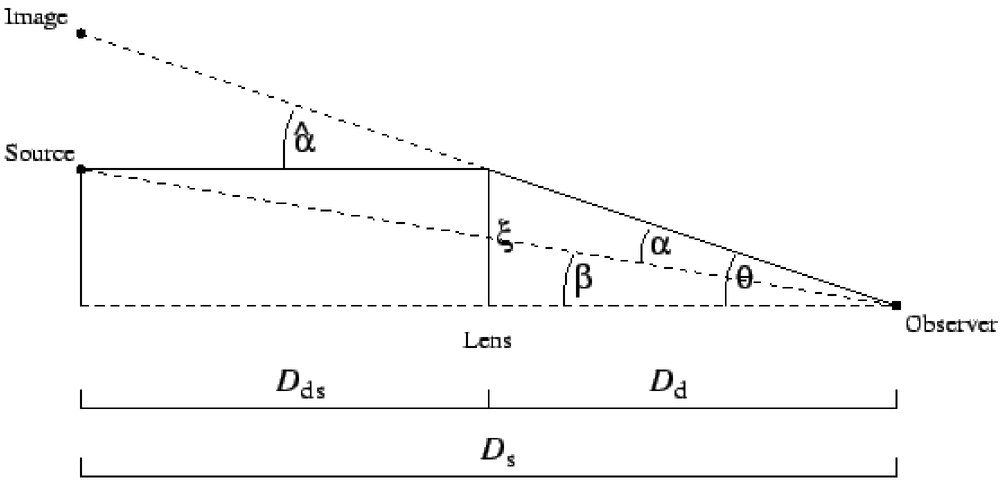

Figure 2.2: Optical system of the gravitational lensing caused by a point mass. Solid line is the actual photon trajectory. Dashed lines are the apparent trajectories with and without lensing. The distances D_s, D_d, D_{ds} are expressed in comoving coordinates.

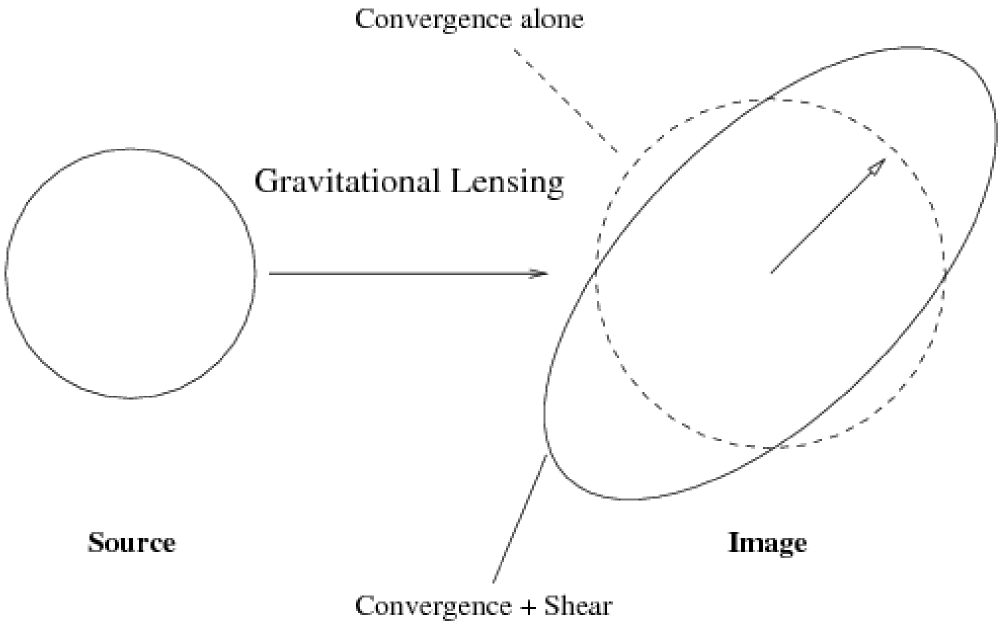

Figure 2.3: Weak-lensing distortion of an extended spherical object. Convergence leads to an isotropic enlargement, whereas shear produces an elongation/shrink along one axis.

This leads to a deflection angle

$$\hat{\vec{\alpha}}(\vec{r}_\perp, r_\parallel^S) = \frac{1}{\pi} \int d^2\vec{r}_\perp \kappa(\vec{r}_\perp, r_\parallel^S) \frac{\vec{r}_\perp^S - \vec{r}_\perp}{|\vec{r}_\perp^S - \vec{r}_\perp|^2}, \tag{2.7}$$

where the convergence (κ) and critical density (Σ_c) has been defined such that

$$\kappa(\vec{r}_\perp, r_\parallel^S) = \frac{\Sigma(\vec{r}_\perp, r_\parallel^S)}{\Sigma_c} \text{ with } \Sigma_c = \frac{c^2}{4\pi G_N} \frac{D_s}{D_d D_{ds}}. \tag{2.8}$$

As weak-lensing wide-field surveys start to proliferate, the limit of validity of the flat-sky approximation is being reached [84–86]. Defining the lensing potential as

$$\psi(\vec{r}_\perp, r_\parallel^S) = \frac{1}{\pi} \int d^2\vec{r}_\perp \kappa(\vec{r}_\perp, r_\parallel^S) \ln |\vec{r}_\perp^S - \vec{r}_\perp|, \tag{2.9}$$

the deflection angle can be written as the gradient of the lensing potential on the transverse plane

$$\hat{\vec{\alpha}}(\vec{r}_\perp, r_\parallel^S) = \nabla_\perp \psi(\vec{r}_\perp, r_\parallel^S) \tag{2.10}$$

and the convergence as its laplacian,

$$\kappa(\vec{r}_\perp, r_\parallel^S) = \frac{1}{2} \nabla_\perp^2 \psi(\vec{r}_\perp, r_\parallel^S). \tag{2.11}$$

Thus, the lens equation from Equation 2.3 results

$$\vec{\beta} = \vec{\theta} - \nabla_\perp \psi(\vec{r}_\perp, r_\parallel^S). \tag{2.12}$$

Taking into account the definition of the lensing potential, it can also be written in terms of the Newtonian gravitational potential (Φ):

$$\psi(\vec{r}_\perp, r_\parallel^S) = \frac{D_{ds}}{D_s D_d} \frac{2}{c^2} \int dr_\parallel^S \Phi(D_d \vec{r}_\perp, r_\parallel^S). \tag{2.13}$$

Thus, gravitational lensing is a direct probe for the underlying gravitational field.

2.2 Weak Gravitational Lensing

In addition to the change in the observed position of the source, considering no absorption nor emission of photons between the source and the observer, Liouville's theorem implies that the surface brightness of the source (I_S)is conserved,

$$I_S(\vec{r}_\perp) = I_S[\vec{\beta}(\vec{r}_\perp)]. \tag{2.14}$$

Considering the weak-field regime, the lensing map can be linearized such that

$$I_S(\vec{r}_\perp) = I_S[\vec{\beta}_0 + \mathcal{J}(\vec{r}_{\perp 0})(\vec{r}_\perp - \vec{r}_{\perp 0})], \tag{2.15}$$

where $\mathcal{J}(\vec{r}_\perp)$ is the jacobian matrix. By the integration-by-substitution theorem of calculus, the integral of the surface brightness at the lensed and un-lensed coordinate systems are related by

$$\int I_S(\vec{\beta}) d\vec{\beta} = \det(\mathcal{J}) \int I_S[\vec{\beta}(\vec{r}_\perp)] d\vec{r}_\perp, \tag{2.16}$$

where $\det(\mathcal{J})$ denotes the determinant of the jacobian matrix. Thus, defining the luminosity of an extended object as the integral of its surface brightness, the luminosity for the cases with and without gravitational lensing (L_μ, L_0 respectively) are related by

$$L_\mu = \frac{1}{\det(\mathcal{J})} L_0 = \mu L_0, \tag{2.17}$$

where μ is called the magnification factor and is defined as de inverse of the determinant of the jacobian matrix of the lensing map.

Taking into account that the jacobian matrix is given by $\mathcal{J} = (\hat{n}_\perp \cdot \nabla_\perp)\vec{\beta}$ with $\hat{n}_\perp$ a unit vector on the plane transverse to LoS, by Equation 2.12 the jacobian can be expressed as

$$\mathcal{J} = (\hat{n}_\perp \cdot \nabla_\perp)\vec{r}_\perp - \mathcal{J} = (\hat{n}_\perp \cdot \nabla_\perp)\nabla\psi, \tag{2.18}$$

resulting finally

$$\mathcal{J}(\vec{r}_\perp) = \left(\delta_{ij} - \frac{\partial^2\psi}{\partial r_i \partial r_j}\right) = \begin{pmatrix} 1-\kappa-\gamma_1 & -\gamma_2 \\ -\gamma_2 & 1-\kappa+\gamma_1 \end{pmatrix}. \tag{2.19}$$

Here κ is the convergence, an isotropic shape distortion and γ_1, γ_2 is the shear, an elongation/shrink on the shape along one of the axis (Figure 2.3).

Taking into account the Born approximation –that is, the light rays of a source galaxy are deflected by only one lens–, the derivatives of the previous equation can be evaluated on the unlensed coordinates.

2.2.1 Magnification

As it has been demonstrated at the previous section, gravitational lensing increases the observed luminosity on an extended object [87–91] such that $L_\mu = \mu L_0$ with

$$\mu = \frac{1}{(1-\kappa)^2 + \gamma_1^2 + \gamma_2^2} \simeq 1 + 2\kappa, \tag{2.20}$$

where on the last step it has been used that $1 \gg \kappa \gg \gamma$. Taking into account the definition given at Equation 2.8, the convergence suffered by the photons emitted by a source located on the sky direction $\hat{n}$ and redshift z is given by

$$\kappa(\hat{n}, z) = \frac{1}{2}\frac{\Sigma(\hat{n}, z)}{\Sigma_c}. \tag{2.21}$$

Using the definition given at Equation 2.5 and the poisson equation for the gravitational field this leads to

$$\kappa(\hat{n}, z) = \int_0^z dz' \frac{r(z')[r(z) - r(z')]}{r(z)} \nabla_\perp \Phi(\hat{n}, z'), \tag{2.22}$$

where $r(z)$ is the comoving distance at redshift z and Φ the gravitational potential. Expressing now the gravitational potential as an homogeneus therm plus a perturbation ($\Phi = \bar{\Phi} + \delta_\Phi$), the previous equation can be expressed as a funcion of the matter density contrast (δ_M)

$$\nabla^2\Phi(\hat{n}, z) = \nabla^2\delta_\Phi(\hat{n}, z) = 4\pi G a^2 \bar{\rho}\delta_M(\hat{n}, z), \tag{2.23}$$

where $a = 1/(1+z)$ is the scale factor and $\bar{\rho}$ is the average density. This leads finally to [92, 93]

$$\kappa(\hat{n}, z) = \frac{3H_0\Omega_M(z)}{2c^2}\int_0^z dz' \frac{r(z')[r(z) - r(z')]}{(1+z')r(z)}\delta_M(\hat{n}, z). \tag{2.24}$$

The convergence, is the physical observable of Magnification and it traces the matter on the direction of line of sight whereas shear proves the matter on the transverse direction. This makes magnification and shear complementary measurements of the same phenomena. The dependence of magnification is usually splitted into two pieces: the lensing kernel,

$$\mathcal{K}(z) = \frac{r(z')[r(z) - r(z')]}{(1+z')r(z)}. \tag{2.25}$$

and the matter density contrast (δ_M). The lensing kernel contains only geometrical information and, for a given set of cosmological parameters, it is fixed. On the other side, the matter density contrast depends strongly on the population of galaxies selected as lens sample.

The convergence of the foreground sample can be probed tracing the three effects that it produces on the background sample:

- **Change of the observed density:** The increase of the observed luminosity of the galaxies, allows to see sources that if there were no lensing, would be below our observational threshold nearby the location of the lenses. At the same time, an stretching of the solid angle behind the lenses causes a drop in the number density. This two effects compete between them and who is over the other depends on the slope of the number counts of the sources. Thus, at the neighbourhood of the lenses, a change of the number density respect to the average is produced. This is known as number-counts magnification.
- **Shift on the observed magnitude:** Since the increase of luminosity due to gravitational lensing is a short range effect, a shift on the observed magnitudes may be detected nearby the positions of the lenses. This requires, in principle, the knowledge of the unlensed magnitude of the sources. Nevertheless, although galaxies have a large variety of magnitudes, it can be assumed that, they are randomly distributed. Thus shifts on the magnitudes respect to the average can be detected.
- **Size enlargement:** All the effects above are a consequence that the meanwhile surface brightness is conserved, a size enlargement is produced. This effect can be statistically measured despite the fact that the unlensed size is not known. Nevertheless, since galaxies have a large variety of shape and size that is strongly related to its evolution and age, no homogeneity assumption can be made and require the definition of the *fundamental plane* [94]. That

kind of work is beyond the scope of this Thesis and further information can be found at Huff & Graves 2014 [95].

Traditionally all these probes have been used independently, but the ideal scenario would be a three-way combination that may lead to a cancellation or better estimation of systematic errors.

As it has been mentioned before, the knowledge of the unlensed properties of the sources is physically impossible. Thus, all the observable quantities must be formulated in terms of changes of its variation respect the ensemble average with the distance to the lenses. The statistical way to do this is the two-point angular correlation-function. This method, provides a measurement of the average convergence profile of the lenses ($\kappa(\theta)$) as a function of its angular distance θ of a point to the lens.

Estimation of $\kappa(\theta)$ with the number counts technique

The two-point angular cross-correlation between the lens (L) and the source (S) is defined as [96]

$$\omega_{LS}(\theta) = \langle \delta_O(\hat{n}, z_L, f_\mu)\delta_O(\hat{n}', z_S, f_\mu)\rangle_\theta. \tag{2.26}$$

Where $\delta_O(\hat{n}, z_L, f_\mu)$ is the observed galaxy density-contrast on the sky direction $\hat{n}$ and redshift z_L with flux limit f_μ. Since due to magnification galaxies beyond the observable threshold will appear nearby the lenses introducing a non-uniform distribution of galaxies. Thus the observed galaxy density contrast can be expressed as

$$\delta_O(\hat{n}, z, f_\mu) = \delta_g(\hat{n}, z) + \delta_\mu(\hat{n}, z, f_\mu), \tag{2.27}$$

where δ_g is the intrinsic galaxy-density contrast (that is, without magnification) and δ_μ is the density contrast due to magnification. Thus Equation 2.26 becomes

$$\omega_{LS}(\theta) = \langle\delta_g(z_L)\delta_g(z_S)\rangle + \langle\delta_g(z_L)\delta_\mu(z_S)\rangle + \langle\delta_\mu(z_L)\delta_g(z_S)\rangle + \langle\delta_\mu(z_L)\delta_\mu(z_S)\rangle. \tag{2.28}$$

Taking into account that $0 < z_L < z_S$, and that the lens and the source sample are well redshift separated, the only non vanishing term is

$$\omega_{LS}(\theta) = \langle \delta_g(\hat{n}, z_L)\delta_\mu(\hat{n}, z_L, f_\mu)\rangle_\theta. \tag{2.29}$$

Let define the magnification density contrast on the sky direction $\hat{n}$ as

$$\delta_\mu(\hat{n}, z, f_\mu) = \frac{N_\mu(\hat{n}, z, f_\mu)}{N_0(\hat{n}, z, f_0)} - 1, \tag{2.30}$$

where $N_0(\hat{n}, z, f_0)$ is the un-lensed cumulative number counts of sources located at redshift z, that is, the number of sources with observed flux greater than the threshold f_0. Conversely, $N_\mu(\hat{n}, z, f_\mu)$ is the lensed cumulative number counts affected by magnification.

Magnification by gravitational lenses increases the observed flux of background objects allowing to see fainter sources by an amount $f_\mu = f_0/\mu$. At the same time, it stretches the solid angle behind the lenses, reducing the surface density of sources an amount $N_\mu = N_0/\mu$, which translates into the density contrast as:

$$\delta_\mu(\hat{n}, z, f_\mu) = \frac{N_\mu(\hat{n}, z, f_\mu)}{\mu N_\mu(\hat{n}, z, \mu f_\mu)} - 1. \tag{2.31}$$

The cumulative number counts can be locally parametrized as a power law

$$N_\mu(\hat{n}, z, f_\mu) = A \left(\frac{f_\mu}{f_*}\right)^{\alpha(f_\mu)}, \tag{2.32}$$

where A, f_* are constant parameters and $\alpha(f_\mu)$ a function of the flux limit. Substituting this into Equation 2.31

$$\delta_\mu(\hat{n}, z, f_\mu) = \mu^{\alpha(f_\mu)-1} - 1. \tag{2.33}$$

Taking into account the weak-lensing approximation $\mu \simeq 1 + 2\kappa$ along with Equation 2.20 and translating from fluxes to magnitudes this results

$$\delta_\mu(\hat{n}, z, m) = 2\kappa(\hat{n}, z)[\alpha(m) - 1] \tag{2.34}$$

with

$$\alpha(m) = 2.5 \frac{d}{dm}\left[\log N_\mu(m)\right]. \tag{2.35}$$

Thus Equation 2.26 becomes

$$\omega_{LS}(\theta) = 2[\alpha(m) - 1]\langle \delta_g(\hat{n}, z_L)\kappa(\hat{n}', z_S)\rangle_\theta = [\alpha(m) - 1]2\kappa(\theta), \tag{2.36}$$

where $\kappa(\theta)$ is the convergence profile of the selected lenses.

Estimation of $\kappa(\theta)$ with magnitude-shift magnification technique

The magnitude-position-angular correlation function between the lens sample (L) and the source sample (S) is defined as

$$\varphi_{LS}(\theta) = \langle \delta_g(z_L, \hat{n})\delta_m(z_S, \hat{n}')\rangle_\theta. \tag{2.37}$$

Where, as on the last section $\delta_g(z, \hat{n})$ is the galaxy density contrast at redshift z on the sky direction $\hat{n}$ and δ_m is the magnitude shift[1], defined as

$$\delta_m(z, \hat{n}) = m_\mu(\hat{n}, z) - m_0(\hat{n}, z), \tag{2.38}$$

where m_μ is the lensed magnitude and m_0 the unlensed magnitude. Taking into account that, as it has been demonstrated previously

$$f_\mu(\hat{n}, z) = \mu(\hat{n}, z)f_0(\hat{n}, z) \Leftrightarrow m_\mu(\hat{n}, z) - m_0(\hat{n}, z) = -2.5\log\mu(\hat{n}, z), \tag{2.39}$$

where on the last step it has been converted from fluxes to magnitudes. Thus, taking into account that

$$\log(\mu) \simeq \log(1 + 2\kappa) \simeq 2\kappa, \tag{2.40}$$

[1]Do not confuse with δ_M, the matter density contrast.

the Equation 2.37 results finally

$$\varphi_{LS}(\theta) = -5\langle\delta_g(\hat{n}, z_L)\kappa(\hat{n}', z_S)\rangle = -5\kappa(\theta), \tag{2.41}$$

where $\kappa(\theta)$ is the convergence profile of the lenses.

Nevertheless, reddening by the inter-galactic medium can also produce –unlike gravitational lensing– wavelength-dependent magnitude-shifts. Thus, the lensed-plus-reddened fluxes are given by

$$f_\mu(\hat{n}, z, \lambda_\eta) = \mu(\hat{n}, z) f_0(\hat{n}, z) e^{-\tau(\lambda_\eta)}, \tag{2.42}$$

that converted to magnitudes results in

$$m_\mu(\hat{n}', z, \lambda_\eta) - m_0(\hat{n}', z, \lambda_\eta) = -2.5 \log \mu + \frac{2.5}{\ln 10}\tau(\lambda_\eta), \tag{2.43}$$

where $\tau(\lambda_\eta)$ is the optical depth at the wavelength λ_η. The dust and the lensing components can be disentangled by defining the color-excess angular correlation function ($E^{\eta\nu}$) between two-wavelengths $\lambda_\eta, \lambda_\nu$,

$$E^{\eta\nu}_{LS}(\theta) = \langle\delta_g(\hat{n}, z_L)[m_\mu(\hat{n}', z_S, \lambda_\eta) - m_\mu(\hat{n}', z_S, \lambda_\nu)]\rangle_\theta. \tag{2.44}$$

Since gravitational lensing is acromatic, the only dependence with the wavelength comes from the extinction law

$$E^{\eta\nu}_{LS}(\theta) = \frac{2.5}{\ln 10}\langle\delta_g(\hat{n}, z_L)[\tau(\hat{n}', z_S, \lambda_\eta) - \tau(\hat{n}', z_S, \lambda_n u)]\rangle. \tag{2.45}$$

Modeling the wavelength dependence of the optical depth as

$$\tau_\eta = \tau(\lambda_\eta) = \tau_V \left(\frac{\lambda_V}{\lambda_\eta}\right)^\gamma, \tag{2.46}$$

where τ_V is the optical depth at the V-band filter, λ_V is the wavelength of the V-band filter and $\gamma \sim 1$ is a constant parameter. Thus, the color-excess cross-correlation results finally

$$E^{\eta\nu}_{LS}(\theta) = \lambda_V(\lambda_\eta^{-1} - \lambda_\nu^{-1})\frac{2.5}{\ln 10}\langle\delta_g(\hat{n}, z_L)\tau_V(\hat{n}', z_S)\rangle. \tag{2.47}$$

At a wide field survey with several broad-band band-pass filters the scale dependence of the optical depth, $\tau_V(\hat{n}, z_S)$ can be constrained.

2.2.2 Shear

From the Jacobian of the lensing map, it can be deduced that the transformation is not isotropic producing an elongation along one of the axis $(r_1, r_2) = \vec{r}_\perp$. Thus, an intrinsically round galaxy is seen as elliptical. On the case of elliptical galaxies, statistically they present a global ellipticicity. From the definition of Equation 2.19, the shear components are given by:

$$\gamma_1(\vec{r}_\perp) = -\frac{1}{2}\left(\frac{\partial^2\psi}{\partial r_1^2} - \frac{\partial^2\psi}{\partial r_2^2}\right) \text{ and } \gamma_1(\vec{r}_\perp) = -\frac{\partial^2\psi}{\partial r_1 \partial r_2}. \tag{2.48}$$

The shear fields γ_1, γ_2 can be expressed as Fourier series such that:

$$\tilde{\gamma}_{1,2}(\vec{k}_\perp) = \int \gamma_{1,2}(\vec{r}_\perp) e^{-i\vec{k}_\perp \cdot \vec{r}_\perp} d^2\vec{r}_\perp \tag{2.49}$$

and

$$\gamma_{1,2}(\vec{r}_\perp) = \frac{1}{(2\pi)^2} \int \tilde{\gamma}_{1,2}(\vec{k}_\perp) e^{i\vec{k}_\perp \cdot \vec{r}_\perp} d^2\vec{k}_\perp. \tag{2.50}$$

Expressing the differential equation at the Fourier space with the usual approach $\partial/\partial r_1 \to ir_1$ it leads to

$$\gamma_1(\vec{k}_\perp) = \frac{1}{2}(r_1^2 - r_2^2)\tilde{\psi}(\vec{k}_\perp) \text{ and } \gamma_2(\vec{k}_\perp) = \frac{1}{2} r_1 r_2 \vec{\psi}(\vec{r}_\perp) \tag{2.51}$$

Considering a plane-wave perturbation of the lensing potential, it is useful to align the axis of the perturbation with those of the shear field such that

$$\tilde{\gamma}_E(\vec{k}_\perp) = \cos(2\phi_{\vec{k}_\perp})\tilde{\gamma}_1(\vec{k}_\perp) + \sin(2\phi_{\vec{k}_\perp})\tilde{\gamma}_2(\vec{k}_\perp) \tag{2.52}$$

and

$$\tilde{\gamma}_B(\vec{k}_\perp) = \cos(2\phi_{\vec{k}_\perp})\tilde{\gamma}_1(\vec{k}_\perp) - \sin(2\phi_{\vec{k}_\perp})\tilde{\gamma}_2(\vec{k}_\perp). \tag{2.53}$$

Resulting finally that

$$\tilde{\gamma}_E(\vec{k}_\perp) = \vec{k}_\perp^2 \tilde{\psi}(\vec{k}_\perp) \text{ and } \tilde{\gamma}_B(\tilde{k}_\perp) = 0 \tag{2.54}$$

The fact that γ_B is zero, constitutes a necessary (but not sufficient) proof for the lack of systematic effects on any shear measurement.

Reaching this point, two kinds of two-point statistics can be build: the point-shear[2] and the shear-shear two-point angular-correlation functions. From this two, we will only focus to gg-lensing due to its direct connection to magnification.

The gg-lensing.
Defining $\tilde{\epsilon}$ as the observed ellipticity, taking into account shear distortions it can be expressed as:

$$\tilde{\epsilon} = \tilde{\epsilon}_i + \tilde{\gamma}, \tag{2.55}$$

where $\tilde{\epsilon}_i$ is the intrinsic ellipticity of the galaxy. As stated previously, without loss of generality, shear coordinates can be rotated. Thus, let define the tangential shear γ_t as

$$\gamma_t = -[\cos(2\phi_{\vec{k}_\perp})\tilde{\gamma}_1(\vec{k}_\perp) + \sin(2\phi_{\vec{k}_\perp})]\tilde{\gamma}_2(\vec{k}_\perp) = -\gamma_E. \tag{2.56}$$

On the new coordinates, this leads to

$$\epsilon = \epsilon_i + \gamma_E, \tag{2.57}$$

where $\tilde{\epsilon}, \tilde{\epsilon}_i$ are the ellipticity on the new coordinates. Let $p(\epsilon)$ the distribution of ellipticity of the sources. At the small distortion regime, assuming that ellipticity is isotropic, it follows that

$$p(\epsilon) = p(\epsilon_i) + \gamma_t \cos 2\phi \frac{\partial p(\epsilon)}{\partial \epsilon}. \tag{2.58}$$

[2]This is usually called galaxy-galaxy- (or gg-) lensing.

Here $\phi_{\vec{k}_\perp}$ is the angle of orientation of the principal axis of the galaxy. Integrating over all the ellipticity, they can be translated to orientation angle,

$$p(\phi) = \frac{2}{\pi}\left[1 - \langle\gamma_t\rangle \cos 2\phi \left\langle\frac{1}{\epsilon}\right\rangle\right]. \tag{2.59}$$

Thus, measuring the ellipticity –or orientation angles–, shear E-modes can be measured, probing directly the underlying lensing potential.

Tangential shear can be estimated to be

$$\langle\gamma_t\rangle = -\frac{\Delta\Sigma}{\Sigma_c}, \tag{2.60}$$

with

$$\Delta\Sigma = \bar{\Sigma}(\theta) - \Sigma(\theta), \tag{2.61}$$

where $\bar{\Sigma}(\theta)$ denotes the average surface density on an disk of angular size θ. Thus the tangential shear can be related to the convergence profile as

$$\langle\gamma_t\rangle = -[\bar{\kappa}(\theta) - \kappa(\theta)]. \tag{2.62}$$

The last equation demonstrates that gg-lensing and magnification are produced by the same physical effect. Nevertheless, they have different systematic effects. This can be exploited in order to produce accurate and reliable magnification measurements.

2.3 Theoretical expressions for $\kappa(\theta)$

As it has been stated on the previous section, the convergence profile is the physical observable for both magnification and gg-lensing. Thus, in order to connect the measurements with a cosmological model, a theoretical expression for it must be provided. Depending on the nature of the lenses considered –that is, whether the lenses are galaxies, voids, clusters or troughs–, the approach may differ.

On this section, are only provided the solutions for galaxies and voids. Although troughs will also be considered on the data analysis, it is beyond the scope of this Thesis and it is still part of an ongoing project. A simple solution can be found on Gruen et al. [97]. Nevertheless, a more general and complete solution is still to be published.

The simplest solution for the convergence profile, is for a sample of galaxies. Taking into account the definition of κ

$$\kappa(\theta) = \langle\delta_g(\hat{n}, z_L)\kappa(\hat{n}', z_S)\rangle_\theta, \tag{2.63}$$

if a linear, constant and redshift-independent galaxy-bias (b_L) is considered; a relation between the galaxy density contrast δ_g and matter density contrast δ_M can be established:

$$\delta_g(\hat{n}, z_L) = b_L\delta_M(\hat{n}, z_L). \tag{2.64}$$

Thus, the convergence profile is given by

$$\kappa(\theta) = b_L \langle \delta_M(\hat{n}, z_L)\kappa(\hat{n}', z_S)\rangle_\theta. \tag{2.65}$$

If it is considered that the convergence field $\kappa(\hat{n})$ can be expressed also as a function of the matter density contrast by Equation 2.24 and Equation 2.22:

$$\kappa(\theta) = b_L \left\langle \delta_M(\hat{n}, z_L) \left[\int_0^z dz' \frac{r(z')[r(z) - r(z')]}{r(z)} 4\pi G a^2 \bar{\rho} \delta_M(\hat{n}, z) \right] \right\rangle. \tag{2.66}$$

This leads finally to [98]:

$$\kappa(\theta) = \frac{3H_0^2\Omega_M^0}{c^2} \int_0^\infty dz'_L \frac{\phi_L(z'_L)}{1+z'_L} \int_{z'_L}^\infty dz'_S \phi_S(z'_S) \frac{r(z'_L)[r(z'_S) - r(z'_L)]}{r(z'_S)} \times \tag{2.67}$$
$$\int_0^\infty \frac{dkk}{2\pi} P_M(k, z'_L) J_0[k\theta r(z'_i)],$$

where ϕ_L, ϕ_S are the redshift distributions of the lens and source sample respectively, P_M the matter power spectrum of the lens sample and J_0 is the zero-th order Bessel function.

The calculation of the convergence profile for a void needs to assume a void profile. A general LTB solution on General Relativity for voids can be found at [99–101],

$$\delta(r_v) = \delta_0 g(a) \left(1 - \frac{2}{3}\frac{r_v^2}{r_0^2}\right) \exp\left(-\frac{r_v^2}{r_0^2}\right), \tag{2.68}$$

where r_v is the radial comoving distance **on the system of coordinates centered at the void**, r_0 the radial size of the void, δ_0 the central underdensity and $g(a)$ the growth factor **not normalized at present**. On the system of coordinates centered on the observer and considering non-spherical voids, this leads to the Kovacs & Garcia-Bellido void-profile (KGB):

$$\delta_{KGB}(\theta, z) = \delta_0 g(a) \left[1 - \frac{2}{1+2q^2}\left(\frac{r_\parallel^2}{r_0^2} + \frac{q^2 r_\perp^2}{r_0^2}\right)\right] \exp\left[-\left(\frac{r_\parallel^2}{q^2 r_0^2} + \frac{r_\perp^2}{r_0^2}\right)\right], \tag{2.69}$$

where $q^2 = 1 - e^2$ with e the ellipticity of the void and

$$r_\parallel = r(z)\cos\theta - r(z_v) \tag{2.70}$$
$$r_\perp = r(z)\sin\theta. \tag{2.71}$$

Here $r(z)$ is the radial comoving distance at redshift z, whereas z_v is the redshit of the center of the void and θ the angular separation form the center of the void. From Equation 2.69 and Equation 2.8, the convergence profile around a single void can be obtained:

$$\kappa(\theta) = \frac{1}{1}\frac{\Sigma_{KGB}(\theta)}{\Sigma_c}, \tag{2.72}$$

where the surface density is given by

$$\Sigma_{KGB}(\theta) = \int_0^\infty dz' \bar{\rho}_M(z')[\delta_{KGB}(\theta, z') - 1]. \tag{2.73}$$

Here the $\bar{\rho}_M(z')$ is the matter average density of the Universe at redshift z', given by

$$\bar{\rho}(z') = \frac{\Omega_M^0 \rho_c}{(1+z')^3} \tag{2.74}$$

with ρ_c the critical energy density of the Universe.

3. The Dark Energy Survey

The Dark Energy Survey (DES) [102] is a $grizY$ photometric galaxy-survey that has as main scientific goal to shed light on the nature of the Dark Energy.

The four probes used by DES to unravel the nature of Dark Energy are: the number of clusters as a function of redshift, the measurement of the peak-scale of the baryon acoustic oscillations (BAO), the weak gravitational lensing of galaxies and the measurement of the Hubble diagram with type Ia Supernovae (SNIa). By the end of five years of observations, DES will cover 5000 deg^2 of the Southern Hemisphere up to magnitude $i < 24.0$ at the 10σ detection level. Taking this into account, this survey is expected to measure 10000 clusters up to redshift 1.0, 200 million galaxy-shapes for weak-lensing, 300 million galaxies for BAO and 3000 SNIa up to redshift 1.0. The power of DES resides on the combination of all the probes braking degeneracies on the cosmological parameter phase-space leading to a precision better than the 5% on the parameters w_0 and $\Delta w_a < 0.2$ on the equation of state of the Dark Energy.

DES is an international collaboration formed by about 500 scientists from more than 20 institutions from: USA, Spain, UK, Brazil, Germany and Switzerland. The Collaboration has built a very sensitivity camera, DECam (see Figure 3.1 and Figure 3.2), that has been mounted at the 4-m Victor M. Blanco Telescope[1] at the Cerro Tololo Inter-American Observatory (CTIO), located at La Serena (Chile).

3.1 The DECam

The DECam (Dark Energy Camera), is the main instrument of the experiment. It is composed mainly by:

- The 570 megapixel focal plane, formed by 70 CCDs.

[1] This is the same telescope where Schmidt and Perlmutter performed some of the observations leading to the Nobel Prize in 2010 for the discovery of Dark Energy.

- Low-noise readout electronics.
- Wide-field optical corrector, producing 2.2 $\deg^2$ field of view.
- Filter and shutter system.
- Hexapod for stability.

Since DES is going to observe very high redshifted galaxies, the used CCDs have been specifically designed at Lawrence Berkeley National Laboratory to detect red light. In order to do so, these CCDs are ten times thicker –250 μm– than conventional ones[2]. This results in a quantum efficiency >80% on the 600-950 nm range, >60% on the 400-600 nm and >50% on the 900-1000 nm. The DECam focal plane consist of the following types of CCDs:

- Science array: formed by 62 CCDs with 2048×4096 pixels. Each pixel is $15\mu m$ of side that, at the prime focus fot the Blanco Telescope, results on 0.27 arc-seconds on the sky.
- Four 2048×2048 guider CCDs.
- Eight 2048×2048 focus and alignment CCDs.

To minimize the noise and dark currents due to the electronic system, DECam operates on an environment cooled by liquid nitrogen at 180 K and a vacuum of $\sim 10^{-9}$ atm.

The whole readout process takes 17 seconds (about the same slewing-time of the telescope). Readout electronic boards were produced and designed in Spain at CIEMAT and IFAE.

3.2 Survey strategy

The total amount of time awarded to DES at CTIO to reach the total area to the nominal depth on the five photometric bands is of 525 nights over a 5-year period. The rest of the nights, DECam is available to the scientific community. The tank-shaped footprint, that can be seen at Figure 3.3 is not casual but is optimized for the several probes.

- The *canyon* located at the equator, is known as stripe-82 and overlaps with several spectroscopic surveys such as SDSS, to calibrate the photometric redshifts (photo-z hereafter).
- The rounded shape –*the body*– is intended to have the largest available scale for BAO measurement.
- The lower part –*the wheels*– is designed to overlap with the South Pole Telescope (SPT) to measure the Sunyaev-Zel'dovich effect.

The DES observations can be split in two: the transient survey and the wide-field survey.

3.2.1 The transient survey

The transient survey is designed to measure SNIa. Selected small portions of the sky –known as the supernovae fields– are surveyed from time to time to look for supernovae explosions by looking objects that are not always present and measure its luminosity curve as a function of time. Although it is designed to SNIa

[2]Sensitivity to long wavelengths is increased when passing trough more silicon.

Figure 3.1: DECam mounted at the focus of the Victor Blanco Telescope. Image credit: M. Garcia-Fernandez

Figure 3.2: Location of the 4-m Victor Blanco Telescope at Cerro Tololo. Chilean Andes. Image credit: M. Garcia-Fernandez

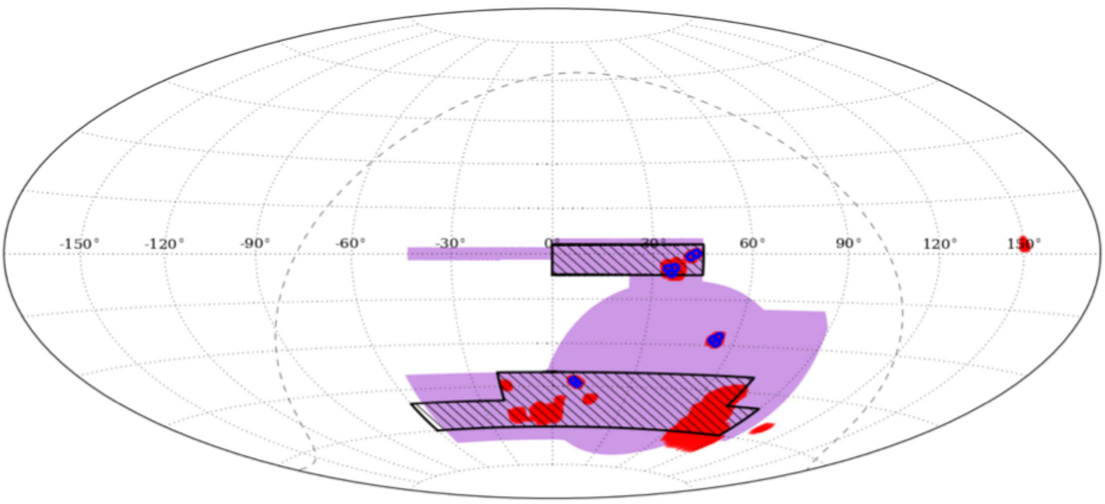

Figure 3.3: DES footprint on equatorial coordinates. Purple area is the total area that DES will cover at the end of the five years (Y5). Red areas -that overlap with the purple- are the Science Verification observations. Shaded areas are the first year campaign of observations (Y1). Dark blue regions are the SNIa fields. Dotted line represent the galactic plane. Image credit: The DES Collaboration.

astronomy, some ancillary Solar-System astronomical results as been reported, such as Jupiter-trojan and trans-neptunian detection and searches for the known planet-9. These ancillary physics also use the wide-field to increase the area.

3.2.2 The wide-field survey

The wide field survey is intended for the rest of the probes for Dark Energy along with some Milky-Way astrophysics. To cover the whole footprint, the sky has been divided on a grid of half square-degree patches known as tiles. Each tile is visited 10 times on each band along the 5-year-period to reach the full depth. The regions to survey are defined at the beginning of the campaign of observations and which band is observed at an specific night is decided based on general observing conditions of that night.

3.2.3 The night operations at CTIO

A typical night of observations, if sky is not overcast and no earthquake threatens the life of the observers, starts in the afternoon taking zeros of the camera and the dome-flats. Then, after the evening twilight, three standard stars are photographed to calibrate the photometry. These, are well known stars with very well defined and measured photometric properties. After that, the wide-field survey starts. When the supernovae fields are visible –and time requirements are fulfilled–, they are surveyed, returning to the wide-field survey when they are done. Some time before the morning twilight, other three standard stars are photographed, finishing the night. All the night operations are the same except if some transient alarm us received. In this case, DES points to the place where the transient has been produced to look for an optical counterpart.

3.3 The data reduction pipeline

The data reduction that goes from images to science-ready catalogs of galaxies is carried at the NCSA[3]. The first step is to correct by the calibration of zeropoints and the dome flats. Then, the different exposures of the same tile for a given band –single-epoch images– are combined into a single image on a procedure called co-addition –multi-epoch image–. This procedure allows the increase of the observed depth respect to each individual single-epoch image (Figure 3.4). This multi-epoch images will constitute the measurement images for each band. Nevertheless, to reach the DES nominal depth, images are detected on the image produced by the co-addition of the $r+i+z$ multi-epoch images. Co-additon of the objects is made by the software SWARP and the detection and photometric measurements is made with SEXTRACTOR in dual mode. Nevertheless, shape and photometry given by SEXTRACTOR do not reach the precision level required for the shear analysis, so the photometry for this analysis is made with IM3SHAPE and NGMIX.

[3]National Center for Supercomputing Applications. Illinois (USA).

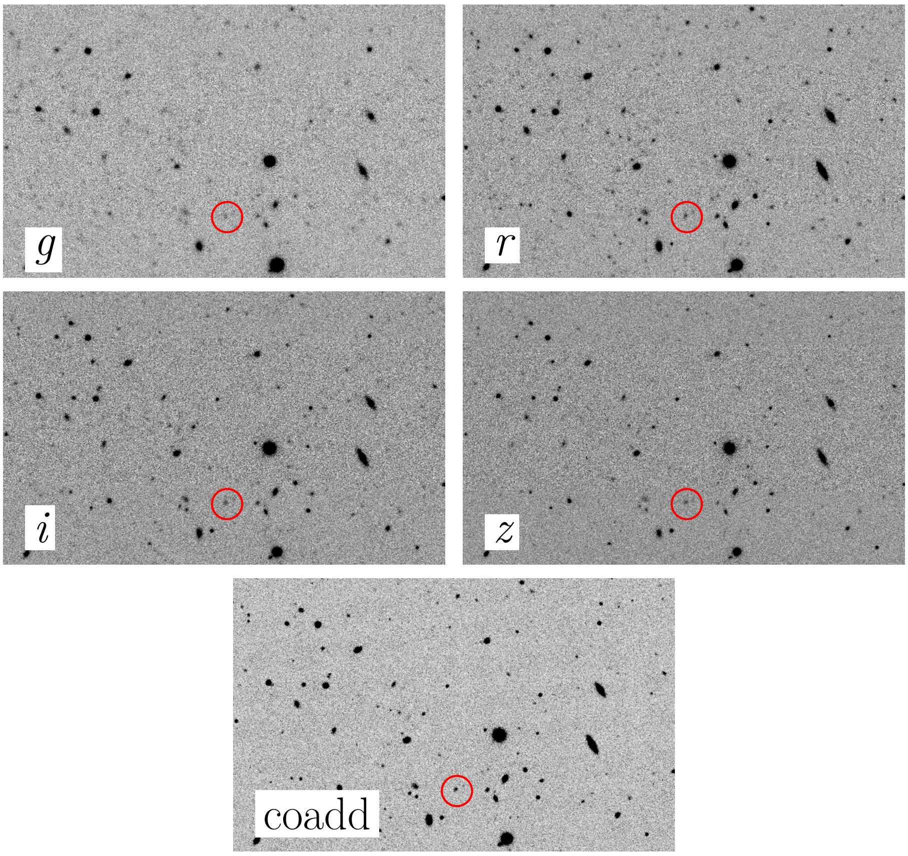

Figure 3.4: Comparison of the multi-epoch image for the *griz* bands with the detection coadd. Images are taken from DES-database for a region of the tile DES0419-4914 after the Y1 epoch. Red circle denotes an object that is detected at the coadd image but at the individual image is not. Image credit: M. Garcia-Fernandez & The DES Collaboration.

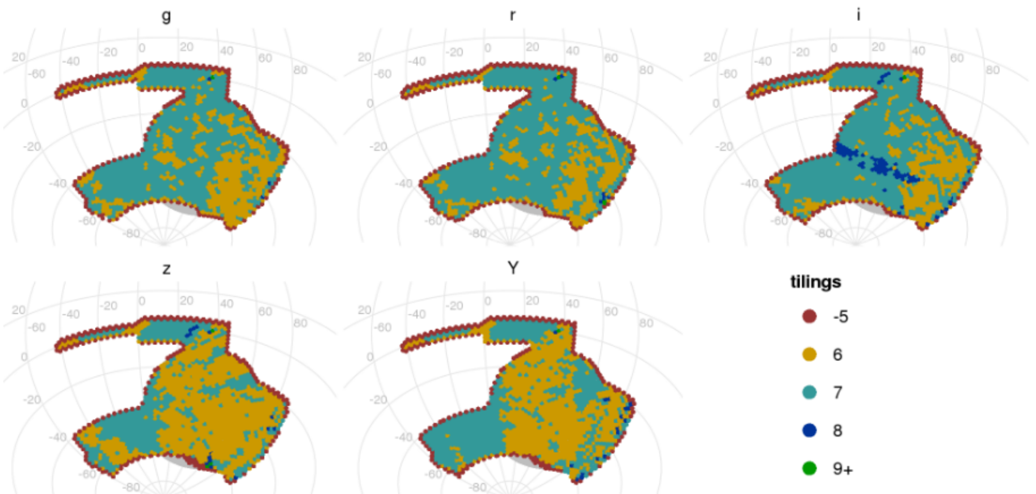

Figure 3.5: DES coverage at the end of Year 4 observations campaign for the *grizY* photometric bands. All the area has at least 6 tiles out of 10. It can be also seen that there is plenty of area with 7 tiles. Image credit: The DES Collaboration.

3.4 Current status and latest results

The Dark Energy Survey began its journey on 2005, starting the data acquisition on 2013 with the Science Verification. By the end of February 2017, the Year 4 observation campaign has ended (Figure 3.5). The Year 3 reduction pipeline from images to galaxy-catalogs has just finished and is still under inspection, so the most recent data-set that is being used for Cosmology analysis, is the Year 1 release (Figure 3.6 and Figure 3.7). Due to logistics and computing time, the Year 2 data release has been folded with the one of Year 3.

Currently, no constrains on dark energy has been made. Nevertheless several other works on Cosmology has been provided, such as strong-lensing [76, 103, 104], Sunyaev-Zel'dovich [105], voids and troughs [97, 106], tests of log-normality [107], clusters [108], weak-lensing [109–115] and large-scale-structure correlations with CMB [111, 116, 117].

Constrains on the cosmological parameter space provided by DES are based on the Science Verification shear analysis [118, 119]. Nevertheless, the most powerful measurement is produced by the combination of clustering with gg-lensing [120] on the $\sigma_8 - \Omega_M$ plane. Although results provided are still not sensitive to decide whether CFHTLens or Planck 2015 is right, it is a remarkable milestone for DES to provide such a competitive results with just the 3% of the planed total area.

But not everything is about dark energy at DES. Several other results has been provided [121]: searches for trans-neptunian objects (TNOs), Jupiter-trojans and main belt asteroids, characterization of variable stars, detection and characterization of Milky-Way satellite galaxies and gravitational-wave follow-up.

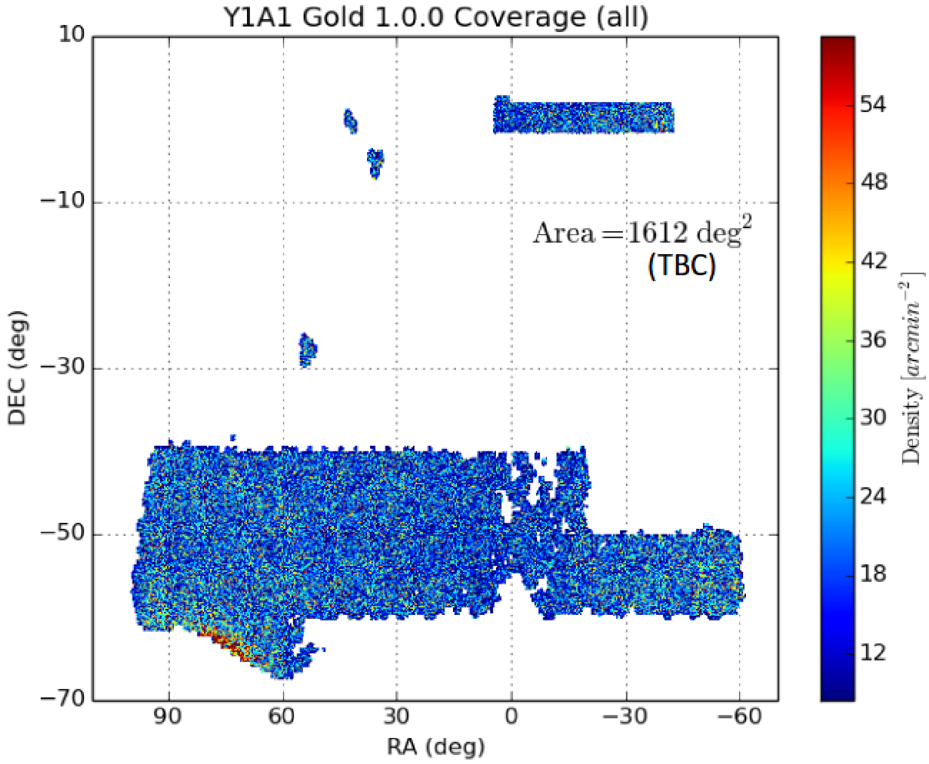

Figure 3.6: DES Year 1 spatial distribution of objects on equatorial coordinates. Image credit: The DES Collaboration.

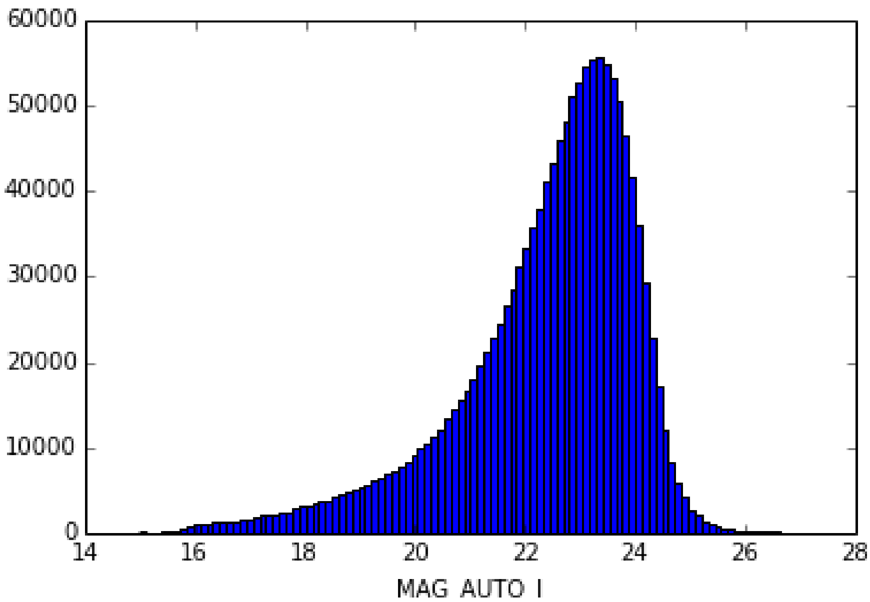

Figure 3.7: DES Year 1 magnitude distribution of objects on the i-band (arbitrary normalization). Image credit: The DES Collaboration.

4. Magnification in DES

Extensive wide-field programs have allowed accurate measurements of weak-lensing effects. Previous magnification measurements involve the use of very massive objects as lenses, such as luminous red galaxies (LRGs) and clusters [122–125], or high redshift objects as sources, such as Lyman break galaxies (LBGs) [126, 127], quasars (QSOs) [128–133] and sub-mm sources [134] to improve signal-to-noise ratio. In addition to the number count technique used on this Thesis, other observational effects produced by magnification have been measured as well: the shift in magnitude [135], flux [136] and size [95].

On this chapter, first the methodology to measure magnification is described and validated with simulations. Then, the methodology is used to measure the magnification signal at the Dark Energy Survey Science Verification data (SV). Finally, the same technique used at the DES-SV data is employed to measure the convergence profile of voids and troughs.

It is worth to remark that, as it has been defined at chapter 2, given both the redshift of the lenses and the sources, the convergence is a two-dimensional scalar field that is independent on the selected lens or source sample. Nevertheless, by choosing the suitable lens sample, different parts of the log-normal distribution of the convergence field [107] can be probed, leading to a different convergence profile.

4.1 Measuring Magnification through Number Count

As it has been described at chapter 2, the amplitude of the magnification signal is dependent on two factors: the number-count slope parameter $(\alpha - 1)$ and the lensing kernel, that for a given lens sample, depends on the redshift of the source sample. LBGs and QSOs has been traditionally used on magnification studies as sources since they have an steep magnitude distribution, leading to a high value of $\alpha - 1$. In addition, this population of galaxies is located at very high redshift ($2 \lesssim z \lesssim 4$), leading to a high lensing efficiency and a clean redshift separation between the lens and source sample. Nevertheless, this population of galaxies has much less density than the general population of galaxies, feature that can prevent the measurement of a magnification signal for low-area surveys. In addition, the selection of a population of LBGs involve the known as *dropout* technique, that requires the development of a custom data-reduction pipeline just to select this specific population of galaxies. For large-area surveys such as DES and LSST, the amount of computing time to run the data-reduction pipeline is enormous (~ 1 year), reaching manpower and infrastructure limitations.

The caveats related to the use of LBGs and QSOs as sources can be avoided by selecting galaxies from the general population of galaxies, that is, not selecting an specific subset of the full sample of galaxies). Then only redshift cuts are imposed in order to separate the lens and source samples. This approach has the advantage that the density of the source sample is more populated, reducing significantly the shot-noise. Nevertheless, the accuracy on the determination of the redshift on broad-band galaxy-surveys –such as DES– is very limited, introducing an important source of systematic errors that must be avoided and carefully taken into account.

In addition to the lens-source redshift overlap, magnification suffers from several systematic errors based on the photometry [44, 137], such as: depth-inhomogeneities, patchiness of the zero-point correction and calibration, or shifts on the magnitude determination due to wrong sky-background subtraction. The important reduction of shot-noise on wide-field surveys requires the development of new techniques to estimate these systematic errors.

The use of the general population of galaxies on shallow small-area surveys is mandatory to reach a significance that allows the detection of the magnification signal. On wide-area surveys the use of this population is not necessary although new studies can be made if it is used. Having a very dense population of galaxies as sources allows to use a set of lenses that are less numerous: voids and troughs. This allows to produce new physics analysis.

The usual approach that can be found on the literature to measure magnification is to use the *optimal weighting* technique [98]. This methodology can be summarized as follows:

1. Split data sample into two well-separated photo-z bins, termed lens and source. Splitting must be done minimizing the overlap between the true redshift distributions of the samples. Otherwise, by Equation 2.28, an additive signal is introduced.
2. Weight each source galaxy by its *optimal weight*.
3. Compute the two-point angular cross-correlation between the lens and the unique source sample.

The weight of the i-th galaxy (w_i) is given by:

$$w_i = \alpha_S(m_i) - 1, \tag{4.1}$$

where $\alpha_S(m_i)$ is the number-count slope given by Equation 2.35 and m_i is the magnitude of the i-th galaxy. This procedure allows to obtain the maximum signal-to-noise. Nevertheless, this weighting makes hard to model the impact of the different systematic effects on the measured signal.

As an alternative approach the following procedure is proposed:

1. Split the data sample into two well-separated photo-z bins, termed lens and source. Splitting must be done minimizing the overlap between the true redshift distributions of the samples. Otherwise, by Equation 2.28, an additive signal is introduced.
2. For each photometric band, define several subsamples from the source sample using different values for the maximum (threshold) magnitude. This is made in order to trace the evolution of the amplitude of the magnification signal with the number count slope (see Equation 2.35).
3. Compute the two-point angular cross-correlation function between the unique common lens sample and each source subsample for each band.

Once the two-point angular correlation function has been measured, it can be compared with theoretical predictions as described in chapter 2 allowing the desired parameter constraints.

As has been stated previously, the amplitude of the measured cross-correlation function depends on the shape of the galaxy number count distribution. Nevertheless, due to this shape –for a fixed footprint, population of galaxies and redshift distribution–, the brighter is the magnitude limit of the sample, the bigger is the amplitude of the two point angular cross correlation function. However, the number of bright galaxies is lower than the number of faint galaxies [138], so shot noise is bigger at brighter magnitude cuts, increasing their measurement uncertainties. For this reason, there exists a magnitude cut that is a trade-off between amplitude and shot noise, maximizing the signal-to-noise ratio. In order to find the optimum magnitude cut for a given sample, define the signal-to-noise ratio for a given angular range and magnitude cut $m' < m$ as [139]:

$$\frac{S}{N}(m) = \frac{\langle \omega_{LS}(\theta; m) \rangle}{\langle s(\omega_{LS}(\theta; m)) \rangle}, \tag{4.2}$$

where $\langle s(\omega_{LS}(\theta; m)) \rangle$ is the average shot noise of the two point angular cross correlation functions and the averages are extended to the angular range considered in the analysis. The shot noise for a given angular aperture is given by the number of pairs inside each angular bin as

$$\sigma(\omega_{LS}(\theta; m)) = \frac{1}{\sqrt{P_{LS}(\theta; m)}}, \tag{4.3}$$

where $P_{LS}(\theta; m)$ is the number of pairs from the lens-source samples separated by an angular distance θ for a magnitude cut $m' < m$. The number of pairs per angular bin is given by the product of the number of source galaxies that fall inside a given annulus times the number of sources inside that annulus. Considering, as a first order approach, that the samples are uniform, the number of lens-source pair-counts of galaxies for a bin centerd at θ with solid angle Δ_Ω is given by

$$P_{LS}(\theta; m) = \left[\frac{N_L}{A}\Delta_\Omega(\theta)\right]\left[\frac{N_S(m)}{A}\Delta_\Omega(\theta)\right]. \tag{4.4}$$

Here A is the solid angle subtended by the dataset, N_L is the number of objects at the lens sample and $N_S(m)$ the number of objects on the source sample with magnitude limit m. Combining Equations **??**, 4.2 and 4.4, results finally in

$$\frac{S}{N}(m) = \langle\omega_0\rangle[\alpha(m) - 1]b_L\frac{\Omega}{A}\sqrt{N_L N_S(m)}, \tag{4.5}$$

where Ω is the solid angle subtended by an annulus with edges the maximum and minimum scales considered. Thus, for a sample, given size, magnitude and redshift distributions –assuming a cosmology– the signal-to-noise ratio can be estimated. Nevertheless, Equation 4.5 assumes that the angular bins are uncorrelated and should be taken as an upper bound to the signal-to-noise. Although this expression does not take into account the full covariance, the behavior

$$\frac{S}{N} \sim [\alpha(m) - 1]\sqrt{N_S(m)}, \tag{4.6}$$

is independent of cosmological and covariance assumptions up to a constant factor, allowing us to use this expression for finding the optimal cut that maximizes the signal-to-noise ratio.

Equation 4.6 finds the magnitude cut with the maximum signal-to-noise for a given source sample. Nevertheless, this requires the use of less data than the *optimal weighting* approach, reaching a lower significance since less information is used. To overcome this, all the magnitude cuts –not just the maximum– are used, tracing the number-count slope evolution.

4.2 Magnification in the MICE-GC simulation

In order to test the methodology described above in a controlled environment, isolated from any source of systematic error, it is applied to a simulated galaxy sample, in particular MICECAT v1.0. This mock is the first catalog release of the N-body simulation MICE-GC[1] [140–142]. It assumes a flat ΛCDM Universe with cosmological parameters $\Omega_M = 0.25, \Omega_b = 0.044, h = 0.7$ and $\sigma_8 = 0.8$, using a light-cone that spans one eighth of the celestial sphere. Another advantage of using these simulations is the possibility of studying specific systematic effects, as described in subsection 4.3.3.

Among other properties, MICE-GC provides lensed and unlensed coordinates, true redshift (including redshift space distortions) and DES-*griz* unlensed magnitudes for the simulated galaxies, along with convergence and shear. Conversion from unlensed magnitudes to lensed magnitudes can be done by applying $m_\mu = m_0 - 2.5\log_{10}(1 + 2\kappa)$.

[1] www.ice.cat/mice

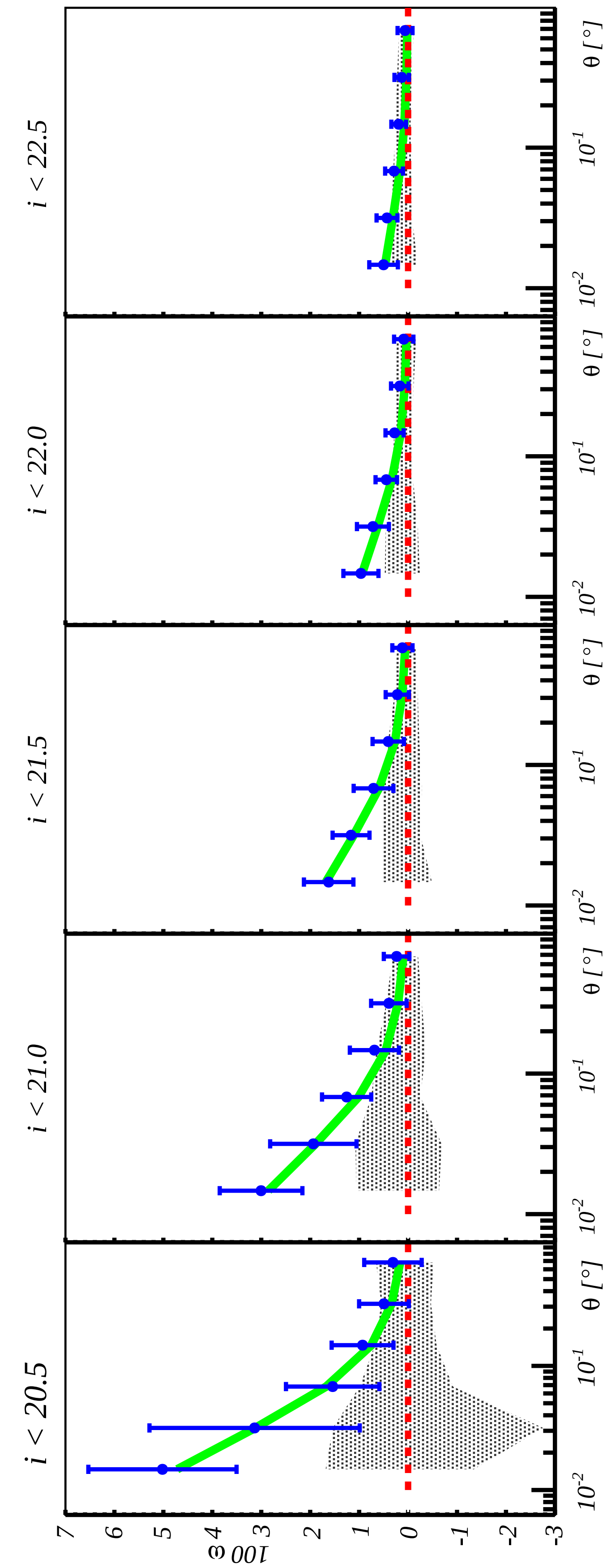

Figure 4.1: Two-point angular cross-correlation functions for the MICE simulation (sample $i < 21.5$): measured, both with magnification (blue dots) and without (grey shade), versus that expected from the MICE cosmological parameters, both with magnification (green solid line) and without (red dashed line), the latter being zero.

Having two sets of coordinates and magnitudes, one in a 'universe' with magnification and another without magnification, allows us to follow the methodology described in section 4.1 for both cases, serving as a test-bench to measure the sensitivity of the method to the magnification effect. In order to have a fiducial function with as little statistical uncertainty as possible, the full 5000 deg^2 of the MICE simulation are used. To match as much as possible the conditions of the DES-SV data, the magnitude cuts described in subsection 4.3.1 are applied to the lens and source samples. The covariance matrices of data (see section 4.3) are used, in order to match the errors in the DES-SV sample.

In Figure 4.1, the results of the magnification analysis in the MICE simulation for the cases with and without magnification can be seen compared with the theoretical expectations. The methodology used in this work clearly allows us to distinguish both cases for a data-set similar to that of the DES-SV data. Nevertheless, results obtained with the MICE simulation can not be directly extrapolated to SV data to estimate the expected significance because the density of galaxies on the simulation is a factor ~ 3 smaller than on the SV data. Also, the luminosity function of the simulation is slightly different from the DES data, which has a direct impact on the number count slope and, consequently, on the amplitude of the measured signal.

4.3 Magnification in DES Science Verification data

As of January 2014 –when I started my PhD–, the only data available at DES was the Science Verification data. The first data-release from DES. This data were taken just for testing purposes and in order to explore the capabilities of the experiment. Thus, although the nominal depth of the survey was reached, only ~ 150 deg^2 where taken. Taking this into account, only 10^4 LBGs are expected at the full DES-SV data, preventing the measurement of magnification.

In order to be capable to reach a detection of the magnification signal with the DES-SV data, the general population of galaxies was selected both as lens and source sample. This leads to technical difficulties, since DES has a low precision on the redshift determination and the general population of galaxies is mainly located at low redshift, complicating the possibility to reach a clean redshift separation.

4.3.1 Data sample

The sample used in this analysis corresponds to the Science Verification (DES-SV) data, which contains several disconnected fields. From the DES SVA1-Gold[2] main galaxy catalog [143], the largest contiguous field is selected, the SPT-E. Regions with declination $< -61°$ are removed in order to avoid the Large Magellanic Cloud. MODEST_CLASS is employed as star-galaxy classifier [144].

The following color cuts are made in order to remove outliers in color space:

- $-1 < g - r < 3$,
- $-1 < r - i < 2$,

[2] des.ncsa.illinois.edu/releases/SVA1

- $-1 < i - z < 2$;

where g, r, i, z stand for the corresponding MAG_AUTO magnitude measured by SExtractor [145].

Regions of the sky that are tagged as bad, amounting to four per cent of the total area, are removed. An area of radius 2 arcminutes around each 2MASS star is masked to avoid stellar halos [133, 146].

The DES Data Management [147–149] produces a MANGLE[3] [150] magnitude limit mask that is later translated to a $N_{\rm side} = 4096$ HEALPix[4] [151] mask. Since the HEALPix mask is a division of the celestial sphere with romboid-like shaped pixels with the same area, to avoid boundary effects due to the possible mismatch between the MANGLE and HEALPix masks, each pixel is required to be totally inside the observed footprint as determined by MANGLE, by demanding

- $r_{\rm fracdet} = 1$,
- $i_{\rm fracdet} = 1$,
- $z_{\rm fracdet} = 1$;

where $r_{\rm fracdet}, i_{\rm fracdet}, z_{\rm fracdet}$ is the fraction of the pixel lying inside the footprint for r, i, z bands respectively.

Depth cuts are also imposed on the *riz*-bands in order to have uniform depth when combined with the magnitude cuts. These depth cuts are reached by including only the regions that meet the following conditions:

- $r_{\rm lim} > 23.0$,
- $i_{\rm lim} > 22.5$,
- $z_{\rm lim} > 22.0$;

where $r_{\rm lim}, i_{\rm lim}, z_{\rm lim}$ stand for the magnitude limit in the corresponding band, that is, the faintest magnitude at which the flux of a galaxy is detected at 10σ significance level. The resulting footprint, as shown in Figure 4.2, after all the masking cuts amounts to 121 deg^2.

Photometric redshifts (photo-z) have been estimated using different techniques. In particular, the fiducial code used in this work employs a machine-learning algorithm (random forests) as implemented by TPZ [152], which was shown to perform well on SV data [153]. The redshifts of the galaxies are defined according to the mean of the probability density functions given by TPZ ($z_{\rm ph}$). Other methods are also employed to demonstrate that the measured two-point angular cross-correlation are not a feature induced by TPZ.

Lens sample

A unique lens sample is defined by the additional photo-z and magnitude cuts:

- $0.2 < z_{\rm ph} < 0.4$;
- $18.0 < i < 22.5$.

---

[3] http://space.mit.edu/∼molly/mangle/

[4] healpix.jpl.nasa.gov

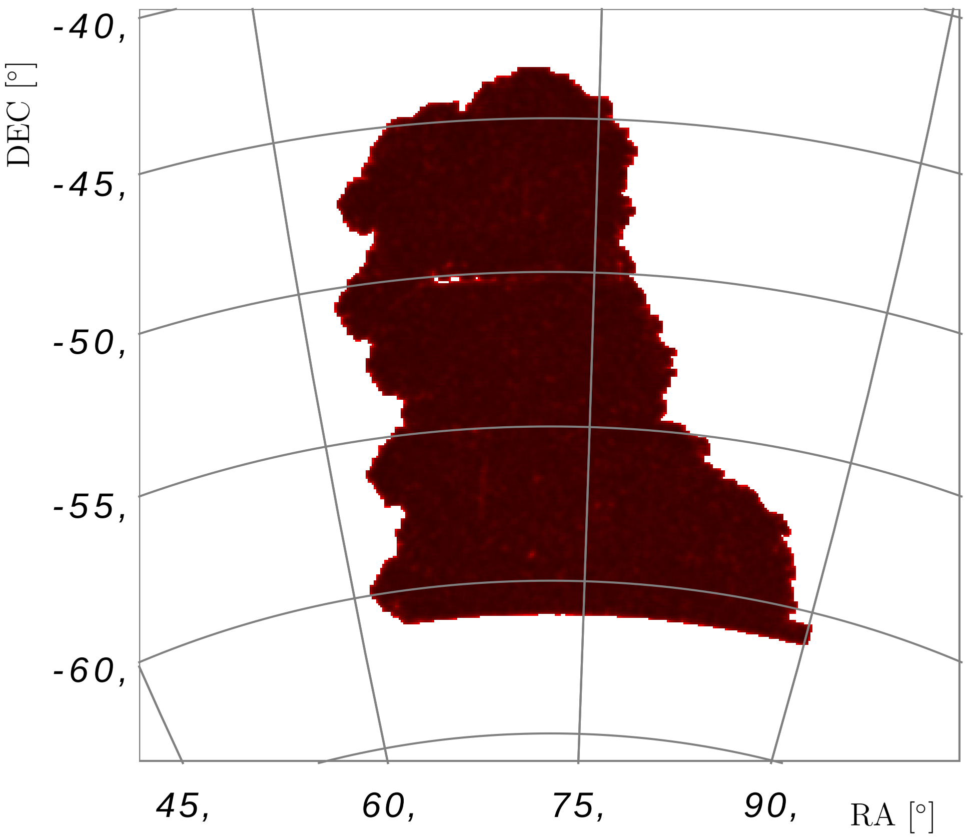

Figure 4.2: Final footprint of the DES SPT-E region after all masking is applied.

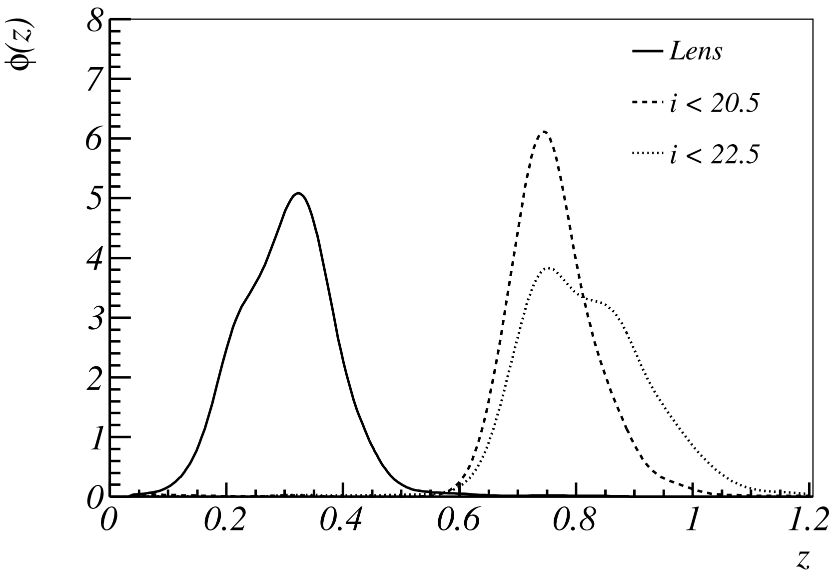

Figure 4.3: Redshift distributions from the stacking of the TPZ probability distribution functions for the lens and two i-band sub-samples of the source.

These requirements are imposed in order to be compatible with the first redshift bin of the so called 'benchmark sample' [143]. Note that the MAG_AUTO cut along with the previous i-band depth cut guarantees uniformity [143].

Source sample

Three source samples are defined, one per band:

- R: $0.7 < z_{\rm ph} < 1.0$ and $r < 23.0$;
- I: $0.7 < z_{\rm ph} < 1.0$ and $i < 22.5$;
- Z: $0.7 < z_{\rm ph} < 1.0$ and $z < 22.0$.

Following the same approach we used on the lens, defined over the 'benchmark' sample, the MAG_AUTO cut along with the previously defined depth cuts also guarantee uniformity on the corresponding band. Within each R, I, Z source sample five sub-samples that map the magnitude evolution are defined,

- R_1: $r < 21.0$; R_2: $r < 21.5$; R_3: $r < 22.0$; R_4: $r < 22.5$; R_5: $r < 23.0$.
- I_1: $i < 20.5$; I_2: $i < 21.0$; I_3: $i < 21.5$; I_4: $i < 22.0$; I_5: $i < 22.5$.
- Z_1: $z < 20.0$; Z_2: $z < 20.5$; Z_3: $z < 21.0$; Z_4: $z < 21.5$; Z_5: $z < 22.0$.

Here $\mathrm{S_j}$ with $\mathrm{j} = 1, 2, 3, 4, 5$ are the sub-samples of sample S with $\mathrm{S} \in \{\mathrm{R}, \mathrm{I}, \mathrm{Z}\}$. In Figure 4.3, the redshift distributions of the lens and source sample are shown. Note that the sub-samples $\mathrm{R}_5, \mathrm{I}_5, \mathrm{Z}_5$ are equal to $\mathrm{R}, \mathrm{I}, \mathrm{Z}$ respectively.

The g-band is not used on this analysis because when the same approach is followed and a uniform sample is defined in that band, the number of galaxies of the lens and source samples decrease dramatically. This increases the shot noise preventing the measurement of number count magnification

4.3.2 Detection of the weak-lensing magnification signal

To estimate the cross-correlation functions, the tree-code TreeCorr[5] [154] and the Landy-Szalay estimator [155] are used demanding six logarithmic angular bins:

$$\omega_{\mathrm{LS_j}}(\theta) = \frac{D_{\mathrm{L}} D_{\mathrm{S_j}}(\theta) - D_{\mathrm{L}} R_{\mathrm{S_j}}(\theta) - D_{\mathrm{S_j}} R_{\mathrm{L}}(\theta)}{R_{\mathrm{L}} R_{\mathrm{S_j}}(\theta)} + 1, \tag{4.7}$$

where $D_{\mathrm{L}} D_{\mathrm{S_j}}(\theta)$ is the number of pairs from the lens data sample L and the source data sub-sample $\mathrm{S_j}$ separated by an angular distance θ and $D_{\mathrm{L}} R_{\mathrm{S_j}}(\theta)$, $D_{\mathrm{S_j}} R_{\mathrm{L}}(\theta)$, $R_{\mathrm{L}} R_{\mathrm{S_j}}(\theta)$ are the corresponding values for the lens-random, source-random and random-random combinations normalized by the total number of objects on each sample.

Catalogs produced with Balrog[6] [156] are used as random samples. The Balrog catalogs are DES-like catalogs, where no intrinsic magnification signal has been included. The Balrog software generates images of fake objects, all with zero convergence κ, that are embedded into the DES-SV coadd images (convolving the objects with the measured point spread function, and applying the measured photometric calibration). Then SExtractor was run on them, using the same DES Data Management configuration parameters used for the image processing.

[5] github.com/rmjarvis/TreeCorr
[6] github.com/emhuff/Balrog

The positions for the simulated objects were generated randomly over the celestial sphere, meaning that these positions are intrinsically unclustered. Hence, the detected Balrog objects amount to a set of random points, which sample the survey detection probability. For a full description and an application to the same measurement as in [143] see [156]. This is the first time that this extensive simulation is used to correct for systematics. The same cuts and masking of the data sample (subsection 4.3.1) are also applied to the the Balrog sample. A re-weighting following a nearest-neighbours approach was applied to Balrog objects in order to follow the same magnitude distribution of the DES-SV data on both lens and sources.

A covariance matrix is computed for each band by jack-knife re-sampling the data taking into account the correlations between the different magnitude cut within each band

$$C_{\mathrm{S}}(\omega_{\mathrm{LS_i}}(\theta_\eta);\omega_{\mathrm{LS_j}}(\theta_\nu)) = \frac{N_{\mathrm{JK}}}{N_{\mathrm{JK}}-1} \times \sum_{k}^{N_{\mathrm{JK}}} [\omega^k_{\mathrm{LS_i}}(\theta_\eta) - \omega_{\mathrm{LS_i}}(\theta_\eta)][\omega^k_{\mathrm{LS_j}}(\theta_\nu) - \omega_{\mathrm{LS_j}}(\theta_\nu)], \tag{4.8}$$

where $\omega^k_{\mathrm{LS_j}}$ stands for the cross-correlation of the k-th jack-knife re-sample and $\omega_{\mathrm{LS_j}}$ is the cross-correlation of the full sample. The $N_{\mathrm{JK}} = 120$ jack-knife regions are defined by a k-means algorithm [157] using Python's machine learning library scikit-learn[7] [158]. In order to get N_{JK} regions with equal area, the algorithm is trained on a uniform random sample following the footprint of the data demanding N_{JK} centers. The regions used on the re-sampling are composed by the Voronoi tessellation defined by these centers. These matrices trace the angular covariance as well as the covariances between functions within each band. No covariance between bands is considered, since each band is treated independently on this work. The reduced covariance matrix of the i-band is displayed at Figure 4.4. The behaviour is similar for the other bands.

Measured two-point angular cross-correlation functions and ΛCDM weak lensing theoretical predictions can be found in Figure 4.3.2, Figure 4.3.2 and Figure 4.3.2. Measured correlation functions are found to be non-zero, compatible with ΛCDM and its amplitude evolves with the magnitude cut. The magnitude cuts imposed to guarantee uniform depth make that, for this data, no negative amplitudes are expected.

To compare with the expected theory, **??** has been used assuming Planck 2015 [159] cosmological parameters. The bias of the lens sample has already been measured independently with different techniques: clustering [143], gg-lensing [114], shear [160] and CMB-lensing [116]. From these values the most precise, from [143], is selected ($b_{\mathrm{L}} = 1.07 \pm 0.08$) and is assumed to be a constant scale-independent parameter. The number count slope parameter α_{S} is computed by fitting the

[7] scikit-learn.org

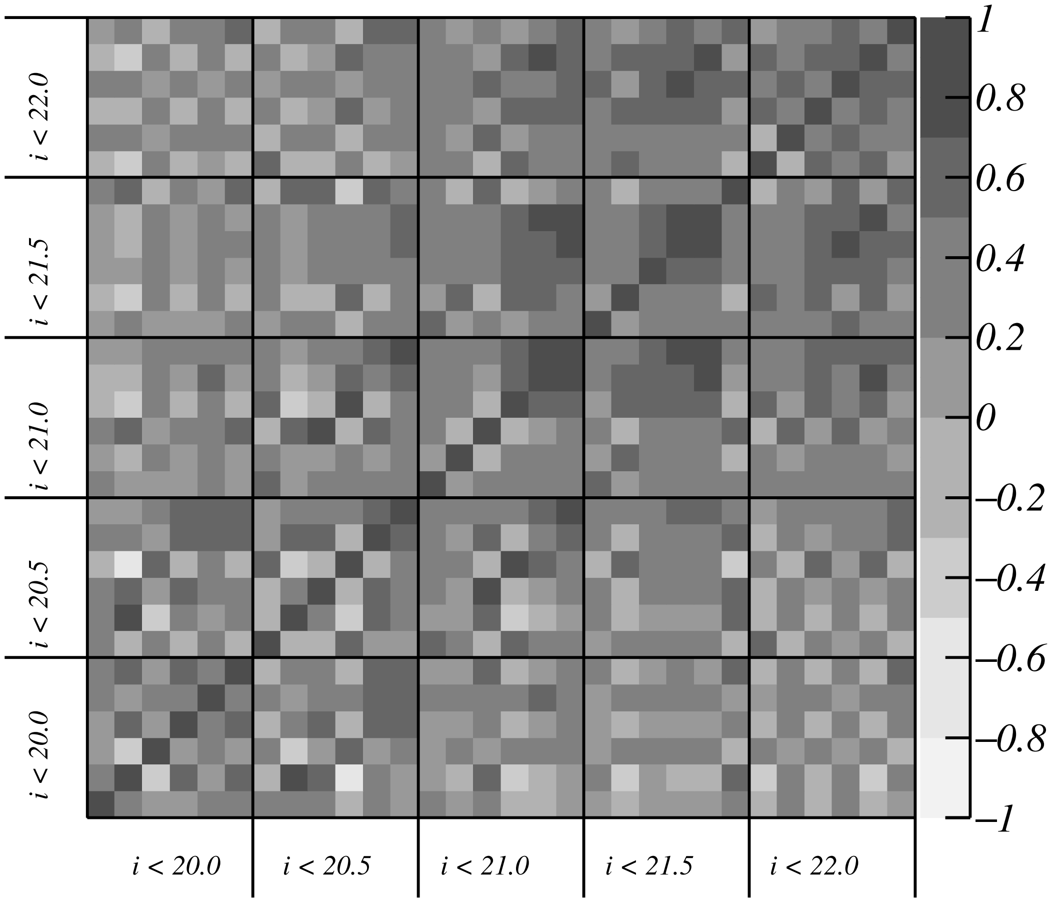

Figure 4.4: Covariance matrix of the i-band rescaled by the value of the diagonal ($C_{ij}/\sqrt{C_{ii}C_{jj}}$). Each box is the part of the matrix corresponding to the samples labeled at the axis whereas the bins within each box stand for the angular values of the correlation function.

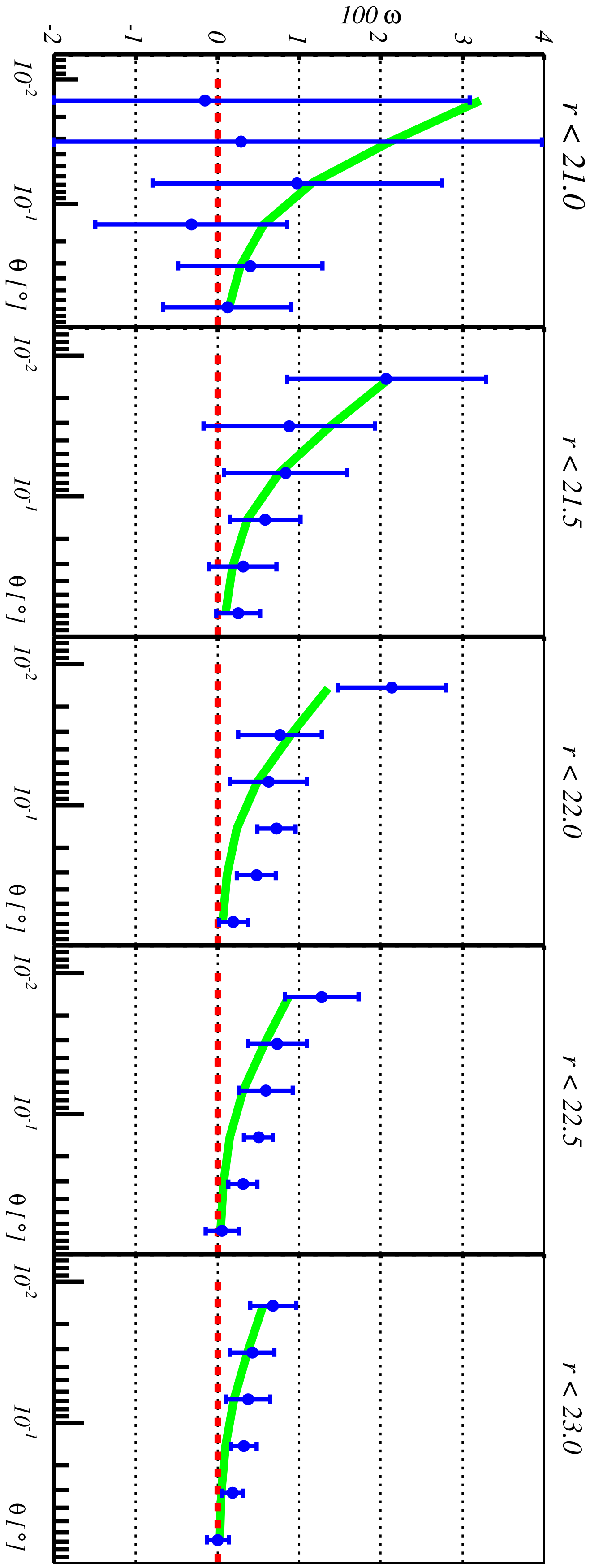

Figure 4.5: Magnification signal for the DES-SV r-band sample.

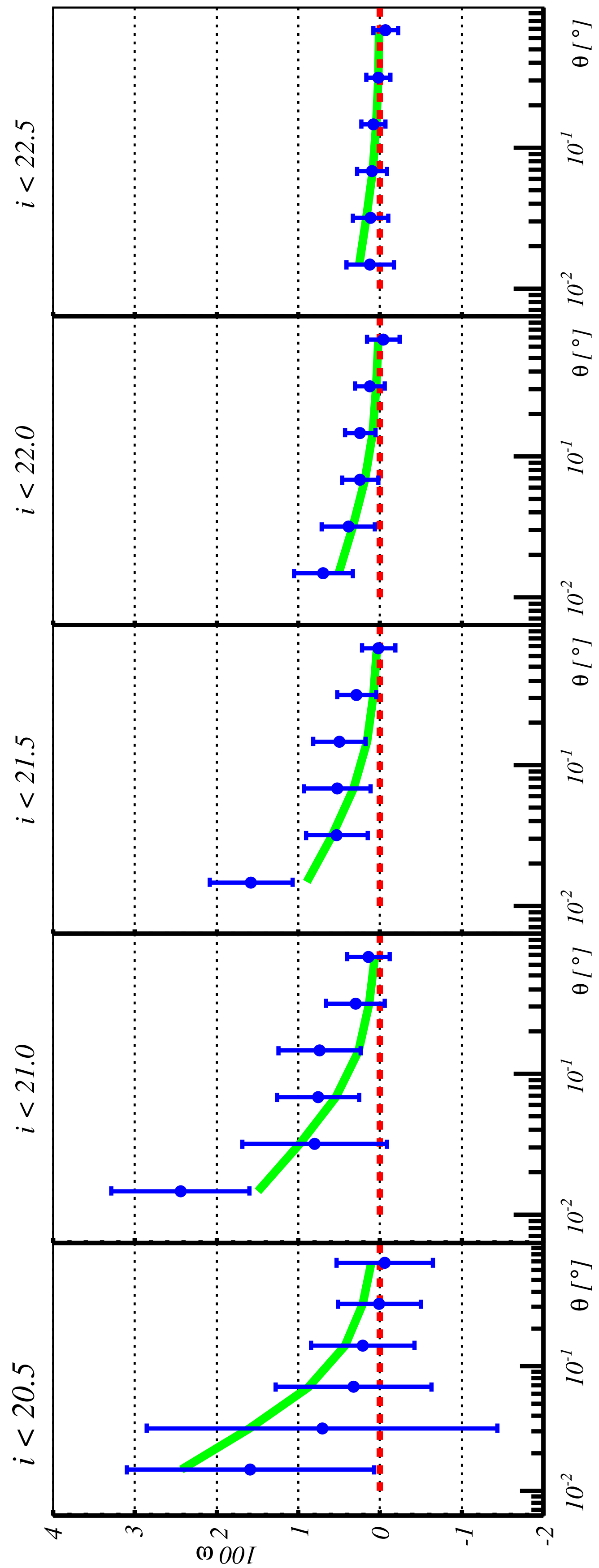

Figure 4.6: Magnification signal for the DES-SV i-band sample.

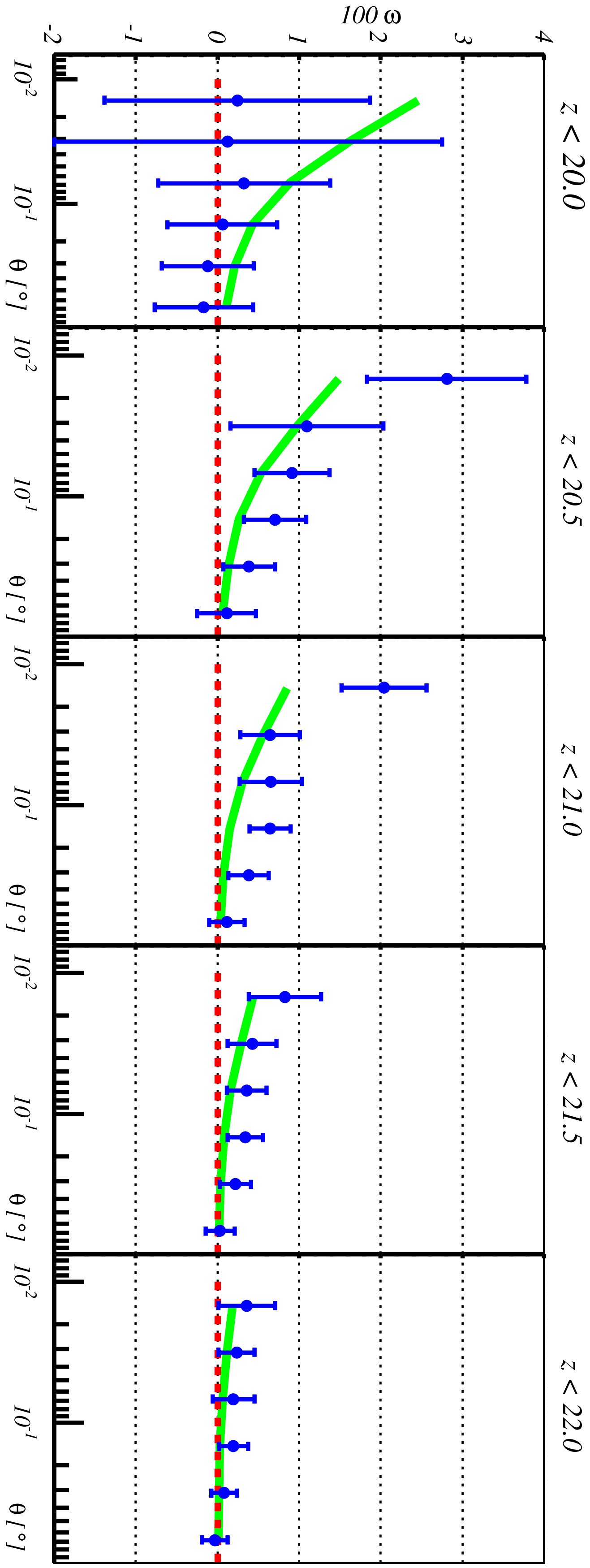

Figure 4.7: Magnification signal for the DES-SV z-band sample.

Weight	Sample	$\log_{10}\mathcal{B}$	$\chi^2/ndof$
No	R	3.9	21.6/30
	I	3.4	23.9/30
	Z	3.4	36.8/30
Yes	$r < 23.0$	3.2	3.2/6
	$i < 22.5$	2.1	2.1/6
	$z < 22.0$	2.3	2.3/6

Table 4.1: Significance of the detection of a magnification signal. Results are shown for the combination of the five subsamples within each band as well as for the faintest sample with weighting.

cumulative number count of the sample S to a Schechter function [138] on the range of interest

$$N_\mu(m) = A\left[10^{0.4(m-m_*)}\right]^\beta \times \exp\left[-10^{0.4(m-m*)}\right], \tag{4.9}$$

where A, m_*, β are the free parameters of the fit. Then $\alpha_{\mathrm{S}}(m) - 1$ is computed by applying Equation 2.35, where m_{j} is the magnitude limit of the $\mathrm{S_j}$ sub-sample on the considered band. In Figure 4.8 the fit and the number count slope parameter for the I sample are shown.

A goodness of fit test of the measured two-point angular cross-correlation function respect to the theoretical predictions for each band is performed:

$$\chi^2_{\mathrm{Planck}} = \sum_{\eta\nu ij}[\tilde{\omega}_{\mathrm{LS_i}}(\theta_\eta) - \omega_{\mathrm{LS_i}}(\theta_\eta)] \tag{4.10}$$

$$C^{-1}(\omega_{\mathrm{LS_i}}(\theta_\eta); \omega_{\mathrm{LS_j}}(\theta_\nu))[\tilde{\omega}_{\mathrm{LS_j}}(\theta_\nu) - \omega_{\mathrm{LS_j}}(\theta_\nu)], \tag{4.11}$$

where $\tilde{\omega}, \omega$ are the measured and theoretical cross-correlation functions respectively. Goodness of fit tests are also made testing the hypothesis of absence of magnification:

$$\chi^2_{\mathrm{zero}} = \tag{4.12}$$

$$\sum_{\eta\nu ij}\tilde{\omega}_{\mathrm{LS_i}}(\theta_\eta) C^{-1}(\omega_{\mathrm{LS_i}}(\theta_\eta); \omega_{\mathrm{LS_j}}(\theta_\nu))\tilde{\omega}_{\mathrm{LS_j}}(\theta_\nu).$$

The χ^2 values can be seen in Table 4.1 showing good agreement with the theoretical predictions described in chapter 2. To test which hypothesis is favored, the Bayes factor is used:

$$\mathcal{B} = \frac{P(M|\Theta)}{P(Z|\Theta)} = \frac{P(\Theta|M)}{P(\Theta|Z)}\frac{P(M)}{P(Z)}, \tag{4.13}$$

where

$$P(M|\Theta) = e^{-\chi^2_{\mathrm{Planck}}/2} \tag{4.14}$$

and

$$P(Z|\Theta) = e^{-\chi^2_{\mathrm{zero}}/2}. \tag{4.15}$$

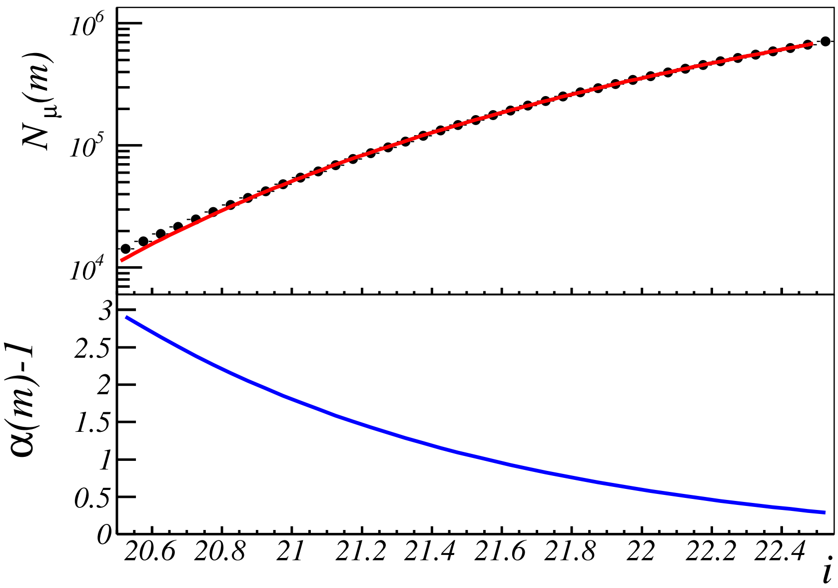

Figure 4.8: Top panel: Dots are the measured i-band cumulative number count as a function of the i-band magnitude. Red solid line is the fit using a Schechter function (see text). Bottom panel: number count slope $\alpha - 1$ measured from the fitted Schechter function of the top panel.

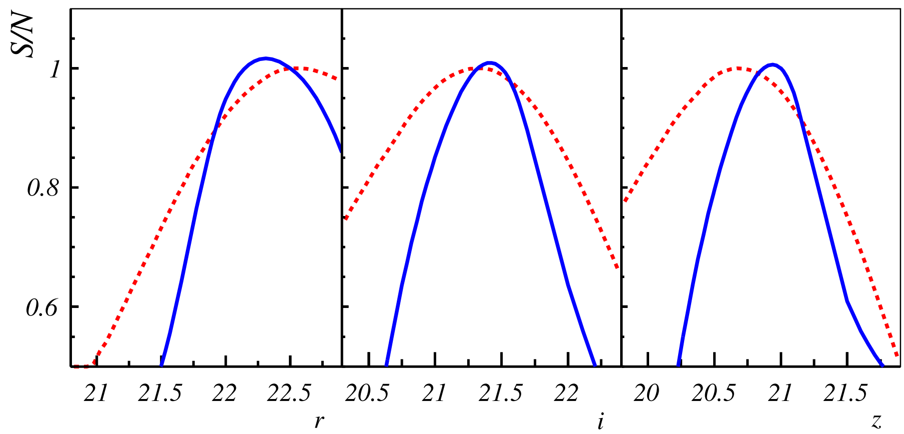

Figure 4.9: Red dashed line: expected signal-to-noise ratio computed with Equation 4.2. Blue solid line is the measured significance of the data. Both curves are normalized to their respective maximum.

The assumed prior sets detection and non-detection of magnification to be equally probable: $P(M) = P(Z)$. Bayes factors are computed for each function individually as well as for each band using the full covariance.

The significance for each individual correlation function has a strong dependence on the considered magnitude limit of the sub-sample. At the bright cuts, shot-noise prevents the identification of a non-zero magnification signal. At the faint end, although the sub-samples are much more populated, the strength of the magnification signal is compatible with zero. This behaviour has been compared with the predictions (see section 4.1). Predicted and measured values are plotted together in Figure 4.9. It can be seen that the prediction of the location of the maximum signal-to-noise can only be used as a first approach.

To compute the significance of the detection for each band, the full covariance is used. One covariance matrix (see Figure 4.4 for the i-band matrix) per each band is computed taking into account the correlations between each magnitude cut. The logarithm of the Bayes factor can be found in Table 4.1, being all above 2, allowing to claim that magnification has been detected [161].

A usual approach to enhance the signal-to-noise ratio, is to define a unique source sample and weight each source galaxy with its corresponding $\alpha_S(m) - 1$ value [98] and compute the two-point angular cross-correlation function. This weighting procedure is used at the samples $r < 23.0$, $i < 22.5$ and $z < 22.0$. These correlation functions can be seen in Figure 4.10 with a comparison with the theoretical prediction and the correlation functions of the same sample computed without weighting. Significances of these measurement can be found in Table 4.1 with a marginal difference respect to the one computed without weighting using the five subsamples.

Finally, in order to test that the signal is achromatic, the measured two-point angular cross-correlation functions for each band, normalized by its $\alpha_S(m) - 1$ are compared. All cross-correlation functions fluctuate within 1σ errors (see Figure 4.11 for an example) demonstrating that the measured convergence field does not depend on the considered band.

4.3.3 Systematic error analysis

Here, the impact of potential sources of systematic errors on the measured two-point angular cross-correlation function is investigated and how they are taken into account in the measurement is described.

Number count slope α

When comparing the measured two point angular cross-correlation functions with the theoretical prediction via **??** for a given set of cosmological parameters, $\alpha(m)$ is determined by fitting the cumulative number count distribution to Equation 4.9 and then using Equation 2.35. To compute the possible impact of the uncertainty of this fit on the comparison with theory, a marginalisation over all the parameters

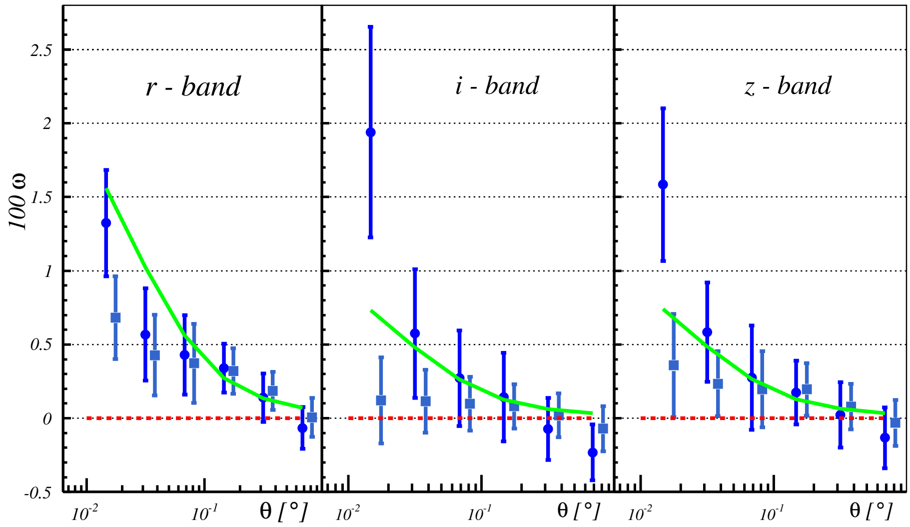

Figure 4.10: Measured two-point angular cross-correlation functions for the samples $r < 23.0$, $i < 22.5$ and $z < 22.0$ left to right respectively. Dots use the optimal weighting [133], where each galaxy is weighted by its corresponding $\alpha_S(m) - 1$ value, whereas squares are not weighted. Green line is the theoretical prediction. Red dashed line is an eye-guide for zero.

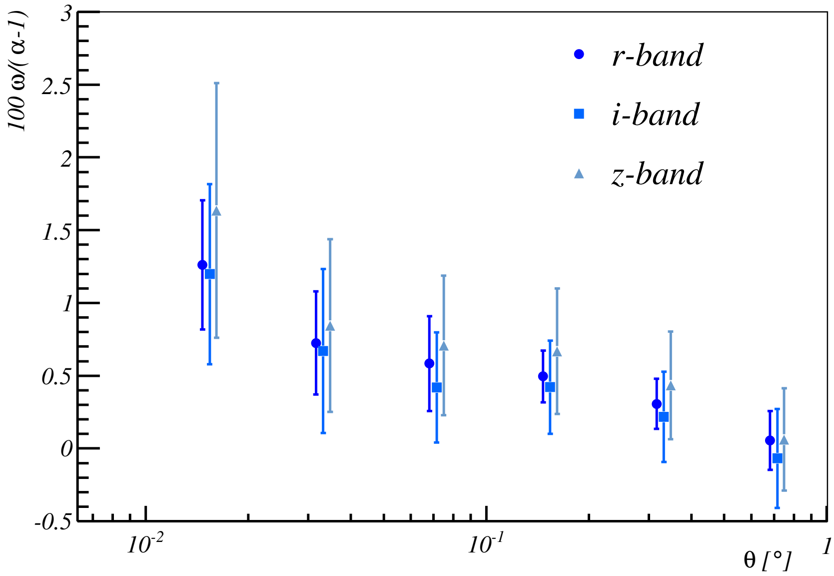

Figure 4.11: Example of the achromaticity of the measured signal. Here are shown the measured two-point angular cross-correlation functions for $r < 22.5$, $i < 22.0$ and $z < 21.5$ divided by their corresponding $\alpha - 1$.

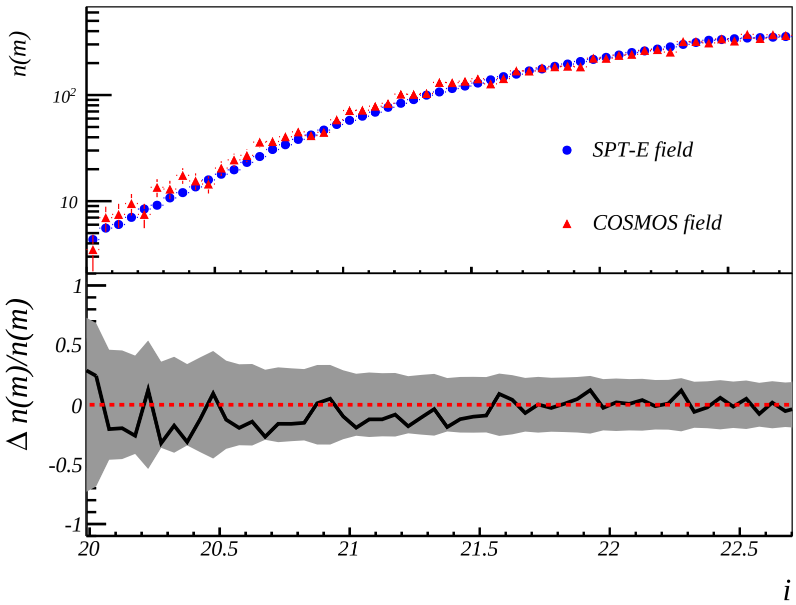

Figure 4.12: Upper panel: Comparison of the magnitude distribution for the SPT-E and the COSMOS fields. Both histograms are normalized by their respective area. Lower panel: Relative difference between the magnitude distribution of the COSMOS and the SPT-E fields. The shaded region shows the 1σ confidence interval computed from shot-noise.

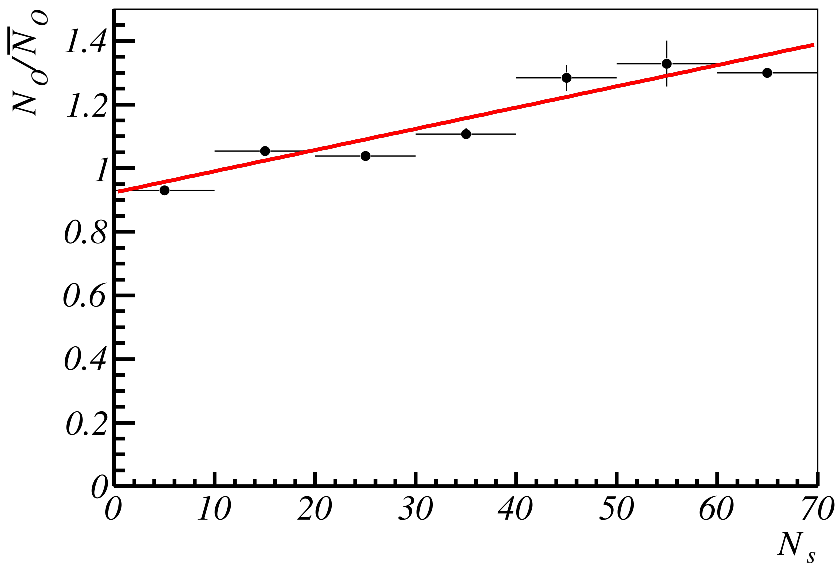

Figure 4.13: Determination of the purity of the lens sample. For each $N_{\rm nside} = 512$ HEALPix-pixel, the number of objects classified as galaxies divided by the average number of galaxies per pixel is plotted as a function of the number of objects classified as stars. Black dots are the measured data. Red line is the linear fit to the data. The intercept of the line with the Y-axis is the estimated purity of the sample.

of fit (A, m_*, β) is made.

Parameters are randomly sampled with a Gaussian distribution centerd on the value given by the fit to the cumulative number count and with a standard deviation equal to the 1σ errors of the fit. The value of α is recalculated with these randomly sampled parameters. The impact of the dispersion of the α values obtained is negligible compared to the size of the jackknife errors, so they are not taken into account.

In addition to the parameter determination, a possible non-completeness on the SPT-E field can modify the magnitude distribution altering the cumulative number count slope parameter [44]. To estimate the possible impact of non-completeness, the measured magnitude distributions of the SPT-E field are compared with those of deeper fields measured by DES, such as the COSMOS field. Both distributions are found to be equal at the range of magnitudes considered on this analysis (see Figure 4.12 for an example in the i-band).

Object obscuration

Chang [144] studied whether moderately bright objects in crowded environments produce a decrease in the detection probability of nearby fainter objects at scales $\theta \lesssim 10$ arcsec. However, such scales are well below those considered in this analysis ($\theta > 36$ arcsec) and therefore this effect is ignored.

Stellar contamination

For a given choice of star-galaxy classifier, there will be a number of stars misclassified as galaxies, so the observed two-point angular cross-correlation function $\omega_O(\theta)$ must be corrected by the presence of any fake signal induced by stars (see chapter A):

$$\omega_{\mathrm{LS_j}} = \frac{\omega_{\mathrm{O}}(\theta) - \lambda_{\mathrm{L}}\omega_{*\mathrm{S_j}}(\theta) - \lambda_{\mathrm{S_j}}\omega_{\mathrm{L}*}(\theta)}{1 - \lambda_{\mathrm{L}} - \lambda_{\mathrm{S_j}}}, \tag{4.16}$$

where $\omega_{\mathrm{LS_j}}$ is the corrected galaxy cross-correlation function, $\omega_{\mathrm{L}*}$ is the cross-correlation function of the true galaxy lenses with the stars misclassified as galaxies in the source sample, $\omega_{*\mathrm{S_j}}$ is the cross correlation of the stars misclassified as galaxies in the lenses with the true source galaxies and $\lambda_{\mathrm{L}}, \lambda_{\mathrm{S_j}}$ are the fraction of stars in the lens and in the source samples respectively. Assuming that the misclassification of stars is spatially random and is a representative sample of the spatial distribution of the population classified as stars and that the fraction of misclassified stars is small, the functions $\omega_{\mathrm{L}*}, \omega_{*\mathrm{S_j}}$ are estimated from the cross-correlation of the galaxy population and the stellar population in the corresponding redshift bin.

Following a similar approach to [162], if the latter is true and the misclassified stars trace the global population of stars, for a given patch of the sky the number of objects classified as galaxies N_{O} must be the average number of true galaxies $\bar{N}_{\mathrm{g}}$ plus a quantity proportional to the number of stars on that given pixel,

$$N_{\mathrm{O}} = \bar{N}_{\mathrm{g}} + \tilde{\gamma} N_{\mathrm{s}}. \tag{4.17}$$

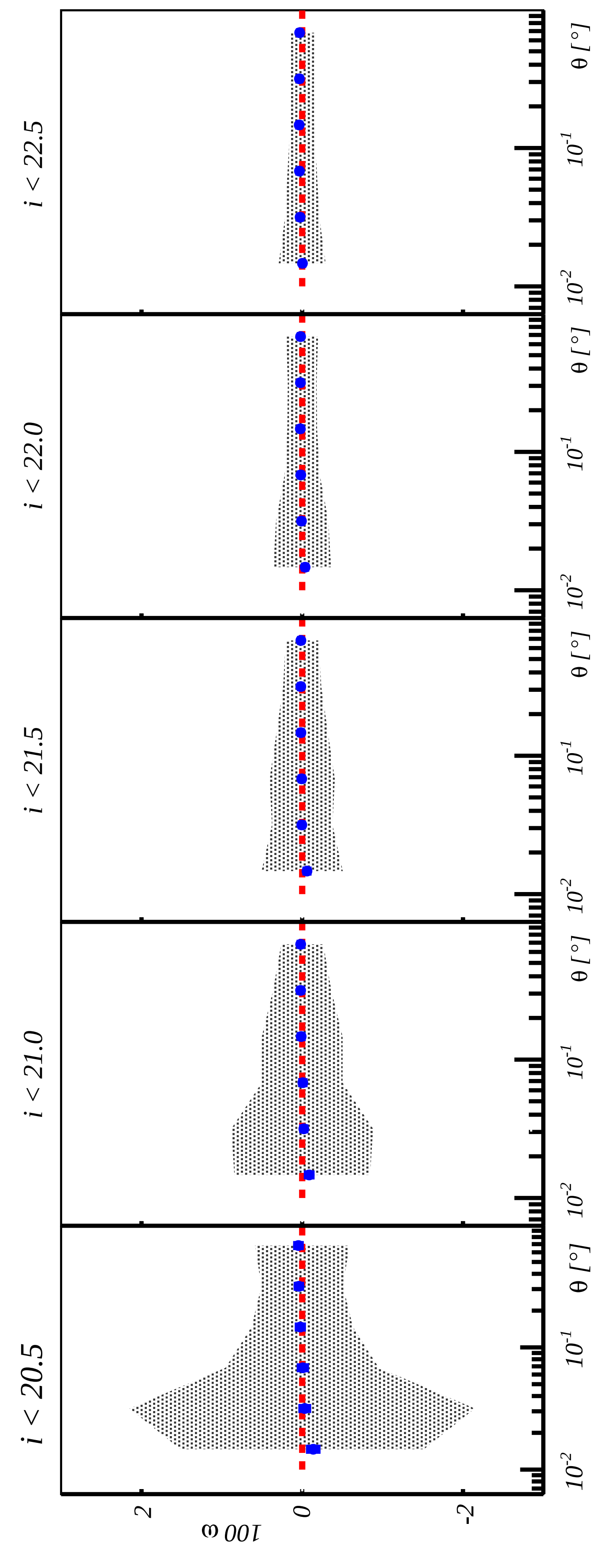

Figure 4.14: Correction by stellar contamination on the $i < 21.5$ sample. Blue dots are the correction and shaded area is the 1σ confidence interval of the measured cross-correlations of the magnification signal. Red dashed line is and eye-guide for zero.

Dividing by the average number of objects marked as galaxies $\bar{N}_{\mathrm{O}}$,

$$\frac{N_{\mathrm{O}}}{\bar{N}_{\mathrm{O}}} = p + \gamma N_{\mathrm{s}}, \tag{4.18}$$

where $p = \bar{N}_{\mathrm{g}}/\bar{N}_{\mathrm{O}}$ is the purity of the sample, that is, $\lambda = 1 - p$.

In order to estimate the purity of the galaxy sample with this method, an $N_{\mathrm{side}} = 512$ HEALPix pixelation is made and for each pixel $N_{\mathrm{O}}/\bar{N}_{\mathrm{O}}$ and N_{s} is computed. Then, a fit to Equation 4.18 is made determining a purity of 94 per cent for the lens sample and about 98 per cent for the source sample depending on the considered band (see Figure 4.13 for an example). With this purity, the correction due to stellar contamination given by Equation 4.16 is found to be one order of magnitude smaller than the statistical errors (see Figure 4.14 for the i-band correction), so stellar contamination is not taken into account in the analysis. Nevertheless, on future analysis with more galaxies and area this may be important. Note that the objects labeled as stars by our star-galaxy classifier would be a combination of stars and galaxies thus these calculations are an upper bound to stellar contamination.

Survey observing conditions

Observing conditions are not constant during the survey, leading to spatial dependencies across the DES-SV footprint [163] that may affect the observed cross-correlation function, such as seeing variations, air-mass, sky-brightness or exposure time [137]. To trace these spatial variations, the catalog produced by the Monte Carlo sampling code Balrog has been used as random sample [156]. It is important to remark that Balrog catalogs are produced with the same pipeline as DES-SV data, allowing one to trace subtle effects such as patchiness on the zero-points, deblending and possible magnitude errors due to a wrong sky subtraction close to bright objects.

The use of Monte Carlo sampling methods provides a new approach to mitigate systematic effects complementary to methods that cross-correlate the galaxy-positions with the maps of the survey observing conditions [137, 162, 164] or involve masking the regions of the sky with worst values of the observing conditions [143]. The amount of sky to be masked in order to mitigate the systematic effects on the correlation functions, is freely decided based on the impact on the correlation function, which may lead to a biassed measurement. On the other hand, the approach involving cross-correlations may lead to an overcorrection effect since the different maps of the observing conditions are, in general, correlated in a complicated manner [165]. This new Monte Carlo technique to sample the selection function of the survey given by Balrog, has the advantage that takes into account the correlation of the different observing conditions maps as well as provides an objective criteria to mitigate systematic errors on the correlation function for a given sample, avoiding biassed measurements. In addition, the use of Balrog has the potential to allow us in the future to exploit the full depth of the survey [156].

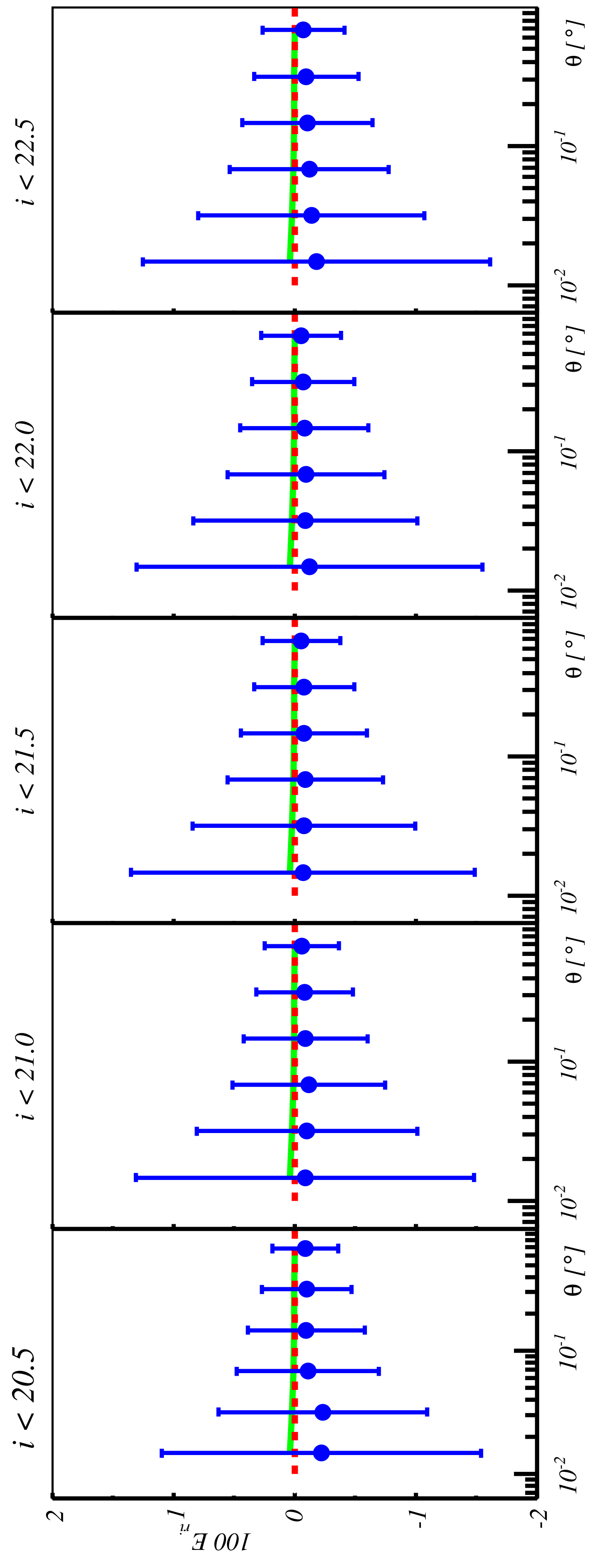

Figure 4.15: Blue dots: color-density cross-correlation functions measured on SV data for the r and i bands (sample $i < 21.5$). Green solid line is the expected value from Equation 4.22. Red dashed line is an eye-guide for zero.

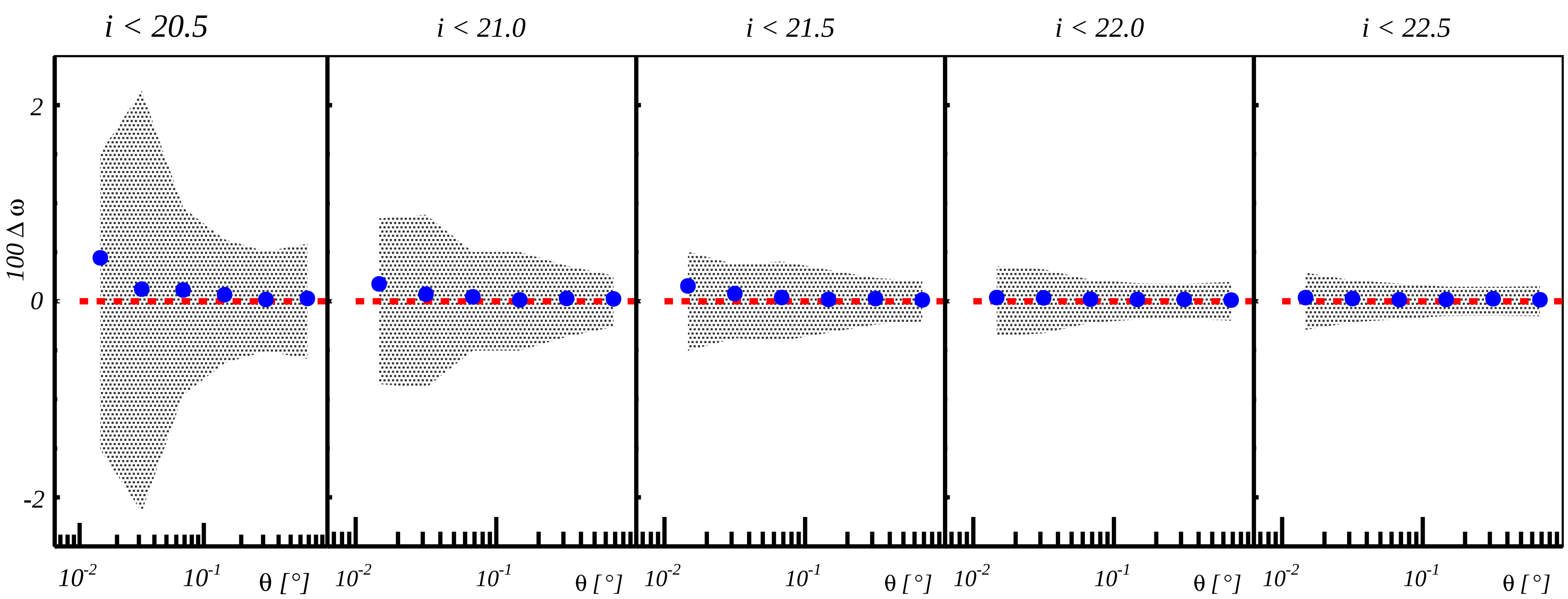

Figure 4.16: Impact of dust on the number count from MICE (sample I). Shade is the 1σ confidence interval. Blue dots are the number count differences between the case with and the case without the simulated dust profile. Red dashed line is an eye-guide for zero.

Dust extinction

The possible presence of dust in the lenses may modify the observed magnitude in addition to the magnitude shift due to magnification [135]. The change in magnitude (δm) on the p-band may be written as

$$\delta m_p = -2.5 \log \mu + \frac{2.5}{\ln 10} \tau_p, \tag{4.19}$$

where $\mu \simeq 1 + 2\kappa$ is the change in magnitude due to magnification and τ_k is the optical depth due to dust extinction. Whereas magnification is achromatic, dust extinction induces a band-dependent magnitude change. Taking this into account, the color-excess for bands p, q[8] is defined as

$$E_{pq} = \delta m_p - \delta m_q = 1.08[\tau_p - \tau_q]. \tag{4.20}$$

Define the color-density cross-correlation as [135]

$$\langle \delta_{\mathrm{g}} E_{pq} \rangle(\theta) = 1.09[\tau_p(\theta) - \tau_q(\theta)], \tag{4.21}$$

where δ_{g} is the density contrast of the lenses and E_{pq} is the color-excess of the sources; from the measurements by [135] it can be parametrized as

$$\langle \delta_{\mathrm{g}} E_{pq} \rangle(\theta) = 1.09 \tau_V \left[\frac{\lambda_V}{\lambda_p} - \frac{\lambda_V}{\lambda_q} \right] \left(\frac{\theta}{1'} \right)^{-0.8}, \tag{4.22}$$

with $\tau_V = 2.3 \times 10^{-3}$ the optical depth at the V-band and $\lambda_V, \lambda_p, \lambda_q$ the average wavelengths of the V, p and q bands respectively. With this parametrization, the impact of dust extinction is negligible at the scales considered on this analysis. As it can be seen in Figure 4.15, color-density cross-correlation functions are compatible with Equation 4.22 as well as with zero.

In addition, the impact of a dust profile has been simulated as described in Equation 4.22 with the MICE simulation (section 4.2). To do so, for each galaxy belonging to the source sample a magnitude shift is induced

$$m_d = m_\mu + 1.09 \tau_V \frac{\lambda_V}{\lambda} \sum_l \left(\frac{\theta_l}{1'} \right)^{-0.8}. \tag{4.23}$$

Here θ_l is the angular separation of the source-galaxy and the l-th lens galaxy and the summation is over all the galaxies of the lens sample. In Figure 4.16 the difference between the two-point angular cross-correlation with and without the dust can be seen to be less than the statistical errors. It can be deduced that dust has no impact on the angular scales considered on this work.

Since the parametrization used here only applies to a sample similar to the one used at [135], statements about dust constrains are limited. Nevertheless this does not change the fact that no chromatic effects are detected.

Figure 4.17: Comparison of 1σ jackknife errors of the measured correlation function (grey shade) with the expected signal induced by the photo-z migration between the lens and the source sample (sample I) computed theoretically with the stacking of the pdfs for the i-band (blue line).

Photometric redshifts

A general study of photo-z performance in DES-SV can be found in [153]. A comprehensive study of the photo-z performance and its implications for weak lensing for this data can be found in [166]. Both studies are followed in this analysis.
Conservative photo-z cuts are made in order to minimize migration between lens and source samples. Nevertheless, catastrophic outliers in the photo-z determination can bias the measurement of κ [167]. Thus, the tails of the probability density functions (pdfs) of the photo-z code are a crucial systematic to test.
As mentioned in chapter 2, in addition to the magnification signal, galaxy migration due to a wrong photo-z assignment between lens and source samples may induce a non-zero cross-correlation signal due to the physical signal coming from the clustering of objects in the same redshift bin. As a first approach, estimation of the expected signal induced by photo-z migration (ω^{ph}) is computed with Equation 2.28:

$$\omega^{\mathrm{ph}}_{\mathrm{LS_j}}(\theta) = \int\limits_0^\infty dz \int\limits_0^\infty dz' \phi_{\mathrm{L}}(z)\phi_{\mathrm{S_j}}(z')\xi(\theta; z, z'), \tag{4.24}$$

where $\xi(\theta; z, z')$ is the 3D correlation-function and $\phi_{\mathrm{L}}, \phi_{\mathrm{S_j}}$ are the redshift distribution of the lens (L) sample and the source sample ($\mathrm{S_j}$) estimated from the stacking of the pdfs given by TPZ. Figure 4.17 compares the measured two-point angular cross-correlation and the expected signal induced by photo-z can be seen for the I sample. The signal induced by photo-z is found to be smaller than the statistical errors. Note that this method relies on an assumed cosmology and bias model, and therefore should be considered only an approximation. A more accurate calculation can be made with the help of N-body simulations.

From the overlap of the redshift distribution of both lens and source samples, it is found that the total photo-z migration between lens and source sample is $o \sim 0.6\%$ depending on the magnitude cut of the source sample. The procedure to compute this overlap is to integrate the product of the pdfs of the lens and source sample:

$$o = \int\limits_0^\infty dz \phi_L(z)\phi_S(z), \tag{4.25}$$

where ϕ_L, ϕ_S are the stacked pdfs of the lens and source sample respectively. Since TPZ provides an individual pdf for each galaxy, the stacked pdf of a given sample

[8] In this section p, q stand for a generic index label while V stands for the V band of the UBV system.

is computed by adding all the individual pdfs of the galaxies that belong to that sample (see [168] for a study of clustering with stacked pdfs).

To estimate the maximum photo-z migration allowed between the lens and the source sample, the MICE simulation (section 4.2) with the un-lensed coordinates and magnitudes is used. Galaxies are randomly sampled on the lens redshift bin and then placed on the source redshift bin. Conversely, galaxies on the source redshift bin are randomly sampled and placed on the lens redshift bin. For a given lens or source sample, the number of galaxies introduced from the other redshift bin is chosen to be 0.1, 0.3, 0.5, 0.7, 0.9 and 2 per cent of the galaxies. Then, the two-point angular cross-correlation is computed for each case. The difference of the correlation functions measured at the simulation with induced migration between lens and source sample and the original used in section 4.2 is the signal induced by photo-z migration. The signal induced by photo-z for the cases with 0.9 and 2 per cent computed with this method can be seen at Figure 4.18. It is found that at 0.9 per cent of contamination, the induced signal due to photo-z migration is comparable to the error in the correlation functions. This upper limit is greater than the estimated photo-z migration, demonstrating that the effect of photo-z migration is negligible. Photo-z migration has a larger impact on the brightest samples. Nevertheless, since the errors of the correlation functions of these samples are shot-noise dominated, the tightest constrains on photo-z migration are imposed by the faintest samples. With a larger data sample this statement will no longer be true.

Photo-z induced correlation functions that mimic magnification may affect the measured significance. Thus, Bayes factor is recomputed with two new hypothesis, the measured signal is a combination of magnification and photo-z ($M + Ph$) or the measured signal is only photo-z (Ph):

$$\mathcal{B} = \frac{P(M + Ph|\Theta)}{P(Ph|\Theta)} = \frac{P(\Theta|M + Ph)}{P(\Theta|Ph)}, \tag{4.26}$$

where

$$P(\Theta|M + Ph) = e^{-\chi^2_{\mathrm{Planck+Ph}}/2} \tag{4.27}$$

and

$$P(\Theta|Ph) = e^{-\chi^2_{\mathrm{Ph}}/2}. \tag{4.28}$$

To compute $\chi^2_{\mathrm{Planck+Ph}}$ and χ^2_{Ph} it has been assumed that the expected theory is given by $\omega_{\mathrm{LS_j}}(\theta) + \omega^{\mathrm{ph}}_{\mathrm{LS_j}}(\theta)$ and $\omega^{\mathrm{ph}}_{\mathrm{LS_j}}$ respectively, where $\omega^{\mathrm{ph}}_{\mathrm{LS_j}}$ is the expected signal induced by photo-z computed using Equation 4.24. The significances recomputed using these two new hypothesis for the r, i and z bands are $\log_{10}\mathcal{B} = 2.5, 4.0, 3.5$ respectively. Thus, it can be concluded that photo-z migration has a limited impact on the measured significances.

All previous calculations were based on the assumption that the pdfs are a reliable description of the true redshift distribution. This statement can be partially validated comparing the pdfs with the spectroscopic redshift distribution for the

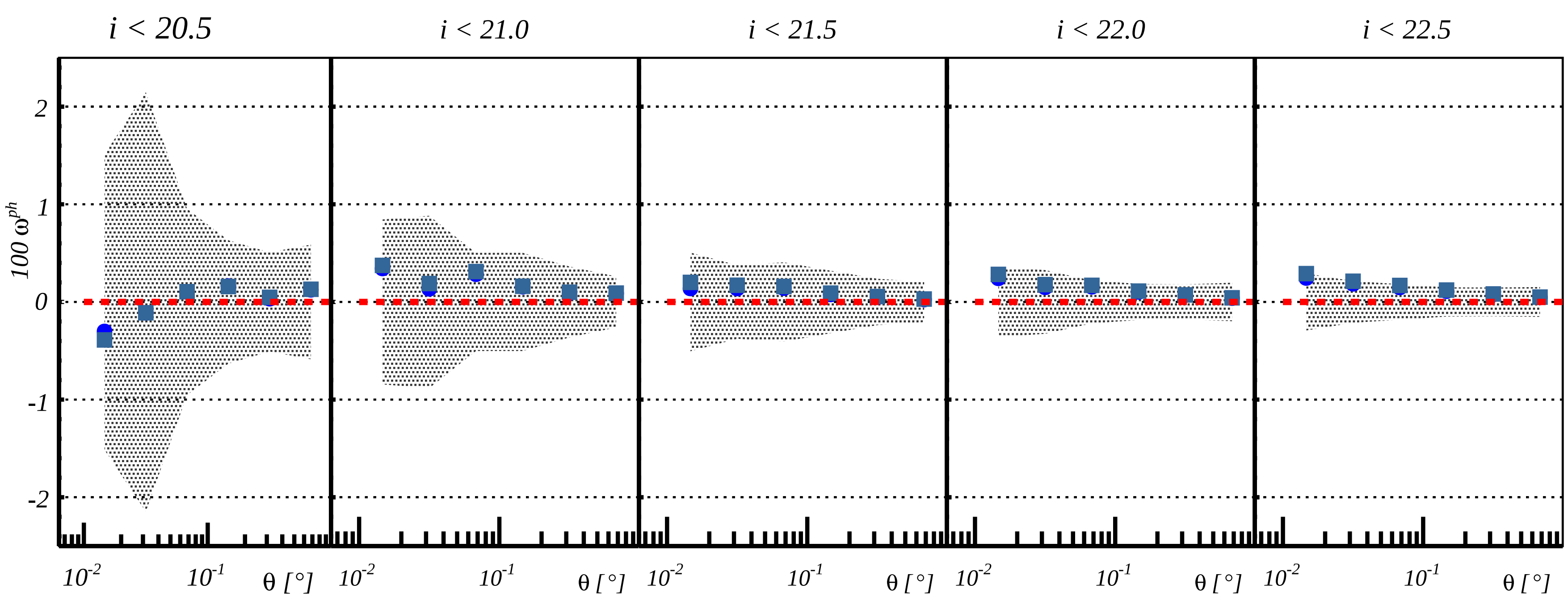

Figure 4.18: Estimation of the signal induced by migration of selected fractions of MICE un-lensed galaxies between the lens and the source sample (sample I). Shaded area is the 1σ confidence interval for the measured number count cross-correlations. Dark blue dots correspond to a contamination fraction of 0.9 per cent. Violet squares correspond to a 2 per cent. Squares are displaced at the X axis for clarity. Red dashed line is an eye-guide for zero.

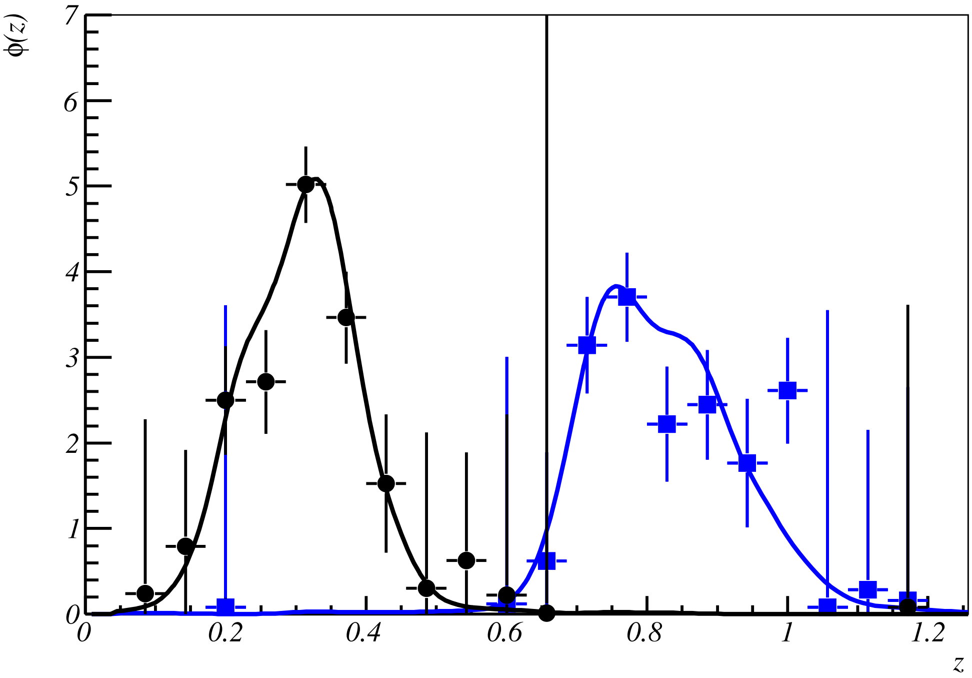

Figure 4.19: Comparison of the redshift distribution computed by the stacking of the pdfs given by TPZ (solid lines) with the ones computed with the spectroscopic sample of the lens (black dots) and the source sample $i < 22.5$ (blue squares).

same sample (see Figure 4.19 for an example). Redshift distributions predicted by TPZ are found to be representative of those given by the spectroscopic sample. Nevertheless, this statement has limitations –but is good enough for SV data– and a more accurate description of the real redshift distribution of the full sample will be measured with methodologies involving clustering-based estimators [169–172] when the size of the data sample grows. This type of estimators involve the use of two-point angular cross-correlations between different redshift bins, whose measurement may be biassed by number count magnification itself. Nevertheless, as it has been stated in chapter 2, depending on the value of the number count slope, the amplitude induced by magnification on the correlation-function may be zero. Thus, when employing this kind of estimators, samples should be carefully chosen so that $\alpha_S - 1 = 0$. This can be done by measuring the number count slope at the cumulative magnitude distribution with methods such that used in this work.

Finally, to demonstrate that the measured signal is independent of the photo-z technique employed to estimate the redshift, the two-point angular cross-correlation functions used on this analysis are re-computed with redshift estimated with other two different approaches that have shown to have similar performance as TPZ [153] a neural network, Skynet [173], and a template based approach, Bayesian Photo-Z (BPZ) [174]. Figure 4.20 compares the cross-correlations computed with the three codes for the i-band, showing them to be within 1σ errors.

4.4 Magnification in DES Year 1 data

4.4.1 Data sample

Lens sample

Lens sample

4.4.2 Determination of matter profile: voids & troughs

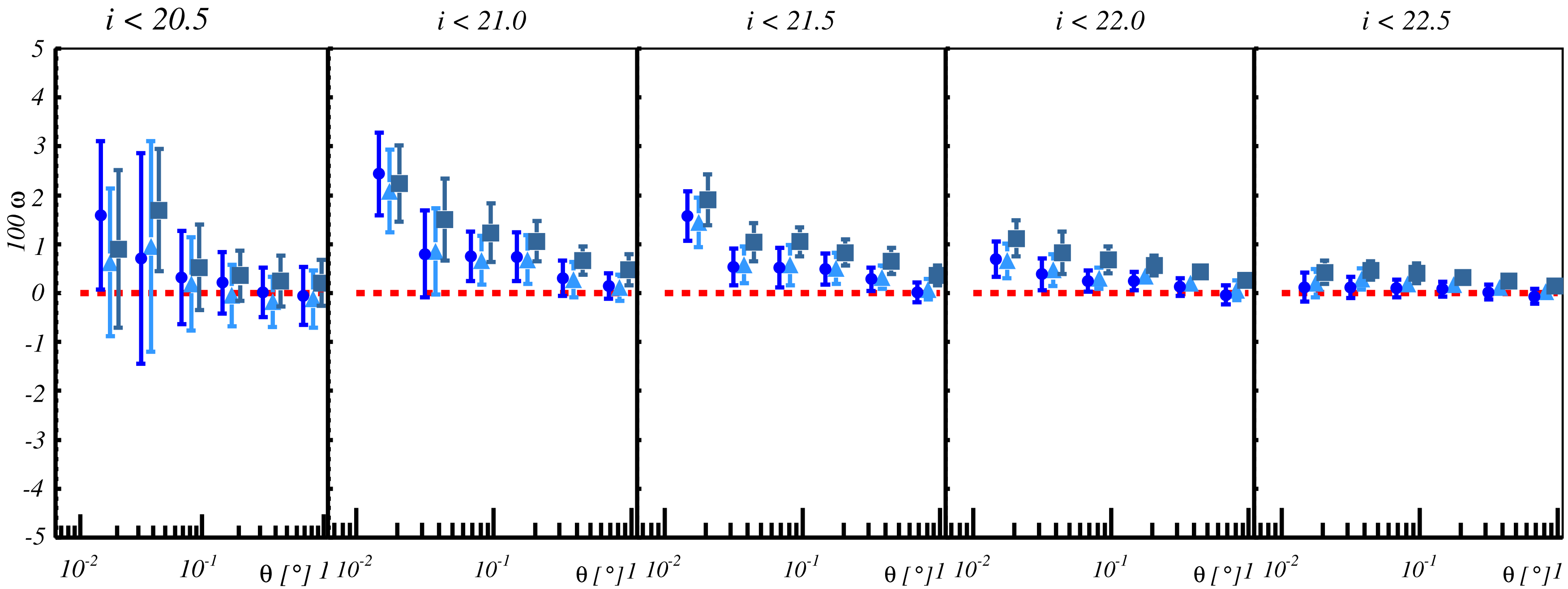

Figure 4.20: Comparison of the measured two-point angular cross-correlation functions corresponding to the sample $i < 21.5$ measured with the Landy-Szalay estimator using TPZ, Skynet and BPZ. Triangles and squares are displaced at the horizontal axis for clarity.

5. Conclusions

General Relativity has been the gravitational theory since Einstein conceived it a century ago. Since then, it passed successfully the most stringent tests. Nevertheless, the discovery of the accelerated expansion of the Universe –dark energy– along with the latest LHC results on High Energy Physics suggest that there must be something beyond General Relativity or the Standard Model of Particle Physics.

Tests of gravity on cosmological scales can provide an insight on the nature of dark energy. One of those scenarios, are the empties regions of the Universe: voids and troughs. Since they are mostly empty of matter, their evolution and structure is dominated by dark energy. Thus, they constitute a promising environment to test the nature of dark energy.

Measurements of voids and troughs properties can be made with weak gravitational lensing, namely: magnification and gg-lensing. The advantage of using these two methods is that they are complementary effects of the same physical phenomena but are sensitive to different systematic effects. Thus, the combination of these two weak-lensing methods to measure voids and trough profiles provide an accurate and reliable probe for the nature of dark energy.

Although wide-field surveys has provided the last years numerous weak-lensing results, magnification has been little studied due to its low signal-to-noise ratio compared with gg-lensing and to its sensitivity to systematic effects.

On this work, a technique to measure magnification with the number-count technique has been presented. In addition, a through and new way to take into account systematic errors has been presented, providing un-biased and reliable measurement.

Nevertheless, number-count magnification is not the measurement *per se*, but a proxy to the convergence profile of the lenses, the final physical observable. This implies that other types of magnification measurements –giving robustenss to the measurement– can be made as a proxy to the convergence: the magnitude and size shift.

Weak-lensing measurements are conceived as one of the four key probes for dark energy to be combined within the Dark Energy Survey. Nevertheless, magnification has shown to be very sensitive to systematic effects that complicate severely the combination of this measurement on a multi-probe fit. This does not imply that magnification can not be used as a competitive probe for Cosmology. The use of weak-lensing magnification as a stand-alone or in combination with gg-lensing on low-scale studies or extreme environments where dark energy dominates, constitute independent and alternative probes for gravity.

Unfortunately as of the day this Thesis started to be written –March 2017– no theoretical expression of the convergence profile of voids with non-cosmological-constant dark energy models is available. Nevertheless, it is known how to proceed: currently available General Relativity LTB void profiles can be assumed as *a posteriori* solution on LTB $f(R)$ modified gravity models. This leads to a subset of $f(R)$ models that can be constrained. Then, with this models, angular diameter distances can be computed and from them the convergence profile. This leads to a physical observable that allow to discriminate between General Relativity and an specific subset of modified gravity models, task that will be addressed on the near future.

Although, the determination of void profiles with magnification constitutes a promising tool for the gravitational theory, other questions on Cosmology can be answered with weak-lensing magnification, such as the large-scale-structure of the Universe. Matter profile of dark matter halos can be measured on both galaxies and clusters, allowing to answer questions such as the nature of dark matter or the halo-bias connection.

The new way to take into account systematic effects developed on this thesis, stablish weak-lensing magnification as a robust, reliable, unbiased and competitive cosmological probe, that opens a new way to explore the Cosmos giving light on the dark Universe: dark matter and dark energy.

§ § §

My personal contribution to Science as part of The Dark Energy Survey Collaboration was to be the leader of the study of weak-lensing magnification both on the Science Verification and the Year 1 data releases. The summit of this Thesis is the publication of the Science Verification weak-lensing magnification measurement on a peer-review journal of which I am the first author. Although plenty of other studies has been made on the same data-set, they are still not published.

Other contributions include infrastructure work for The Dark Energy Survey

Collaboration: night observations at Cerro Tololo (Chile) and to produce the Balrog catalogs for the Year 1 data release.

In addition as infrastructure work for the PAU-Survey Collaboration include night observations at La Palma (Spain).

A. Stellar contamination equation

The observed density contrast of objects is given by

$$\delta_{\mathrm{O}}(\hat{\boldsymbol{n}}, z_i) = \frac{N_{\mathrm{g}}(z_i) + N_*(z_i)}{\bar{N}_{\mathrm{g}}(z_i) + \bar{N}_*(z_i)} - 1, \tag{A.1}$$

where N_{g}, N_* are the number of galaxies on direction $\hat{\boldsymbol{n}}$ and redshift z_i and stars respectively and $\bar{N}_{\mathrm{g}}, \bar{N}_*$ the average number of galaxies and stars over the footprint. The previous equation can be expressed as

$$\delta_{\mathrm{O}}(\hat{\boldsymbol{n}}, z_i) = \frac{N_{\mathrm{g}}(z_i) + N_*(z_i)}{\bar{N}_{\mathrm{g}}(z_i)\left[1 + \frac{\bar{N}_*(z_i)}{\bar{N}_{\mathrm{g}}(z_i)}\right]} - 1. \tag{A.2}$$

Taylor expanding the brackets one has,

$$\delta_{\mathrm{O}}(\hat{\boldsymbol{n}}, z_i) = \frac{N_{\mathrm{g}}(z_i) + N_*(z_i)}{\bar{N}_{\mathrm{g}}(z_i)}\left[1 - \frac{\bar{N}_*(z_i)}{\bar{N}_{\mathrm{g}}(z_i)}\right] - 1 \tag{A.3}$$

and taking common factor $\bar{N}_*(z_i)/\bar{N}_{\mathrm{g}}(z_i)$,

$$\begin{gathered}\delta_{\mathrm{O}}(z_i) = \left[\frac{N_{\mathrm{g}}(z_i)}{\bar{N}_{\mathrm{g}}(z_i)} - 1\right] + \\ \frac{\bar{N}_*(z_i)}{\bar{N}_{\mathrm{g}}(z_i)}\left[\frac{N_*(z_i)}{\bar{N}_*(z_i)} - \frac{N_{\mathrm{g}}(z_i)}{\bar{N}_{\mathrm{g}}(z_i)}\right] - \frac{N_*(z_i)}{\bar{N}_{\mathrm{g}}(z_i)}.\end{gathered} \tag{A.4}$$

Assuming that $\bar{N}_* \ll \bar{N}_g$, the last term can be neglected and defining $\lambda_i = \bar{N}_*(z_i)/\bar{N}_{\mathrm{g}}(z_i)$ as the fraction of stars on the i-th sample,

$$\delta_{\mathrm{O}}(\hat{\boldsymbol{n}}, z_i) = \delta_{\mathrm{g}}(\hat{\boldsymbol{n}}, z_i) + \lambda_i[\delta_*(\hat{\boldsymbol{n}}, z_i) - \delta_{\mathrm{g}}(\hat{\boldsymbol{n}}, z_i)]. \tag{A.5}$$

Calculating the two point angular cross-correlation results finally in

$$\omega_{\mathrm{O}} = (1 - \lambda_i - \lambda_j)\omega_{\mathrm{gg}} + \lambda_j\omega_{\mathrm{g}*} + \lambda_i\omega_{*\mathrm{g}} + \lambda_i\lambda_j\omega_{**}. \tag{A.6}$$

B. Additional figures

Here the plots and graphs not included on the main text are included.

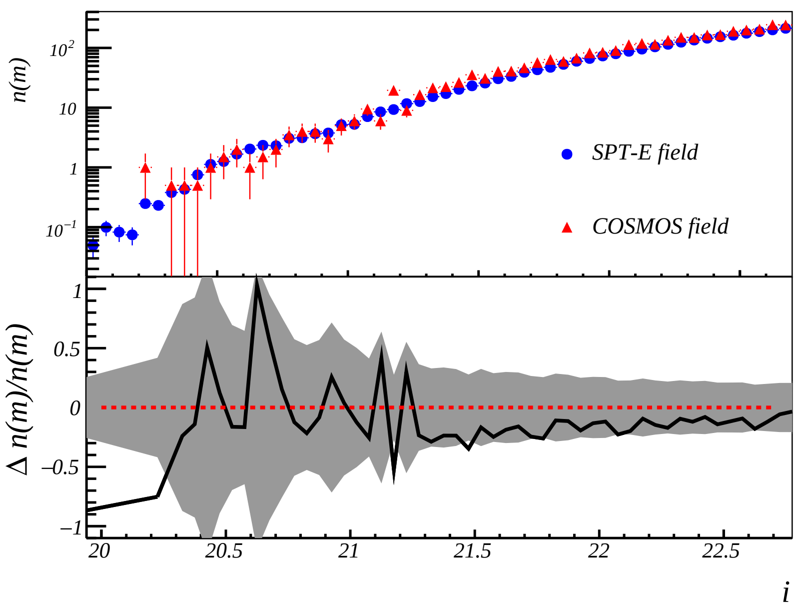

Figure B.1: Upper panel: Comparison of the magnitude distribution for the SPT-E and the COSMOS fields for the r band.

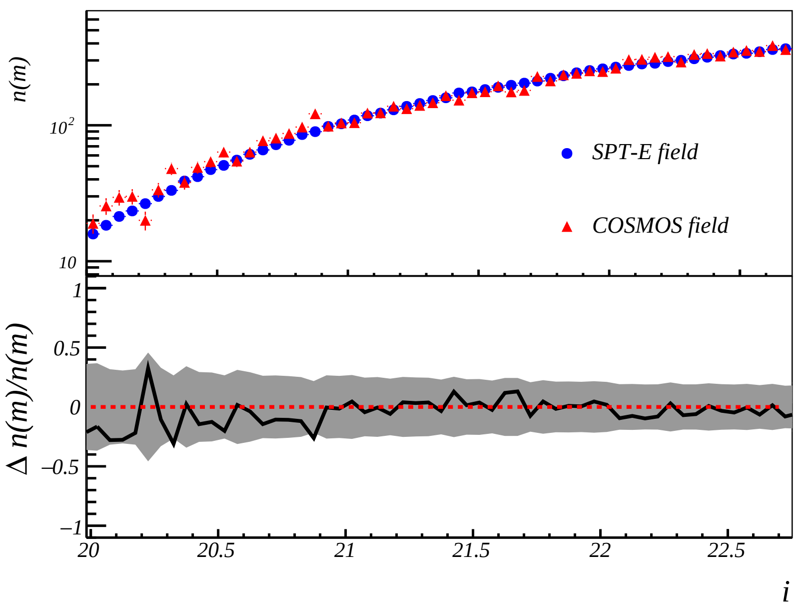

Figure B.2: Upper panel: Comparison of the magnitude distribution for the SPT-E and the COSMOS fields for the z band.

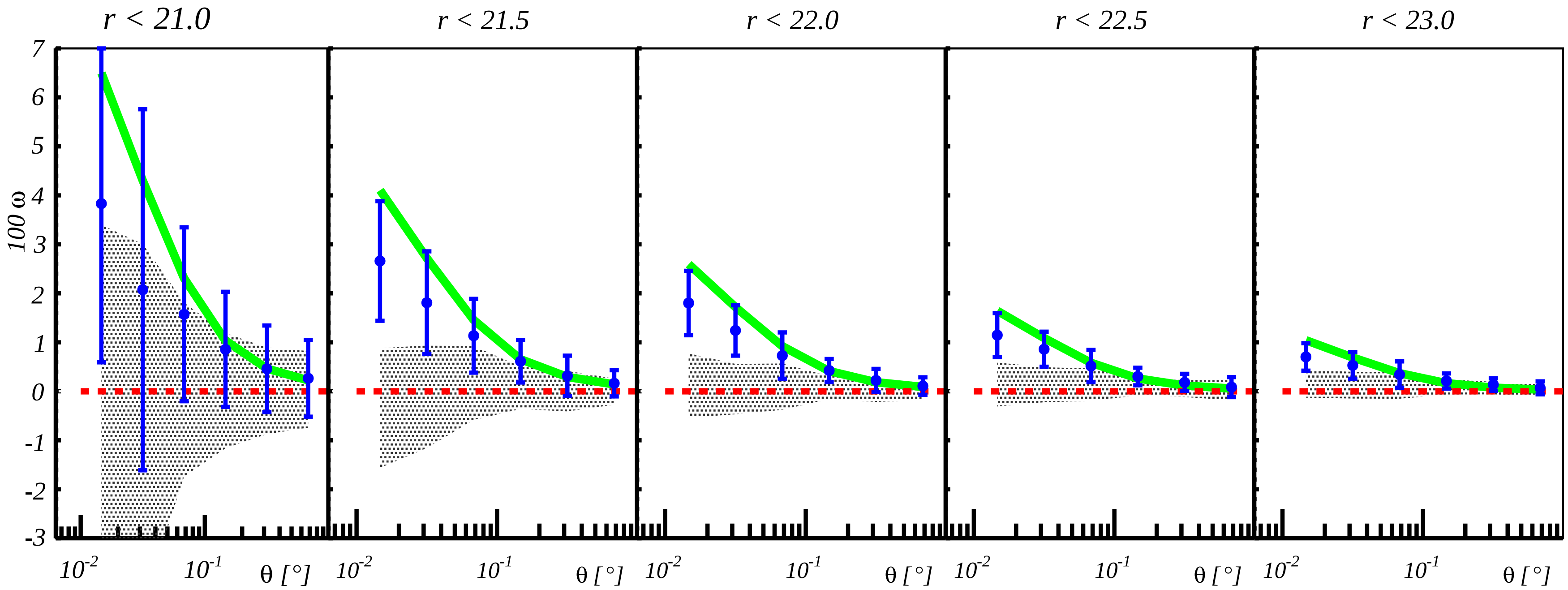

Figure B.3: MICE r-band.

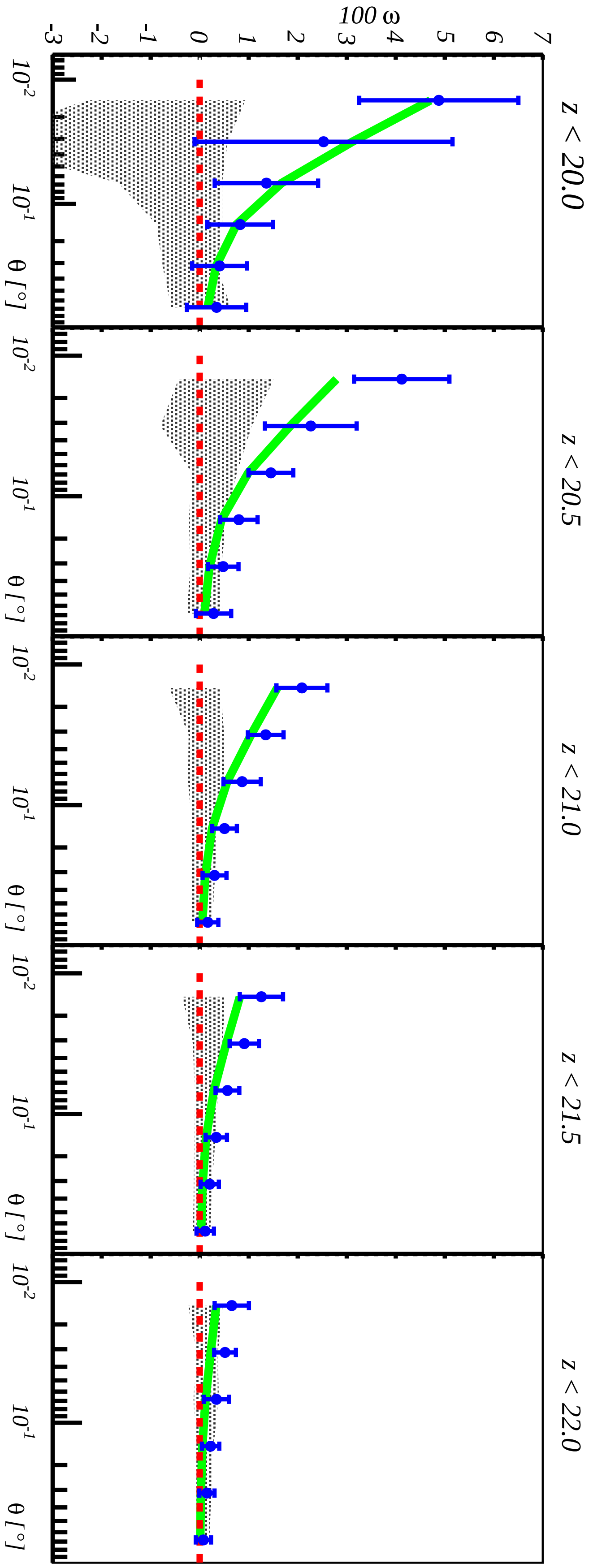

Figure B.4: MICE z-band.

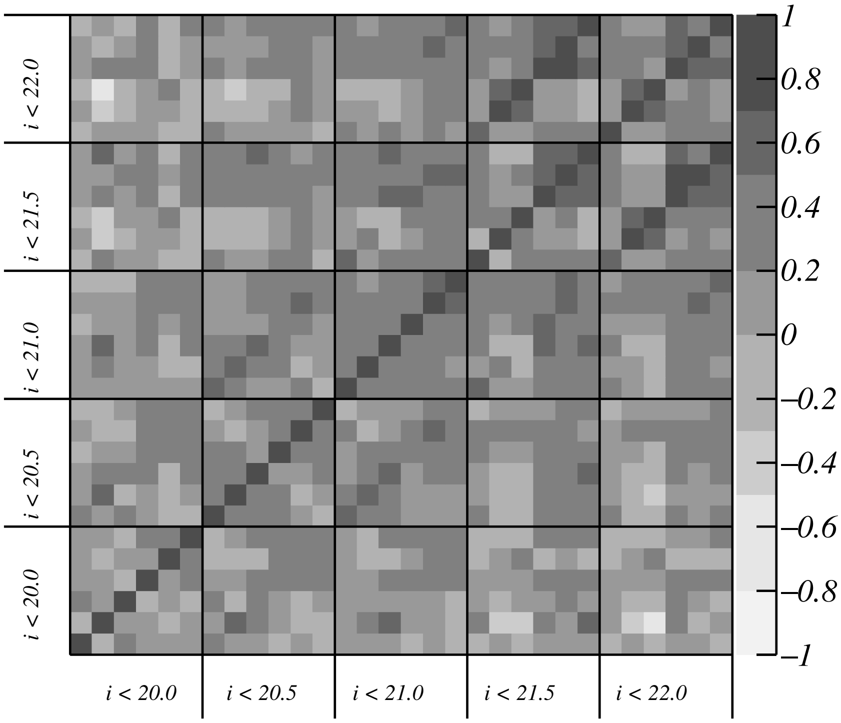

Figure B.5: Covariance matrix of the r-band rescaled by the value of the diagonal.

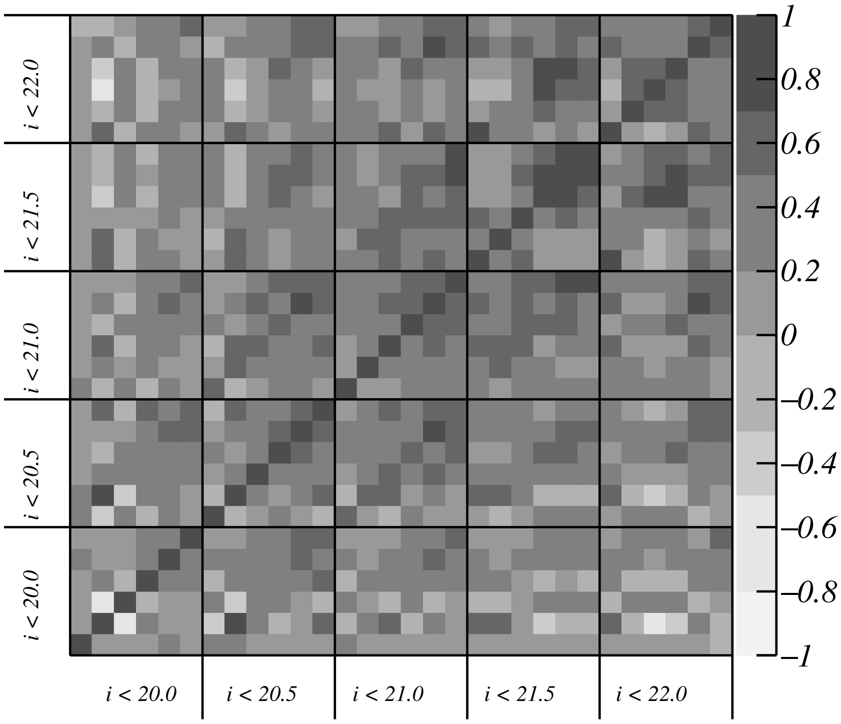

Figure B.6: Covariance matrix of the z-band rescaled by the value of the diagonal.

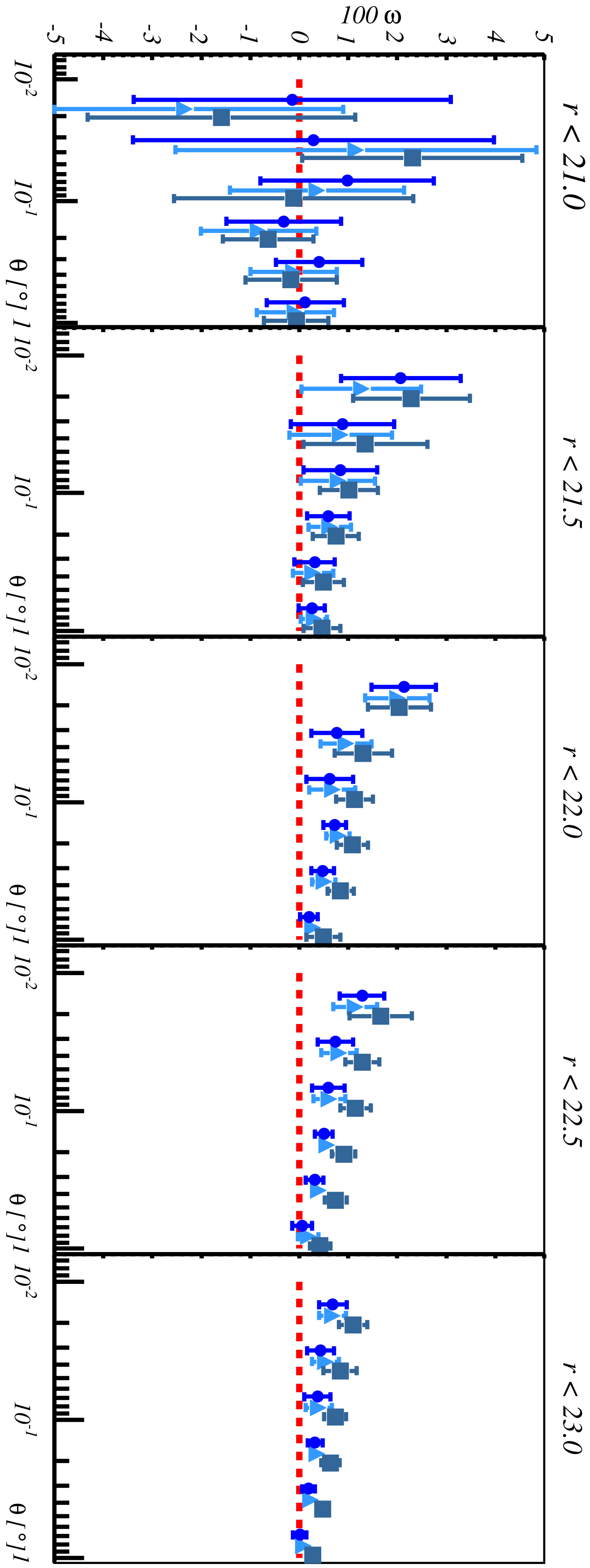

Figure B.7: DES-SV r-band photo-z comparison.

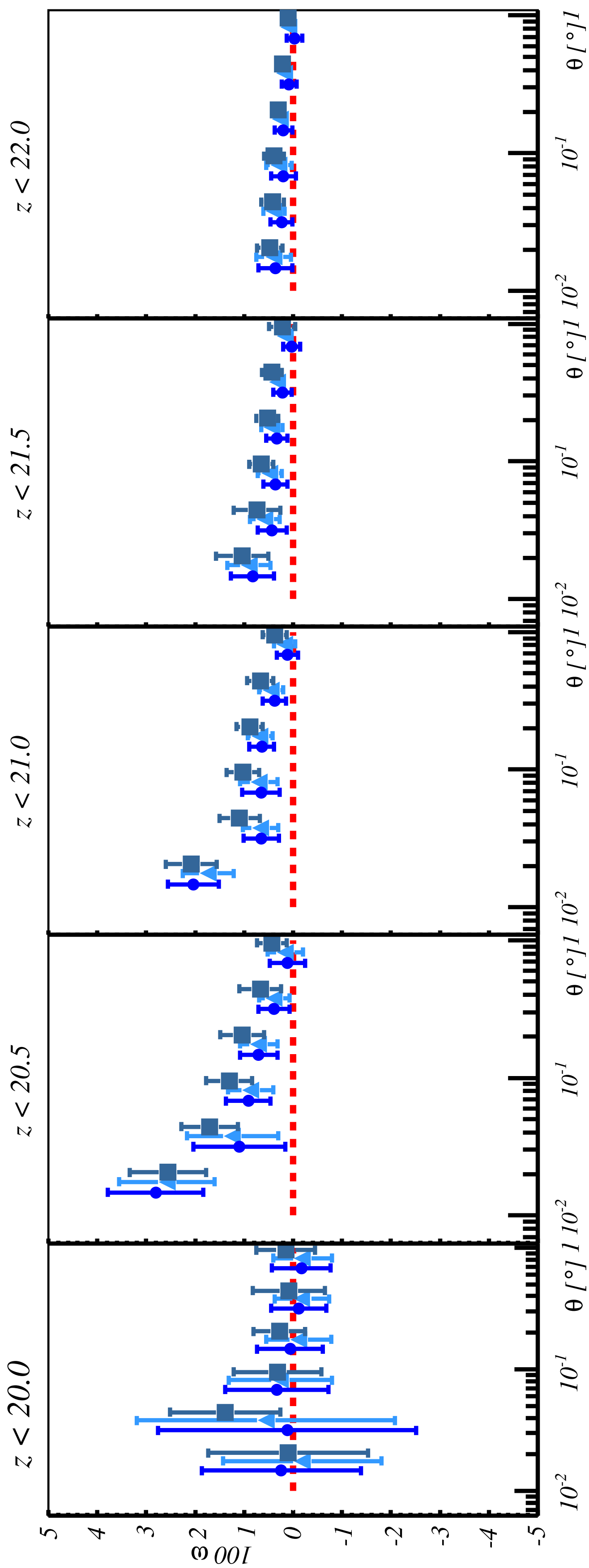

Figure B.8: DES-SV z-band photo-z comparison.

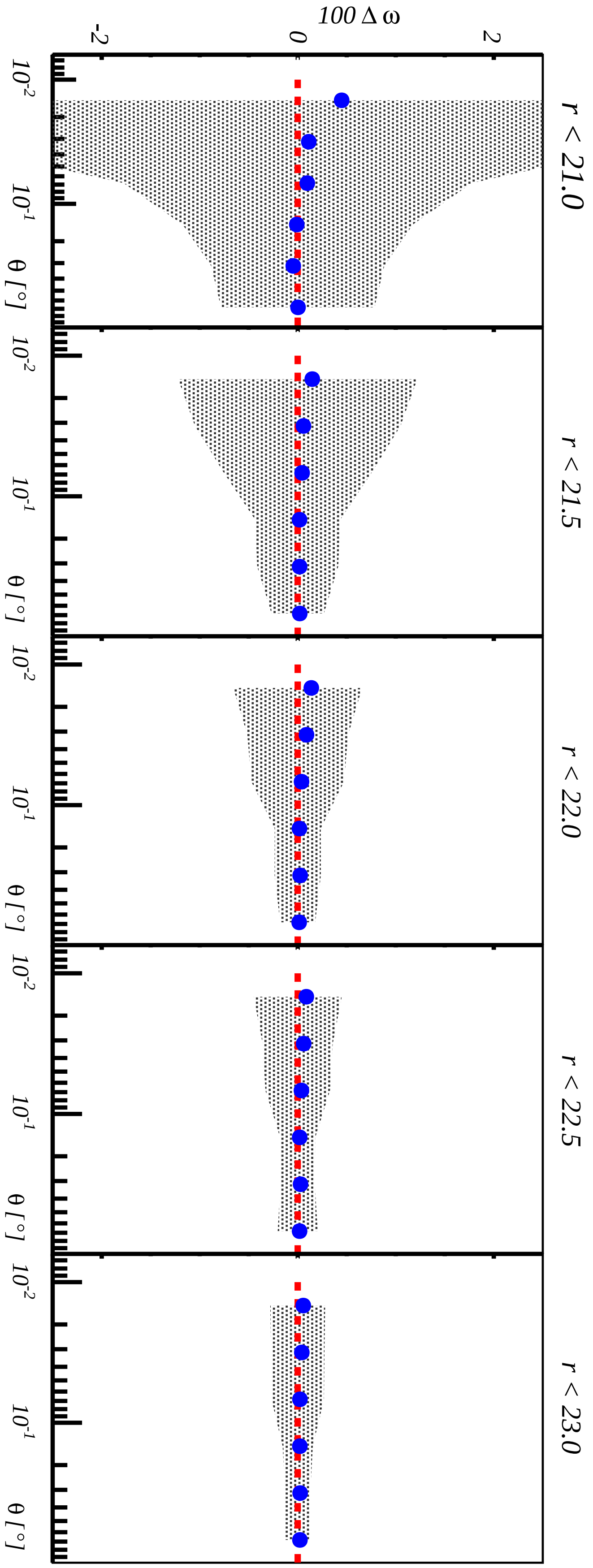

Figure B.9: DES-SV r-band estimation of dust extinction with MICE.

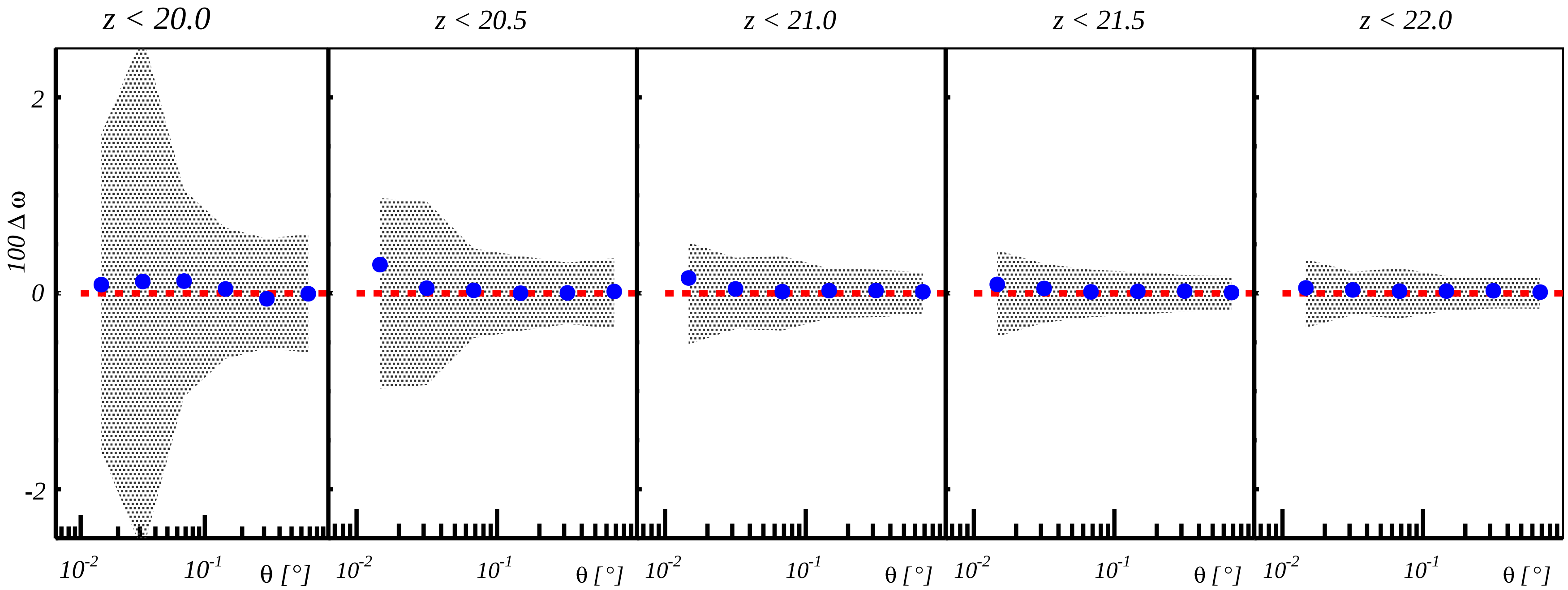

Figure B.10: DES-SV z-band estimation of dust extinction with MICE.

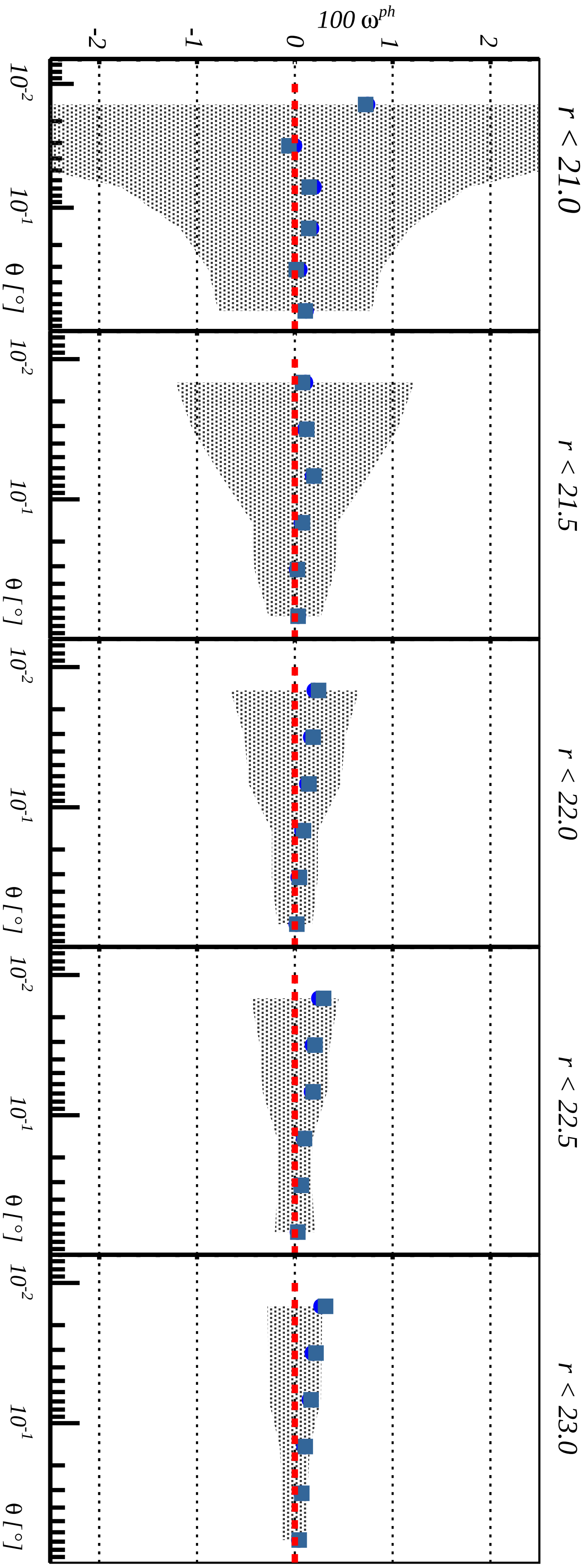

Figure B.11: DES-SV z-band estimation of photo-z induced signal with MICE.

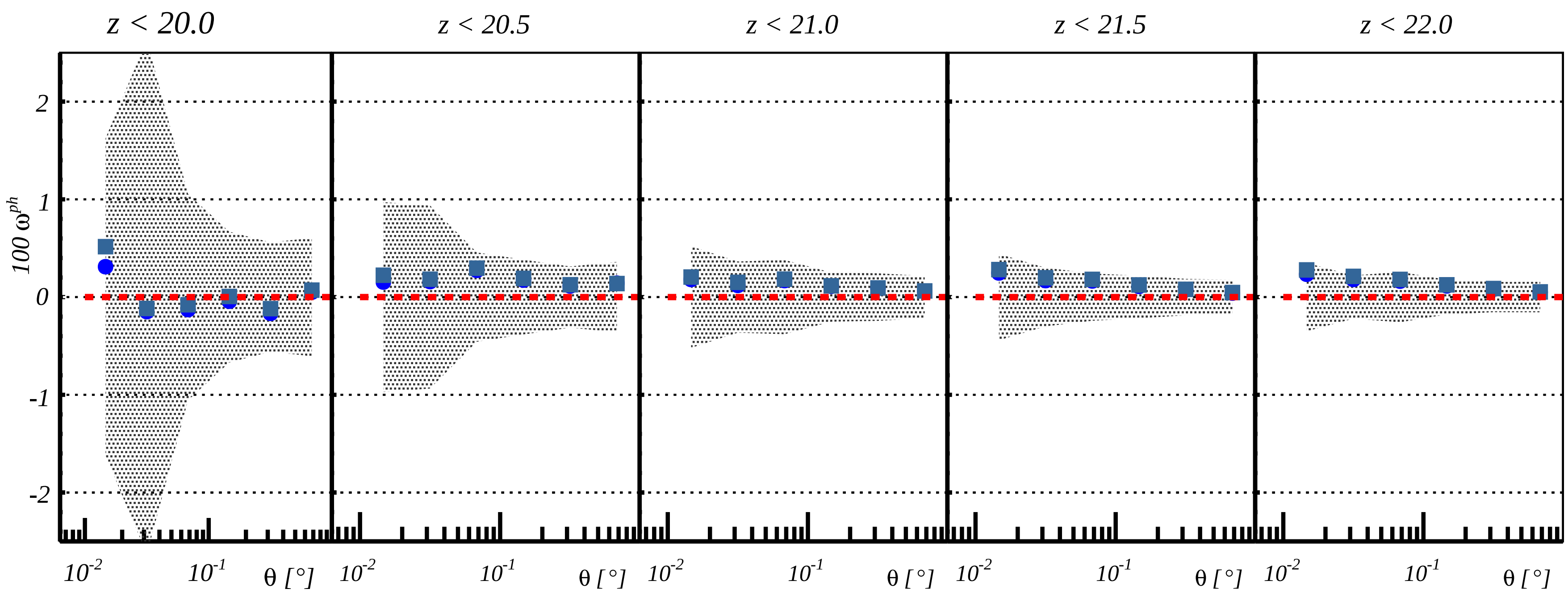

Figure B.12: DES-SV z-band estimation of photo-z induced signal with MICE.

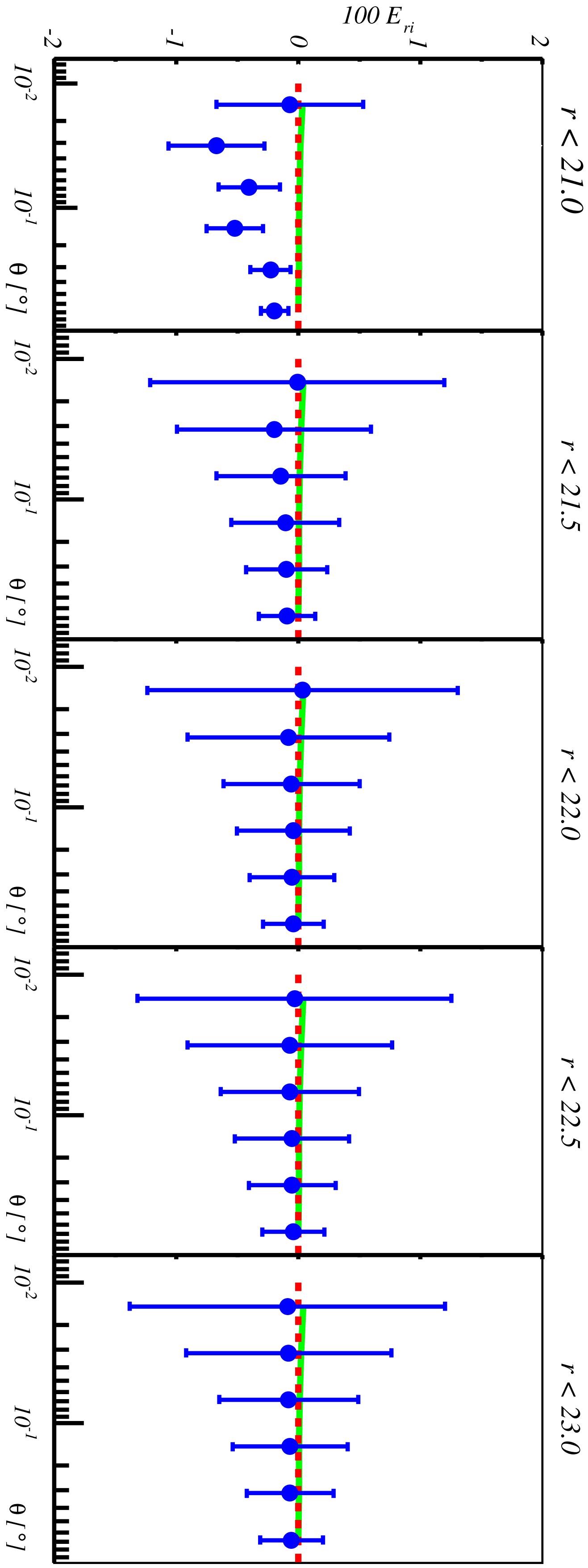

Figure B.13: DES-SV r-band estimation of the $r - i$ color excess.

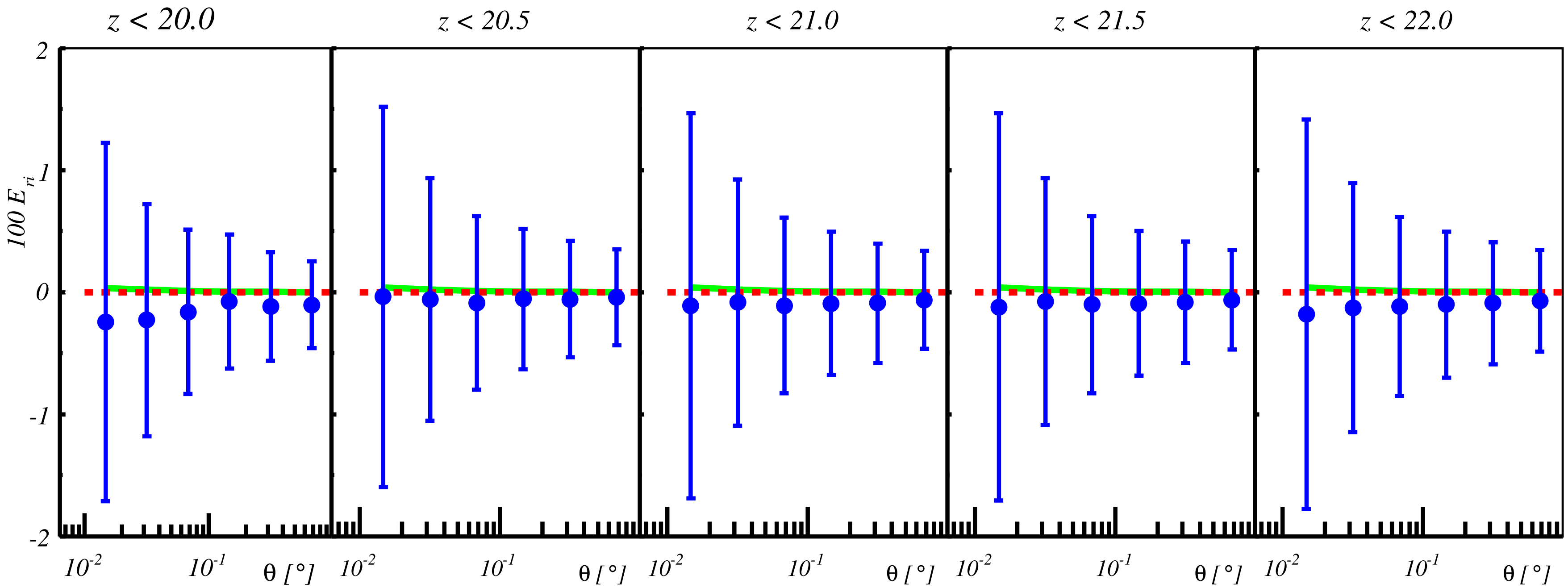

Figure B.14: DES-SV z-band estimation of the $r - i$ color excess.

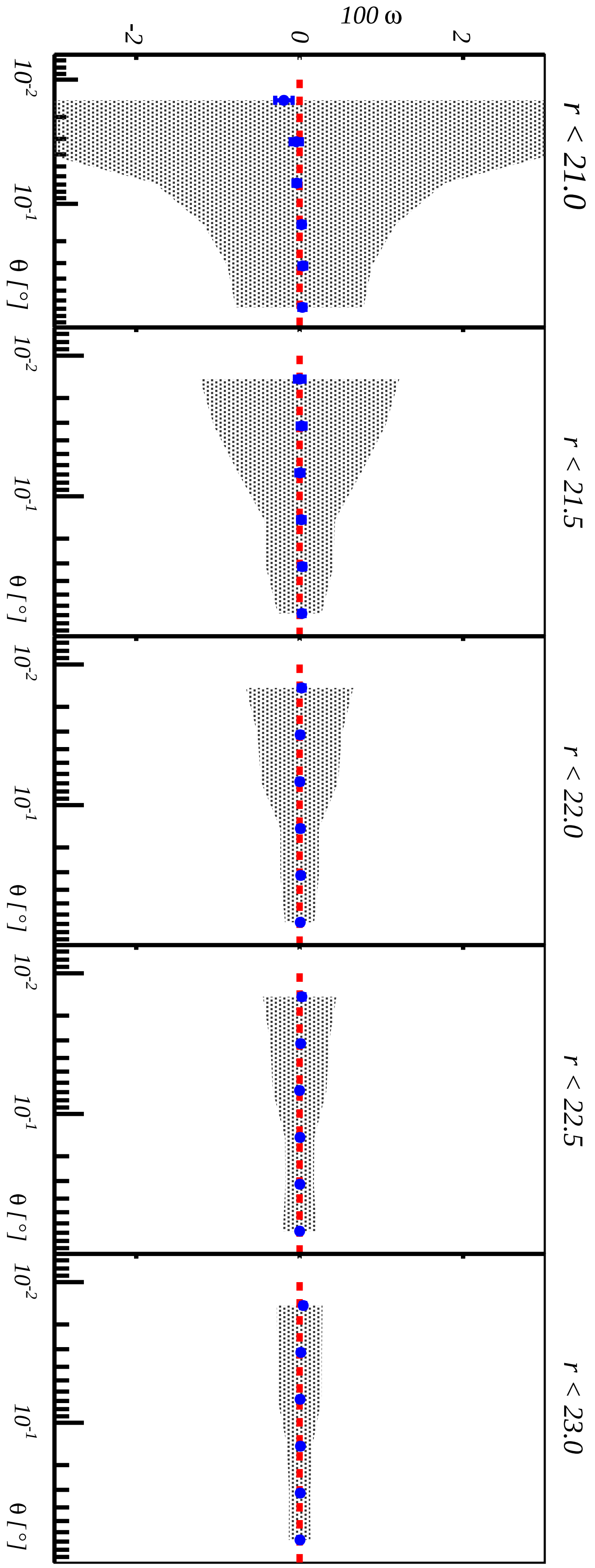

Figure B.15: DES-SV r-band estimation of the signal induced by stellar contamination.

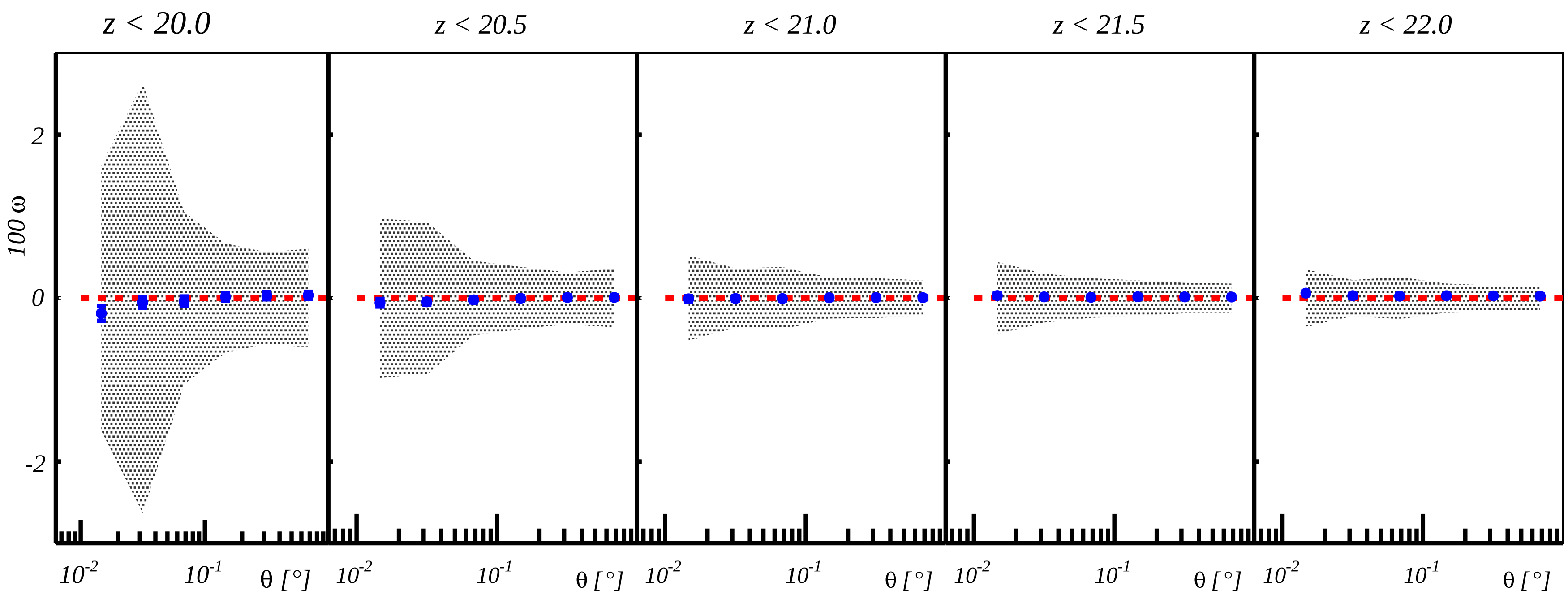

Figure B.16: DES-SV z-band estimation of the signal induced by the stellar contamination.

References

[1] F. Halzen and A.D. Martin. *Quarks and leptons: an introductory course in modern particle physics*. Wiley, 1984. URL: https://books.google.es/books?id=zwDvAAAAMAAJ.

[2] M.E. Peskin and D.V. Schroeder. *An Introduction to Quantum Field Theory*. Advanced book classics. Avalon Publishing, 1995. ISBN: 9780201503975. URL: https://books.google.es/books?id=i35LALN0GosC.

[3] S. Weinberg. *The Quantum Theory of Fields*. The Quantum Theory of Fields 3 Volume Hardback Set v. 1. Cambridge University Press, 1995. ISBN: 9780521550017. URL: https://books.google.es/books?id=doeDB3%5C_WLvwC.

[4] S. Weinberg. *The Quantum Theory of Fields: Volume 2, Modern Applications*. Cambridge University Press, 1996. ISBN: 9781139643252. URL: https://books.google.es/books?id=J2EhAwAAQBAJ.

[5] S. F. Novaes. "Standard Model: An Introduction". In: *ArXiv High Energy Physics - Phenomenology e-prints* (Jan. 2000). eprint: hep-ph/0001283.

[6] A. Einstein. "Die Grundlage der allgemeinen Relativitätstheorie". In: *Annalen der Physik* 354.7 (1916), pp. 769–822. ISSN: 1521-3889. DOI: 10.1002/andp.19163540702. URL: http://dx.doi.org/10.1002/andp.19163540702.

[7] A. Einstein. "Die Grundlage der allgemeinen Relativitätstheorie". In: *Annalen der Physik* 354 (1916), pp. 769–822. DOI: 10.1002/andp.19163540702.

[8] A. Einstein. "Kosmologische Betrachtungen zur allgemeinen Relativitätstheorie". In: *Sitzungsberichte der Königlich Preußischen Akademie der Wissenschaften (Berlin), Seite 142-152.* (1917).

[9] S. M. Carroll. "The Cosmological Constant". In: *Living Reviews in Relativity* 4, 1 (Dec. 2001), p. 1. DOI: 10.12942/lrr-2001-1. eprint: astro-ph/0004075.

[10] David Hilbert. “Die Grundlagen der Physik. 1.” In: *Gott. Nachr.* 27 (1915), pp. 395–407.

[11] D. Alonso et al. “Measuring the transition to homogeneity with photometric redshift surveys”. In: *MNRAS* 440 (May 2014), pp. 10–23. DOI: 10.1093/mnras/stu255. arXiv: 1312.0861 [astro-ph.CO].

[12] D. Alonso et al. “Homogeneity and isotropy in the Two Micron All Sky Survey Photometric Redshift catalogue”. In: *MNRAS* 449 (May 2015), pp. 670–684. DOI: 10.1093/mnras/stv309. arXiv: 1412.5151.

[13] G. Lemaître. “Un Univers homogène de masse constante et de rayon croissant rendant compte de la vitesse radiale des nébuleuses extra-galactiques”. In: *Annales de la Société Scientifique de Bruxelles* 47 (1927), pp. 49–59.

[14] M. Betoule et al. “Improved cosmological constraints from a joint analysis of the SDSS-II and SNLS supernova samples”. In: *A&A* 568, A22 (Aug. 2014), A22. DOI: 10.1051/0004-6361/201423413. arXiv: 1401.4064.

[15] Planck Collaboration et al. “Planck 2015 results. XIII. Cosmological parameters”. In: *ArXiv e-prints* (Feb. 2015). arXiv: 1502.01589.

[16] D.-C. Dai, R. Matsuo, and G. Starkman. “Gravitational lenses in generalized Einstein-aether theory: The bullet cluster”. In: *Phys. Rev. D* 78.10, 104004 (Nov. 2008), p. 104004. DOI: 10.1103/PhysRevD.78.104004. arXiv: 0806.4319 [gr-qc].

[17] Steven Weinberg. “The cosmological constant problem”. In: *Rev. Mod. Phys.* 61 (1 Jan. 1989), pp. 1–23. DOI: 10.1103/RevModPhys.61.1. URL: https://link.aps.org/doi/10.1103/RevModPhys.61.1.

[18] T. Padmanabhan. “Cosmological constant-the weight of the vacuum”. In: *Phys. Rep.* 380 (July 2003), pp. 235–320. DOI: 10.1016/S0370-1573(03)00120-0. eprint: hep-th/0212290.

[19] R. L. Jaffe. “Casimir effect and the quantum vacuum”. In: *Phys. Rev. D* 72 (2 July 2005), p. 021301. DOI: 10.1103/PhysRevD.72.021301. URL: https://link.aps.org/doi/10.1103/PhysRevD.72.021301.

[20] Ya B Zel’dovich. “THE COSMOLOGICAL CONSTANT AND THE THEORY OF ELEMENTARY PARTICLES”. In: *Soviet Physics Uspekhi* 11.3 (1968), p. 381. URL: http://stacks.iop.org/0038-5670/11/i=3/a=A13.

[21] A. D. Linde. “Is the Lee constant a cosmological constant?” In: *Soviet Journal of Experimental and Theoretical Physics Letters* 19 (Mar. 1974), p. 183.

[22] M. Veltman. “Cosmology and the Higgs Mass”. In: *Phys. Rev. Lett.* 34 (12 Mar. 1975), pp. 777–777. DOI: 10.1103/PhysRevLett.34.777. URL: https://link.aps.org/doi/10.1103/PhysRevLett.34.777.

[23] P. H. Brax and J. Martin. “Quintessence and supergravity”. In: *Physics Letters B* 468 (Nov. 1999), pp. 40–45. DOI: 10.1016/S0370-2693(99)01209-5. eprint: astro-ph/9905040.

[24] P. Brax and J. Martin. "Cosmological Implications of the Supergravity Tracking Potential". In: *ArXiv Astrophysics e-prints* (Nov. 1999). eprint: astro-ph/9912005.

[25] P. Brax and J. Martin. "Robustness of quintessence". In: *Phys. Rev. D* 61.10, 103502 (May 2000), p. 103502. DOI: 10.1103/PhysRevD.61.103502. eprint: astro-ph/9912046.

[26] P. Binétruy. "Models of dynamical supersymmetry breaking and quintessence". In: *Phys. Rev. D* 60.6, 063502 (Sept. 1999), p. 063502. DOI: 10.1103/PhysRevD.60.063502. eprint: hep-ph/9810553.

[27] L. Amendola and S. Tsujikawa. *Dark Energy: Theory and Observations*. 2010.

[28] P. Bechtle, T. Plehn, and C. Sander. "The Status of Supersymmetry after the LHC Run 1". In: *ArXiv e-prints* (June 2015). arXiv: 1506.03091 [hep-ex].

[29] A. De Felice and S. Tsujikawa. "f(R) Theories". In: *Living Reviews in Relativity* 13, 3 (Dec. 2010), p. 3. DOI: 10.12942/lrr-2010-3. arXiv: 1002.4928 [gr-qc].

[30] T. P. Sotiriou and V. Faraoni. "f(R) theories of gravity". In: *Reviews of Modern Physics* 82 (Jan. 2010), pp. 451–497. DOI: 10.1103/RevModPhys.82.451. arXiv: 0805.1726 [gr-qc].

[31] Mohamed Abdelwahab, Rituparno Goswami, and Peter K. S. Dunsby. "Cosmological dynamics of fourth-order gravity: A compact view". In: *Phys. Rev. D* 85 (8 Apr. 2012), p. 083511. DOI: 10.1103/PhysRevD.85.083511. URL: https://link.aps.org/doi/10.1103/PhysRevD.85.083511.

[32] A. M. Nzioki et al. "Geometrical approach to strong gravitational lensing in f(R) gravity". In: *Phys. Rev. D* 83.2, 024030 (Jan. 2011), p. 024030. DOI: 10.1103/PhysRevD.83.024030. arXiv: 1002.2056 [gr-qc].

[33] R. Gavazzi et al. "The Sloan Lens ACS Survey. VI. Discovery and Analysis of a Double Einstein Ring". In: *ApJ* 677, 1046-1059 (Apr. 2008), pp. 1046–1059. DOI: 10.1086/529541. arXiv: 0801.1555.

[34] E. Berti et al. "Testing general relativity with present and future astrophysical observations". In: *Classical and Quantum Gravity* 32.24, 243001 (Dec. 2015), p. 243001. DOI: 10.1088/0264-9381/32/24/243001. arXiv: 1501.07274 [gr-qc].

[35] C. D. Leonard, T. Baker, and P. G. Ferreira. "Exploring degeneracies in modified gravity with weak lensing". In: *Phys. Rev. D* 91.8, 083504 (Apr. 2015), p. 083504. DOI: 10.1103/PhysRevD.91.083504. arXiv: 1501.03509.

[36] T. Baker, P. G. Ferreira, and C. Skordis. "The parameterized post-Friedmann framework for theories of modified gravity: Concepts, formalism, and examples". In: *Phys. Rev. D* 87.2, 024015 (Jan. 2013), p. 024015. DOI: 10.1103/PhysRevD.87.024015. arXiv: 1209.2117 [astro-ph.CO].

[37] David H. Weinberg et al. “Observational probes of cosmic acceleration”. In: *Physics Reports* 530.2 (2013). Observational Probes of Cosmic Acceleration, pp. 87–255. ISSN: 0370-1573. DOI: http://dx.doi.org/10.1016/j.physrep.2013.05.001. URL: http://www.sciencedirect.com/science/article/pii/S0370157313001592.

[38] C. Alcock and B. Paczynski. “An evolution free test for non-zero cosmological constant”. In: *Nature* 281 (Oct. 1979), p. 358. DOI: 10.1038/281358a0.

[39] C. Yèche et al. “Prospects for dark energy evolution: a frequentist multi-probe approach”. In: *A&A* 448 (Mar. 2006), pp. 831–842. DOI: 10.1051/0004-6361:20053786. eprint: astro-ph/0507170.

[40] E. Krause and T. Eifler. “CosmoLike - Cosmological Likelihood Analyses for Photometric Galaxy Surveys”. In: *ArXiv e-prints* (Jan. 2016). arXiv: 1601.05779.

[41] E. Schaan et al. “Looking through the same lens: shear calibration for LSST, Euclid, WFIRST with stage 4 CMB lensing”. In: *ArXiv e-prints* (July 2016). arXiv: 1607.01761.

[42] S. Samuroff et al. “Simultaneous constraints on cosmology and photometric redshift bias from weak lensing and galaxy clustering”. In: *MNRAS* 465 (Feb. 2017), pp. L20–L24. DOI: 10.1093/mnrasl/slw201. arXiv: 1607.07910.

[43] O. Friedrich and T. Eifler. “Precision matrix expansion - efficient use of numerical simulations in estimating errors on cosmological parameters”. In: *ArXiv e-prints* (Mar. 2017). arXiv: 1703.07786 [astro-ph.IM].

[44] H. Hildebrandt. “Observational biases in flux magnification measurements”. In: *MNRAS* 455 (Feb. 2016), pp. 3943–3951. DOI: 10.1093/mnras/stv2575. arXiv: 1511.01352.

[45] B. Li, G.-B. Zhao, and K. Koyama. “Haloes and voids in f(R) gravity”. In: *MNRAS* 421 (Apr. 2012), pp. 3481–3487. DOI: 10.1111/j.1365-2966.2012.20573.x. arXiv: 1111.2602 [astro-ph.CO].

[46] F. von Braun-Bates et al. “The f(Script R) halo mass function in the cosmic web”. In: *J. Cosmology Astropart. Phys.* 3, 012 (Mar. 2017), p. 012. DOI: 10.1088/1475-7516/2017/03/012. arXiv: 1702.06817.

[47] G. Lavaux and B. D. Wandelt. “Precision cosmology with voids: definition, methods, dynamics”. In: *MNRAS* 403 (Apr. 2010), pp. 1392–1408. DOI: 10.1111/j.1365-2966.2010.16197.x. arXiv: 0906.4101.

[48] Guilhem Lavaux and Benjamin D. Wandelt. “Precision Cosmography with Stacked Voids”. In: *The Astrophysical Journal* 754.2 (2012), p. 109. URL: http://stacks.iop.org/0004-637X/754/i=2/a=109.

[49] Daeseong Park and Jounghun Lee. “Void Ellipticity Distribution as a Probe of Cosmology”. In: *Phys. Rev. Lett.* 98 (8 Feb. 2007), p. 081301. DOI: 10.1103/PhysRevLett.98.081301. URL: https://link.aps.org/doi/10.1103/PhysRevLett.98.081301.

[50] D. Spolyar, M. Sahlén, and J. Silk. "Topology and Dark Energy: Testing Gravity in Voids". In: *Physical Review Letters* 111.24, 241103 (Dec. 2013), p. 241103. DOI: 10.1103/PhysRevLett.111.241103. arXiv: 1304.5239 [astro-ph.CO].

[51] E. V. Arbuzova, A. D. Dolgov, and L. Reverberi. "Spherically symmetric solutions in F (R) gravity and gravitational repulsion". In: *Astroparticle Physics* 54 (Feb. 2014), pp. 44–47. DOI: 10.1016/j.astropartphys.2013.11.008. arXiv: 1306.5694 [gr-qc].

[52] Y.-C. Cai, N. Padilla, and B. Li. "Testing Gravity using Void Profiles". In: *ArXiv e-prints* (Oct. 2014). arXiv: 1410.8355.

[53] P. Zivick et al. "Using cosmic voids to distinguish f(R) gravity in future galaxy surveys". In: *MNRAS* 451 (Aug. 2015), pp. 4215–4222. DOI: 10.1093/mnras/stv1209. arXiv: 1411.5694.

[54] A. Barreira et al. "Weak lensing by voids in modified lensing potentials". In: *J. Cosmology Astropart. Phys.* 8, 028 (Aug. 2015), p. 028. DOI: 10.1088/1475-7516/2015/08/028. arXiv: 1505.05809.

[55] I. Achitouv et al. "Imprint of f (R) gravity on nonlinear structure formation". In: *Phys. Rev. D* 93.10, 103522 (May 2016), p. 103522. DOI: 10.1103/PhysRevD.93.103522. arXiv: 1511.01494.

[56] I. Achitouv. "Testing the imprint of nonstandard cosmologies on void profiles using Monte Carlo random walks". In: *Phys. Rev. D* 94.10, 103524 (Nov. 2016), p. 103524. DOI: 10.1103/PhysRevD.94.103524. arXiv: 1609.01284.

[57] Planck Collaboration et al. "Planck 2015 results. XIV. Dark energy and modified gravity". In: *A&A* 594, A14 (Sept. 2016), A14. DOI: 10.1051/0004-6361/201525814. arXiv: 1502.01590.

[58] X.-D. Li et al. "Cosmological Constraints from the Redshift Dependence of the Alcock-Paczynski Effect: Application to the SDSS-III BOSS DR12 Galaxies". In: *ApJ* 832, 103 (Dec. 2016), p. 103. DOI: 10.3847/0004-637X/832/2/103. arXiv: 1609.05476.

[59] S. Alam et al. "The clustering of galaxies in the completed SDSS-III Baryon Oscillation Spectroscopic Survey: cosmological analysis of the DR12 galaxy sample". In: *ArXiv e-prints* (July 2016). arXiv: 1607.03155.

[60] Y. Wang et al. "The clustering of galaxies in the completed SDSS-III Baryon Oscillation Spectroscopic Survey: tomographic BAO analysis of DR12 combined sample in configuration space". In: *ArXiv e-prints* (July 2016). arXiv: 1607.03154.

[61] J. E. Bautista et al. "Measurement of BAO correlations at $z = 2.3$ with SDSS DR12 \lya-Forests". In: *ArXiv e-prints* (Feb. 2017). arXiv: 1702.00176.

[62] H. Gil-Marín et al. "The clustering of galaxies in the SDSS-III Baryon Oscillation Spectroscopic Survey: RSD measurement from the power spectrum and bispectrum of the DR12 BOSS galaxies". In: *MNRAS* 465 (Feb. 2017), pp. 1757–1788. DOI: 10.1093/mnras/stw2679. arXiv: 1606.00439.

[63] A. G. Riess et al. “A 2.4% Determination of the Local Value of the Hubble Constant”. In: *ApJ* 826, 56 (July 2016), p. 56. DOI: 10.3847/0004-637X/826/1/56. arXiv: 1604.01424.

[64] Planck Collaboration et al. “Planck 2013 results. XVI. Cosmological parameters”. In: *A&A* 571, A16 (Nov. 2014), A16. DOI: 10.1051/0004-6361/201321591. arXiv: 1303.5076.

[65] M. Kilbinger et al. “CFHTLenS: combined probe cosmological model comparison using 2D weak gravitational lensing”. In: *MNRAS* 430 (Apr. 2013), pp. 2200–2220. DOI: 10.1093/mnras/stt041. arXiv: 1212.3338.

[66] J. Harnois-Déraps et al. “KiDS-450: Tomographic Cross-Correlation of Galaxy Shear with {\it Planck} Lensing”. In: *ArXiv e-prints* (Mar. 2017). arXiv: 1703.03383.

[67] S. Joudaki et al. “KiDS-450: Testing extensions to the standard cosmological model”. In: *ArXiv e-prints* (Oct. 2016). arXiv: 1610.04606.

[68] J. N. Dossett et al. “Constraints and tensions in testing general relativity from Planck and CFHTLenS data including intrinsic alignment systematics”. In: *Phys. Rev. D* 92.2, 023003 (July 2015), p. 023003. DOI: 10.1103/PhysRevD.92.023003. arXiv: 1501.03119.

[69] S. Joudaki et al. “CFHTLenS revisited: assessing concordance with Planck including astrophysical systematics”. In: *MNRAS* 465 (Feb. 2017), pp. 2033–2052. DOI: 10.1093/mnras/stw2665. arXiv: 1601.05786.

[70] A. Leauthaud et al. “Lensing is low: cosmology, galaxy formation or new physics?” In: *MNRAS* 467 (May 2017), pp. 3024–3047. DOI: 10.1093/mnras/stx258. arXiv: 1611.08606.

[71] G.-B. Zhao et al. “The clustering of galaxies in the completed SDSS-III Baryon Oscillation Spectroscopic Survey: Examining the observational evidence for dynamical dark energy”. In: *ArXiv e-prints* (Jan. 2017). arXiv: 1701.08165.

[72] E. Di Valentino et al. “Constraining Dark Energy Dynamics in Extended Parameter Space”. In: *ArXiv e-prints* (Apr. 2017). arXiv: 1704.00762.

[73] J. H. Taylor and J. M. Weisberg. “A new test of general relativity - Gravitational radiation and the binary pulsar PSR 1913+16”. In: *ApJ* 253 (Feb. 1982), pp. 908–920. DOI: 10.1086/159690.

[74] B. P. Abbott et al. “Observation of Gravitational Waves from a Binary Black Hole Merger”. In: *Phys. Rev. Lett.* 116 (6 Feb. 2016), p. 061102. DOI: 10.1103/PhysRevLett.116.061102. URL: https://link.aps.org/doi/10.1103/PhysRevLett.116.061102.

[75] F. W. Dyson, A. S. Eddington, and C. Davidson. “A Determination of the Deflection of Light by the Sun’s Gravitational Field, from Observations Made at the Total Eclipse of May 29, 1919”. In: *Philosophical Transactions of the Royal Society of London A: Mathematical, Physical and Engineering Sciences* 220.571-581 (1920), pp. 291–333. ISSN: 0264-3952. DOI: 10.1098/rsta.1920.0009. eprint: http://rsta.royalsocietypublishing.org/content/220/571-581/291.full.pdf. URL: http://rsta.royalsocietypublishing.org/content/220/571-581/291.

[76] B. Nord et al. “Observation and Confirmation of Six Strong-lensing Systems in the Dark Energy Survey Science Verification Data”. In: *ApJ* 827, 51 (Aug. 2016), p. 51. DOI: 10.3847/0004-637X/827/1/51. arXiv: 1512.03062.

[77] C. Jacobs et al. “Finding strong lenses in CFHTLS using convolutional neural networks”. In: *ArXiv e-prints* (Apr. 2017). arXiv: 1704.02744 [astro-ph.IM].

[78] Steven Weinberg. *Gravitation and Cosmology: Principles and Applications of the General Theory of Relativity*. New York, NY: Wiley, 1972. URL: https://cds.cern.ch/record/100595.

[79] M. Bartelmann and P. Schneider. “Weak gravitational lensing”. In: *Phys. Rep.* 340 (Jan. 2001), pp. 291–472. DOI: 10.1016/S0370-1573(00)00082-X. eprint: astro-ph/9912508.

[80] G. Meylan et al., eds. *Gravitational Lensing: Strong, Weak and Micro*. 2006. eprint: astro-ph/0407232.

[81] H. Hoekstra and B. Jain. “Weak Gravitational Lensing and Its Cosmological Applications”. In: *Annual Review of Nuclear and Particle Science* 58 (Nov. 2008), pp. 99–123. DOI: 10.1146/annurev.nucl.58.110707.171151. arXiv: 0805.0139.

[82] L. van Waerbeke et al. “Magnification as a Probe of Dark Matter Halos at High Redshifts”. In: *The Astrophysical Journal Letters* 723.1 (2010), p. L13. URL: http://stacks.iop.org/2041-8205/723/i=1/a=L13.

[83] M. Kilbinger. “Cosmology with cosmic shear observations: a review”. In: *Reports on Progress in Physics* 78.8, 086901 (July 2015), p. 086901. DOI: 10.1088/0034-4885/78/8/086901. arXiv: 1411.0115.

[84] T. D. Kitching et al. “The Limits of Cosmic Shear”. In: *ArXiv e-prints* (Nov. 2016). arXiv: 1611.04954.

[85] M. Kilbinger et al. “Precision calculations of the cosmic shear power spectrum projection”. In: *ArXiv e-prints* (Feb. 2017). arXiv: 1702.05301.

[86] P. Lemos, A. Challinor, and G. Efstathiou. “The effect of Limber and flat-sky approximations on galaxy weak lensing”. In: *ArXiv e-prints* (Apr. 2017). arXiv: 1704.01054.

[87] R. D. Blandford et al. “Gravitational lens optics”. In: *Science* 245 (Aug. 1989), pp. 824–830. DOI: 10.1126/science.245.4920.824.

[88] M. Bartelmann. "Gravitational Lensing by Large-Scale Structures." In: *Reviews in Modern Astronomy*. Ed. by G. Klare. Vol. 5. Reviews in Modern Astronomy. 1992, pp. 259–270.

[89] M. Bartelmann. "Gravitational Lensing by Large-Scale Structures". In: *Gravitational Lenses*. Ed. by R. Kayser, T. Schramm, and L. Nieser. Vol. 406. Lecture Notes in Physics, Berlin Springer Verlag. 1992, p. 345. DOI: `10.1007/3-540-55797-0_122`.

[90] M. Bartelmann. "Cluster mass estimates from weak lensing." In: *A&A* 303 (Nov. 1995), p. 643. eprint: `astro-ph/9412051`.

[91] M. Bartelmann and R. Narayan. "Gravitational lensing and the mass distribution of clusters". In: *Dark Matter*. Ed. by S. S. Holt and C. L. Bennett. Vol. 336. American Institute of Physics Conference Series. July 1995, pp. 307–319. DOI: `10.1063/1.48350`. eprint: `astro-ph/9411033`.

[92] Lam Hui, Enrique Gaztañaga, and Marilena LoVerde. "Anisotropic magnification distortion of the 3D galaxy correlation. I. Real space". In: *Phys. Rev. D* 76 (10 Nov. 2007), p. 103502. DOI: `10.1103/PhysRevD.76.103502`. URL: `http://link.aps.org/doi/10.1103/PhysRevD.76.103502`.

[93] Lam Hui, Enrique Gaztañaga, and Marilena LoVerde. "Anisotropic magnification distortion of the 3D galaxy correlation. II. Fourier and redshift space". In: *Phys. Rev. D* 77 (6 Mar. 2008), p. 063526. DOI: `10.1103/PhysRevD.77.063526`. URL: `http://link.aps.org/doi/10.1103/PhysRevD.77.063526`.

[94] M. Bernardi et al. "Early-Type Galaxies in the Sloan Digital Sky Survey. III. The Fundamental Plane". In: *AJ* 125 (Apr. 2003), pp. 1866–1881. DOI: `10.1086/367794`. eprint: `astro-ph/0301626`.

[95] Eric M. Huff and Genevieve J. Graves. "Magnificent Magnification: Exploiting the Other Half of the Lensing Signal". In: *The Astrophysical Journal Letters* 780.2 (2014), p. L16. URL: `http://stacks.iop.org/2041-8205/780/i=2/a=L16`.

[96] Marilena LoVerde, Lam Hui, and Enrique Gaztañaga. "Lensing corrections to features in the angular two-point correlation function and power spectrum". In: *Phys. Rev. D* 77 (2 Jan. 2008), p. 023512. DOI: `10.1103/PhysRevD.77.023512`. URL: `http://link.aps.org/doi/10.1103/PhysRevD.77.023512`.

[97] D. Gruen et al. "Weak lensing by galaxy troughs in DES Science Verification data". In: *MNRAS* 455 (Jan. 2016), pp. 3367–3380. DOI: `10.1093/mnras/stv2506`. arXiv: `1507.05090`.

[98] B. Ménard et al. "Improving the accuracy of cosmic magnification statistics". In: *A&A* 403 (June 2003), pp. 817–828. DOI: `10.1051/0004-6361:20030406`. eprint: `astro-ph/0210112`.

[99] J. Garcia-Bellido and T. Haugbølle. “Confronting Lemaitre Tolman Bondi models with observational cosmology”. In: *J. Cosmology Astropart. Phys.* 4, 003 (Apr. 2008), p. 003. DOI: 10.1088/1475-7516/2008/04/003. arXiv: 0802.1523.

[100] F. Finelli et al. “Supervoids in the WISE-2MASS catalogue imprinting cold spots in the cosmic microwave background”. In: *MNRAS* 455 (Jan. 2016), pp. 1246–1256. DOI: 10.1093/mnras/stv2388. arXiv: 1405.1555.

[101] A. Kovács and J. García-Bellido. “Cosmic troublemakers: the Cold Spot, the Eridanus supervoid, and the Great Walls”. In: *MNRAS* 462 (Oct. 2016), pp. 1882–1893. DOI: 10.1093/mnras/stw1752. arXiv: 1511.09008.

[102] The Dark Energy Survey Collaboration. “The Dark Energy Survey”. In: *ArXiv Astrophysics e-prints* (Oct. 2005). eprint: astro-ph/0510346.

[103] A. Agnello et al. “Discovery of two gravitationally lensed quasars in the Dark Energy Survey”. In: *MNRAS* 454 (Dec. 2015), pp. 1260–1265. DOI: 10.1093/mnras/stv2171. arXiv: 1508.01203.

[104] H. Lin et al. “Discovery of the Lensed Quasar System DES J0408-5354”. In: *ApJ* 838, L15 (Apr. 2017), p. L15. DOI: 10.3847/2041-8213/aa624e. arXiv: 1702.00072.

[105] A. Saro et al. “Optical-SZE Scaling Relations for DES Optically Selected Clusters within the SPT-SZ Survey”. In: *ArXiv e-prints* (May 2016). arXiv: 1605.08770.

[106] C. Sánchez et al. “Cosmic voids and void lensing in the Dark Energy Survey Science Verification data”. In: *MNRAS* 465 (Feb. 2017), pp. 746–759. DOI: 10.1093/mnras/stw2745. arXiv: 1605.03982.

[107] L. Clerkin et al. “Testing the lognormality of the galaxy and weak lensing convergence distributions from Dark Energy Survey maps”. In: *MNRAS* 466 (Apr. 2017), pp. 1444–1461. DOI: 10.1093/mnras/stw2106. arXiv: 1605.02036.

[108] C. Hennig et al. “Galaxy populations in massive galaxy clusters to z = 1.1: colour distribution, concentration, halo occupation number and red sequence fraction”. In: *MNRAS* 467 (June 2017), pp. 4015–4035. DOI: 10.1093/mnras/stx175. arXiv: 1604.00988.

[109] V. Vikram et al. “Wide-field lensing mass maps from Dark Energy Survey science verification data: Methodology and detailed analysis”. In: *Phys. Rev. D* 92.2, 022006 (July 2015), p. 022006. DOI: 10.1103/PhysRevD.92.022006. arXiv: 1504.03002.

[110] M. R. Becker et al. “Cosmic shear measurements with Dark Energy Survey Science Verification data”. In: *Phys. Rev. D* 94.2, 022002 (July 2016), p. 022002. DOI: 10.1103/PhysRevD.94.022002. arXiv: 1507.05598.

[111] D. Kirk et al. “Cross-correlation of gravitational lensing from DES Science Verification data with SPT and Planck lensing”. In: *MNRAS* 459 (June 2016), pp. 21–34. DOI: 10.1093/mnras/stw570. arXiv: 1512.04535.

[112] B. Soergel et al. “Detection of the kinematic Sunyaev-Zel’dovich effect with DES Year 1 and SPT”. In: *MNRAS* 461 (Sept. 2016), pp. 3172–3193. DOI: 10.1093/mnras/stw1455. arXiv: 1603.03904.

[113] E. Baxter et al. “Joint measurement of lensing-galaxy correlations using SPT and DES SV data”. In: *MNRAS* 461 (Oct. 2016), pp. 4099–4114. DOI: 10.1093/mnras/stw1584. arXiv: 1602.07384.

[114] J. Prat et al. “Galaxy bias from galaxy-galaxy lensing in the DES Science Verification Data”. In: *ArXiv e-prints* (Sept. 2016). arXiv: 1609.08167.

[115] J. Clampitt et al. “Galaxy-galaxy lensing in the Dark Energy Survey Science Verification data”. In: *MNRAS* 465 (Mar. 2017), pp. 4204–4218. DOI: 10.1093/mnras/stw2988. arXiv: 1603.05790.

[116] T. Giannantonio et al. “CMB lensing tomography with the DES Science Verification galaxies”. In: *MNRAS* 456 (Mar. 2016), pp. 3213–3244. DOI: 10.1093/mnras/stv2678. arXiv: 1507.05551.

[117] A. Kovács et al. “Imprint of DES superstructures on the cosmic microwave background”. In: *MNRAS* 465 (Mar. 2017), pp. 4166–4179. DOI: 10.1093/mnras/stw2968. arXiv: 1610.00637.

[118] T. Abbott et al. “Cosmology from cosmic shear with Dark Energy Survey Science Verification data”. In: *Phys. Rev. D* 94.2, 022001 (July 2016), p. 022001. DOI: 10.1103/PhysRevD.94.022001. arXiv: 1507.05552.

[119] T. Kacprzak et al. “Cosmology constraints from shear peak statistics in Dark Energy Survey Science Verification data”. In: *MNRAS* 463 (Dec. 2016), pp. 3653–3673. DOI: 10.1093/mnras/stw2070. arXiv: 1603.05040.

[120] J. Kwan et al. “Cosmology from large-scale galaxy clustering and galaxy-galaxy lensing with Dark Energy Survey Science Verification data”. In: *MNRAS* 464 (Feb. 2017), pp. 4045–4062. DOI: 10.1093/mnras/stw2464. arXiv: 1604.07871.

[121] Dark Energy Survey Collaboration et al. “The Dark Energy Survey: more than dark energy - an overview”. In: *MNRAS* 460 (Aug. 2016), pp. 1270–1299. DOI: 10.1093/mnras/stw641. arXiv: 1601.00329.

[122] T. Broadhurst. “Mass distributions of clusters from gravitational magnification”. In: *Dark Matter*. Ed. by S. S. Holt and C. L. Bennett. Vol. 336. American Institute of Physics Conference Series. July 1995, pp. 320–329. DOI: 10.1063/1.48351. eprint: astro-ph/9505010.

[123] A. H. Bauer et al. “Magnification of photometric LRGs by foreground LRGs and clusters in the Sloan Digital Sky Survey”. In: *MNRAS* 440 (June 2014), pp. 3701–3713. DOI: 10.1093/mnras/stu530. arXiv: 1312.2458.

[124] J. Ford et al. “Cluster magnification and the mass-richness relation in CFHTLenS”. In: *MNRAS* 439 (Apr. 2014), pp. 3755–3764. DOI: 10.1093/mnras/stu225. arXiv: 1310.2295 [astro-ph.CO].

[125] I. Chiu et al. “Detection of enhancement in number densities of background galaxies due to magnification by massive galaxy clusters”. In: *MNRAS* 457 (Apr. 2016), pp. 3050–3065. DOI: 10.1093/mnras/stw190. arXiv: 1510.01745.

[126] H. Hildebrandt, L. van Waerbeke, and T. Erben. “CARS: The CFHTLS-Archive-Research Survey. III. First detection of cosmic magnification in samples of normal high-z galaxies”. In: *A&A* 507 (Nov. 2009), pp. 683–691. DOI: 10.1051/0004-6361/200912655. arXiv: 0906.1580.

[127] C. B. Morrison et al. “Tomographic magnification of Lyman-break galaxies in the Deep Lens Survey”. In: *MNRAS* 426 (Nov. 2012), pp. 2489–2499. DOI: 10.1111/j.1365-2966.2012.21826.x. arXiv: 1204.2830.

[128] M. Seldner and P. J. E. Peebles. “Statistical analysis of catalogs of extragalactic objects. XI - Evidence of correlation of QSOs and Lick galaxy counts”. In: *ApJ* 227 (Jan. 1979), pp. 30–36. DOI: 10.1086/156699.

[129] C. J. Hogan, R. Narayan, and S. D. M. White. “Quasar lensing by galaxies?” In: *Nature* 339 (May 1989), p. 106. DOI: 10.1038/339106b0.

[130] W. Fugmann. “Statistical gravitational lensing and the Lick catalogue of galaxies”. In: *A&A* 240 (Dec. 1990), pp. 11–21.

[131] M. Bartelmann and P. Schneider. “Large-scale correlations between QSOs and galaxies - an effect caused by gravitational lensing?” In: *A&A* 268 (Feb. 1993), pp. 1–13.

[132] B. Ménard and M. Bartelmann. “Cosmological information from quasar-galaxy correlations induced by weak lensing”. In: *A&A* 386 (May 2002), pp. 784–795. DOI: 10.1051/0004-6361:20020274. eprint: astro-ph/0203163.

[133] Ryan Scranton et al. “Detection of Cosmic Magnification with the Sloan Digital Sky Survey”. In: *The Astrophysical Journal* 633.2 (2005), p. 589. URL: http://stacks.iop.org/0004-637X/633/i=2/a=589.

[134] L. Wang et al. “HerMES: detection of cosmic magnification of submillimetre galaxies using angular cross-correlation”. In: *MNRAS* 414 (June 2011), pp. 596–601. DOI: 10.1111/j.1365-2966.2011.18417.x. arXiv: 1101.4796.

[135] B. Ménard et al. “Measuring the galaxy-mass and galaxy-dust correlations through magnification and reddening”. In: *MNRAS* 405 (June 2010), pp. 1025–1039. DOI: 10.1111/j.1365-2966.2010.16486.x. arXiv: 0902.4240.

[136] B. Jain and M. Lima. “Magnification effects on source counts and fluxes”. In: *MNRAS* 411 (Mar. 2011), pp. 2113–2117. DOI: 10.1111/j.1365-2966.2010.17505.x. arXiv: 1003.6127.

[137] C. B. Morrison and H. Hildebrandt. “Mitigating systematic errors in angular correlation function measurements from wide field surveys”. In: *MNRAS* 454 (Dec. 2015), pp. 3121–3133. DOI: 10.1093/mnras/stv2103. arXiv: 1509.04290.

[138] P. Schechter. “An analytic expression for the luminosity function for galaxies.” In: *ApJ* 203 (Jan. 1976), pp. 297–306. DOI: 10.1086/154079.

[139] R. Moessner and B. Jain. “Angular cross-correlation of galaxies - A probe of gravitational lensing by large-scale structure”. In: *MNRAS* 294 (Feb. 1998), pp. L18–L24. DOI: 10.1046/j.1365-8711.1998.01378.x. eprint: astro-ph/9709159.

[140] P. Fosalba et al. “The MICE Grand Challenge light-cone simulation - III. Galaxy lensing mocks from all-sky lensing maps”. In: *MNRAS* 447 (Feb. 2015), pp. 1319–1332. DOI: 10.1093/mnras/stu2464. arXiv: 1312.2947.

[141] P. Fosalba et al. “The MICE grand challenge lightcone simulation - I. Dark matter clustering”. In: *MNRAS* 448 (Apr. 2015), pp. 2987–3000. DOI: 10.1093/mnras/stv138. arXiv: 1312.1707.

[142] M. Crocce et al. “The MICE Grand Challenge lightcone simulation - II. Halo and galaxy catalogues”. In: *MNRAS* 453 (Oct. 2015), pp. 1513–1530. DOI: 10.1093/mnras/stv1708. arXiv: 1312.2013.

[143] M. Crocce et al. “Galaxy clustering, photometric redshifts and diagnosis of systematics in the DES Science Verification data”. In: *MNRAS* 455 (Feb. 2016), pp. 4301–4324. DOI: 10.1093/mnras/stv2590. arXiv: 1507.05360.

[144] C. Chang et al. “Modeling the Transfer Function for the Dark Energy Survey”. In: *The Astrophysical Journal* 801.2 (2015), p. 73. URL: http://stacks.iop.org/0004-637X/801/i=2/a=73.

[145] E. Bertin and S. Arnouts. “SExtractor: Software for source extraction.” In: *A&AS* 117 (June 1996), pp. 393–404. DOI: 10.1051/aas:1996164.

[146] R. Mandelbaum et al. “Systematic errors in weak lensing: application to SDSS galaxy-galaxy weak lensing”. In: *MNRAS* 361 (Aug. 2005), pp. 1287–1322. DOI: 10.1111/j.1365-2966.2005.09282.x. eprint: astro-ph/0501201.

[147] I. Sevilla et al. “The Dark Energy Survey Data Management System”. In: *ArXiv e-prints* (Sept. 2011). arXiv: 1109.6741 [astro-ph.IM].

[148] S. Desai et al. “The Blanco Cosmology Survey: Data Acquisition, Processing, Calibration, Quality Diagnostics, and Data Release”. In: *ApJ* 757, 83 (Sept. 2012), p. 83. DOI: 10.1088/0004-637X/757/1/83. arXiv: 1204.1210 [astro-ph.CO].

[149] J. J. Mohr et al. “The Dark Energy Survey data processing and calibration system”. In: *Software and Cyberinfrastructure for Astronomy II*. Vol. 8451. Proc. SPIE. Sept. 2012, p. 84510D. DOI: 10.1117/12.926785. arXiv: 1207.3189 [astro-ph.IM].

[150] M. E. C. Swanson et al. “Methods for rapidly processing angular masks of next-generation galaxy surveys”. In: *MNRAS* 387 (July 2008), pp. 1391–1402. DOI: 10.1111/j.1365-2966.2008.13296.x. arXiv: 0711.4352.

[151] K. M. Górski et al. “HEALPix: A Framework for High-Resolution Discretization and Fast Analysis of Data Distributed on the Sphere”. In: *ApJ* 622 (Apr. 2005), pp. 759–771. DOI: 10.1086/427976. eprint: astro-ph/0409513.

[152] M. Carrasco Kind and R. J. Brunner. “TPZ: photometric redshift PDFs and ancillary information by using prediction trees and random forests”. In: *MNRAS* 432 (June 2013), pp. 1483–1501. DOI: 10.1093/mnras/stt574. arXiv: 1303.7269.

[153] C. Sánchez et al. “Photometric redshift analysis in the Dark Energy Survey Science Verification data”. In: *MNRAS* 445 (Dec. 2014), pp. 1482–1506. DOI: 10.1093/mnras/stu1836. arXiv: 1406.4407 [astro-ph.IM].

[154] M. Jarvis, G. Bernstein, and B. Jain. “The skewness of the aperture mass statistic”. In: *MNRAS* 352 (July 2004), pp. 338–352. DOI: 10.1111/j.1365-2966.2004.07926.x. eprint: astro-ph/0307393.

[155] S. D. Landy and A. S. Szalay. “Bias and variance of angular correlation functions”. In: *ApJ* 412 (July 1993), pp. 64–71. DOI: 10.1086/172900.

[156] E. Suchyta et al. “No galaxy left behind: accurate measurements with the faintest objects in the Dark Energy Survey”. In: *MNRAS* 457 (Mar. 2016), pp. 786–808. DOI: 10.1093/mnras/stv2953. arXiv: 1507.08336.

[157] James MacQueen et al. “Some methods for classification and analysis of multivariate observations”. In: *Proceedings of the fifth Berkeley symposium on mathematical statistics and probability*. Vol. 1. 14. Oakland, CA, USA. 1967, pp. 281–297.

[158] F. Pedregosa et al. “Scikit-learn: Machine Learning in Python”. In: *Journal of Machine Learning Research* 12 (2011), pp. 2825–2830.

[159] Planck Collaboration. “Planck 2015 results. XIII. Cosmological parameters”. In: *A&A* 594, A13 (Sept. 2016), A13. DOI: 10.1051/0004-6361/201525830. arXiv: 1502.01589.

[160] C. Chang et al. “Galaxy bias from the Dark Energy Survey Science Verification data: combining galaxy density maps and weak lensing maps”. In: *MNRAS* 459 (July 2016), pp. 3203–3216. DOI: 10.1093/mnras/stw861. arXiv: 1601.00405.

[161] Robert E. Kass and Adrian E. Raftery. “Bayes Factors”. In: *Journal of the American Statistical Association* 90.430 (1995), pp. 773–795. ISSN: 01621459. URL: http://www.jstor.org/stable/2291091.

[162] A. J. Ross et al. “The clustering of galaxies in the SDSS-III Baryon Oscillation Spectroscopic Survey: analysis of potential systematics”. In: *MNRAS* 424 (July 2012), pp. 564–590. DOI: 10.1111/j.1365-2966.2012.21235.x. arXiv: 1203.6499.

[163] B. Leistedt et al. “Mapping and simulating systematics due to spatially-varying observing conditions in DES Science Verification data”. In: *ArXiv e-prints* (July 2015). arXiv: 1507.05647.

[164] S. Ho et al. “Clustering of Sloan Digital Sky Survey III Photometric Luminous Galaxies: The Measurement, Systematics, and Cosmological Implications”. In: *ApJ* 761, 14 (Dec. 2012), p. 14. DOI: 10.1088/0004-637X/761/1/14. arXiv: 1201.2137.

[165] F. Elsner, B. Leistedt, and H. V. Peiris. “Unbiased methods for removing systematics from galaxy clustering measurements”. In: *MNRAS* 456 (Feb. 2016), pp. 2095–2104. DOI: 10.1093/mnras/stv2777. arXiv: 1509.08933.

[166] C. Bonnett et al. “Redshift distributions of galaxies in the Dark Energy Survey Science Verification shear catalogue and implications for weak lensing”. In: *Phys. Rev. D* 94 (4 Aug. 2016), p. 042005. DOI: 10.1103/PhysRevD.94.042005. URL: http://link.aps.org/doi/10.1103/PhysRevD.94.042005.

[167] G. Bernstein and D. Huterer. “Catastrophic photometric redshift errors: weak-lensing survey requirements”. In: *MNRAS* 401 (Jan. 2010), pp. 1399–1408. DOI: 10.1111/j.1365-2966.2009.15748.x. arXiv: 0902.2782 [astro-ph.CO].

[168] J. Asorey et al. “Galaxy clustering with photometric surveys using PDF redshift information”. In: *MNRAS* 459 (June 2016), pp. 1293–1309. DOI: 10.1093/mnras/stw721. arXiv: 1601.00357.

[169] J. A. Newman. “Calibrating Redshift Distributions beyond Spectroscopic Limits with Cross-Correlations”. In: *ApJ* 684, 88-101 (Sept. 2008), pp. 88–101. DOI: 10.1086/589982. arXiv: 0805.1409.

[170] D. J. Matthews and J. A. Newman. “Reconstructing Redshift Distributions with Cross-correlations: Tests and an Optimized Recipe”. In: *ApJ* 721 (Sept. 2010), pp. 456–468. DOI: 10.1088/0004-637X/721/1/456. arXiv: 1003.0687 [astro-ph.CO].

[171] B. Ménard et al. “Clustering-based redshift estimation: method and application to data”. In: *ArXiv e-prints* (Mar. 2013). arXiv: 1303.4722.

[172] V. Scottez et al. “Clustering-based redshift estimation: application to VIPERS/CFHTLS”. In: *MNRAS* 462 (Oct. 2016), pp. 1683–1696. DOI: 10.1093/mnras/stw1500. arXiv: 1605.05501.

[173] P. Graff et al. “SKYNET: an efficient and robust neural network training tool for machine learning in astronomy”. In: *MNRAS* 441 (June 2014), pp. 1741–1759. DOI: 10.1093/mnras/stu642. arXiv: 1309.0790 [astro-ph.IM].

[174] N. Benítez. “Bayesian Photometric Redshift Estimation”. In: *ApJ* 536 (June 2000), pp. 571–583. DOI: 10.1086/308947. eprint: astro-ph/9811189.